VILNIUS UNIVERSITY
CENTER FOR PHYSICAL SCIENCES AND TECHNOLOGY

GINTARĖ BATAVIČIŪTĖ

NEW METHODS FOR QUANTITATIVE EVALUATION OF LASER DAMAGE PRECURSORS

Doctoral dissertation
Technological Sciences, Materials Engineering (08T)

Vilnius, 2015

The research was performed in 2011–2015 at Vilnius University.

Scientific supervisor – dr. Andrius Melninkaitis
(Vilnius University, Technological Sciences, Materials Engineering – 08T).

VILNIAUS UNIVERSITETAS
FIZINIŲ IR TECHNOLOGIJOS MOKSLŲ CENTRAS

GINTARĖ BATAVIČIŪTĖ

NAUJI LAZERINĘ PAŽAIDĄ SUKELIANČIŲ DEFEKTŲ KIEKYBINIO VERTINIMO METODAI

Daktaro disertacija
Technologijos mokslai, medžiagų inžinerija (08T)

Vilnius, 2015

Disertacija rengta 2011–2015 metais Vilniaus universitete.

Mokslinis vadovas – dr. Andrius Melninkaitis
(Vilniaus universitetas, technologijos mokslai, medžiagų inžinerija – 08T).

Contents

Acknowledgements

The PhD studies are a journey of discovery. As every great adventure it starts with a single step. For me it was a lecture course on laser technologies given by *prof. habil. dr. V. Sirutkaitis*. I am sincerely thankful to him for the opportunity to work in Laser Research Center of Vilnius University, which was my first introduction into scientific society.

My "scientific life" started at Optics Characterization Group. There I met my supervisor *dr. A. Melninkaitis*. It is said, that the best way to teach is by example. He was a mastermind of this approach. The most valuable lesson I have learned working with him is *"do your best in everything you do"*. So, I would like to express my fairest gratitude to him for his guidance, friendship, patience and overnight work.

It's the friends we meet along life's road who help us appreciate the journey. Indeed, PhD studies are the time you grow as a scientist and as a person. During my professional carrier I was lucky to meet and learn from the best.

I would like to thank my former colleagues from *Laser Zentrum Hannover e.V.* for a possibility to join, work and learn from them. Special thanks to *Istvan Balasa*, *Marco Jupé*, *Detlev Ristau* and *Hendrik Gebauer* for their hospitality, friendship and shared knowledge.

Many thanks to the team of Active Optical Systems from *Deutsches Zentrum für Luft– und Raumfahrt*, especially *Wolfgang Riede* and *Helmut Schröder* for the great possibility of practice on an interesting theme.

I would also like to express my gratitude to *Simonas Kičas* and all the personnel of Center of Physical Science and Technologies for the preparation of experimental samples and cooperation in joint projects.

A big thank you to my “partners in crime” for great work atmosphere, assistance in the lab and much needed coffee breaks: *Mindaugas Ščiuka, Egidijus Pupka, Linas Smalakys, Arūnas Petravičius* and *Julius Mirauskas*.

In order to travel far during your PhD journey, you need to have fuel. Here I would like to acknowledge Lithuanian Government, Lithuanian study and science foundation, the Faculty of Physics and European structural funds for the financial support of my studies and research.

Writing a story about your journey, better known as PhD thesis, is a challenging task, because it’s no longer enough to understand things for yourself, you should make it clear for others as well. I would like thank *Gintaras Toločka* for great ideas on how to combine scientific data with graphical design elements. Also, I would like to acknowledge the support of *Zita Manstavičienė* and *Andrius Bernotas* for the proofreading of the manuscript.

Every story that is worth telling, has its moments of mountain peaks and moments of deep valleys of despair. So, I would like to thank my personal support team: *Viktorija Straukaitė*, *Ieva Gelžinytė*, *Aušra Balskienė* and *Vėja Laurinaitis*, for being here for me and patiently listening to my excuse “I could not make it, due to my busy schedule". Also, for the sincere belief in me I would like to thank *Gytis Kvedaravičius*. The last but not the least, I would not have made it without inspiration, support and the motivation of my sisters: *Inga*, *Giedrė* and *Audra*.

PhD is a journey of discovery. It will push you to your limits and leaves you wanting for more. As Fort Minor rhymes: and for those you that want to know what it’s all about –

This is ten percent luck, twenty percent skill,
Fifteen percent concentrated power of will,
Five percent pleasure, fifty percent pain,
And a hundred percent reason to remember the name.

Dedicated to four special ladies: Inga, Audra, Giedrė and Daniela.

List of Abbreviations

AOI - **A**ngle **o**f **I**incidence
AR - **A**nti-**R**eflective coating
CCD - **C**arge-**C**oupled **D**evice
CIPM - **I**nternational **C**omittee for **W**eights and **M**easures
CMP - **C**hemical **M**echanical **P**olishing
DFM - **D**amage **F**requency **M**ethod
EBD - **E**lectron **B**eam **D**eposition
ED - **E**nergy **D**ensity
FS - **F**used **S**ilica
FWHM - **F**ull **W**idth at **H**alf **M**aximum
HR - **H**ighly **R**eflective coating
IAD - **I**on **A**ssisted **D**eposition
IBE - **I**on **B**eam **E**tching
IBS - **I**on **B**eam **S**puttering
ISO - **I**nternational-**S**tandard-**O**rganisation
LIC - **L**aser-**I**nduced **C**ontamination
LID - **L**aser-**I**nduced **D**amage
LIDT - **L**aser-**I**nduced **D**amage **T**hreshold
SSD - **S**ub**S**urface-**D**efects
SHG - **S**econd **H**armonic **G**eneration
SW - **S**tanding-**W**ave
MLE - **M**aximum **L**ikelihood **E**stimates

MSE - **M**ean **S**quared **E**rror
MR - **M**agnetorheological **f**luids
MRF - **M**agnetorheological **f**inishing
NBOHC - **N**on **B**ridging **O**xygen **H**ole **C**enter
Nd:YAG - **N**eodymium-doped **Y**ttrium **A**luminium **G**arnet
ODC - **O**xygen **D**eficiency **C**enter
PDF - **P**robability **D**ensity **F**unction
QWOT - **Q**uater-**W**ave **O**ptical **T**hickness
RPM - **R**ate **P**er **M**inute
UV - **U**ltraviolet

Introduction

The sun has one drawback: it can not see itself.
Socrates, Greek philosopher.

Within only 55 years after the demonstration of the first laser spark back in 1960 by T. H. Maiman [1], laser technologies became an irreplaceable part of the nowadays world. The laser has evolved into high-power laser systems, which have become a driving force in scientific, commercial and mass production applications. Today, the invention of laser – *Light Amplification by Stimulated Emission of Radiation* – is recognized as one of the most important discoveries in human history next to the press, steam engine or antibiotics. Laser-produced radiation can be focused onto a tight spot and concentrate sufficient amount of power to destroy even transparent materials in the focal plane [2, 3]. So, the feature that makes the laser a perfect tool for precise and accurate material processing [4] also makes it a self-destructive device. First reports about plasma sparks in air and damage induced in transparent dielectrics by applied laser radiation were released right after the invention of the laser itself [5–8]. Laser-induced damage (LID) defines any irreversible change in an optical structure caused by the surface or bulk melting, material softening and bending, cracking, pitting, vaporization or violent shattering [2, 3]. Ability of matter to withstand laser radiation, known as optical resistance, is characterized via laser-induced damage threshold (LIDT) – the highest quantity of laser radiation incident upon an optical component leaving it undamaged [9]. Optical elements damaged by laser radiation pose a threat to efficiency and safety of the whole operating laser system and often prevent it from operating at all. Therefore, to a large extent, development of high-peak-power laser systems has been made possible only due to corresponding development of optical glasses and deeper understanding of reasons why the elements get broken. Laser-induced damage threshold has been shown to be sensitive to irradiation parameters [10–21], environment conditions [22–27] and material properties [21, 28–31]. This knowledge was one of the main factors, that allowed to reach extreme laser intensities in National Ignition Facility (NIF) [32] and other project such as Laser MegaJoule [33] and Extreme Light Intensities (ELI) [34]. A historical laser pulse has been demonstrated by NIF. Laser system of 192 beams delivered more than 500 trillion watts (terawatts) of peak power and 1.85 megajoules of ultraviolet laser light to its target [32]. However, with each advancement in optics manufacture, new requirements for optical resistance arise as well. Thus, development of high-power laser system design and performance require corresponding advances in laser damage resistance improvement.

High-power nanosecond lasers take an important part of worldwide laser market. The demand for laser systems operating at ultraviolet – UV (355 nm and less) radiation is constantly increasing in the laser processing industry. The shorter wavelength couples (or is absorbed) more efficiently with many target materials than does the 1064 nm fundamental or even second harmonic 532 nm wavelength. Comparing the same three wavelengths, UV radiation can also be focused into smaller spot on the focal plane, thus materials can be processed more accurately. Furthermore, short wavelength lasers are valuable tools for scientific study. However, poor optical resistance performance of laser components limits their practical use and development. In practice it is hardly possible to make optics with quality any better than it can be tested, therefore LIDT metrology plays an essential role here. Damage frequency method (DFM – also known as damage probability method) [35, 36] is the standard LIDT testing technique [9]. However, it has been shown that LIDT values estimated by this procedure features poor accuracy and repeatability [37–39, 39, 40].

In nanosecond pulse regime, LIDT is mostly determined by nano-size defects (damage precursors) inherent to the manufacturing processes, such as glass shaping, polishing, cleaning and deposition procedures [28, 41, 42]. Thus, a careful notion of defect properties is necessary in order to improve the overall quality of manufacturing processes and their final products: optical elements. Up till now the techniques developed to quantify the damage precursors were the statistical models based on defect ensemble – distribution of the local defect damage threshold in respect to the defect density at the surface or volume of interest [43–45]. However, the true defect ensemble is never known, it can be only assumed. Several hypotheses on the defect ensemble distribution function have been suggested over time [43–50]. Nevertheless, there still is no unambiguous proof which of the available hypotheses should be used for a particular type of samples. Furthermore, standard testing procedures are focused on the investigation of the surface defects. The possibility to distinguish between the coating and polishing defects is rarely addressed. Also, current statistical models do not take into account interference caused effects. This is of particular importance when considering multilayer coatings. Aforementioned factors raises the need for optical resistance metrology advancement on at least three issues. Firstly, accuracy and repeatability problems related to standard LIDT evaluation models should be addressed. Secondly, the lack of information about the true defect ensemble application should be carefully analysed and compared with other available techniques. Thirdly, LIDT metrology should be expanded by considering interference effects when used for defects characterization and LIDT evaluation of multilayer coatings.

Objective of the thesis

Advancement of optical resistance metrology towards better quantification of laser-induced damage precursors in dielectric materials when operating in nanosecond laser pulse regime.

Thesis is structured as follows:

Chapter 1 is a literature overview on LID phenomena and summarizes knowledge of LIDT dependence on irradiation parameters, environment and material properties. This chapter also focus attention on the origin of intrinsic and extrinsic defects existing within the optical elements and their effect on LIDT of the materials.

Chapter 2 introduces the background of LIDT metrology. Poor accuracy and repeatability of the standard LIDT testing procedure is addressed. The aim of this chapter is to identify the uncertainty sources causing unreliable LIDT test results and to suggest a revised approach that could benefit the users of optical components and be an advance in the optimization of manufacture of optical devices.

Chapter 3 is focused on the quantitative estimation of damage precursors in optical elements. Defects are characterized by mathematical model – defect ensemble. An attempt to determine the true defect ensemble is made by applying different measurement concepts. Two approaches are used to extract defect ensembles, namely, damage probability and damage density measurements. A direct comparison of defect ensembles obtained from both approaches is carried out for the first time. Results of the comparison indicates apparent differences among extracted defect ensembles, that are discussed in detail.

Chapter 4 is dedicated to the identification of weak layers in optical element. Particular attention is focused on ability to distinguish which type of defects – coating or polishing – limits the optical resistance of the component. For this purpose new metrological tools are introduced.

The main tasks of the thesis

1st task – To develop Monte Carlo-based simulation software dedicated to 1-on-1 LIDT testing analysis with the capability to imitate real experimental conditions and analyse statistical models used for laser-induced damage threshold evaluation.

2nd task – To perform 1-on-1 damage probability measurements on uncoated and thin film deposited optical substrates in order to analyse how laser-induced damage threshold of the tested samples depends on distribution of the defects and irradiation conditions (angle of incidence and polarization).

3rd task – To quantitatively evaluate the effect of shot-to-shot laser peak fluence fluctuations in 1-on-1 damage probability measurements and expand damage probability model to include experimental uncertainty.

4th task – Directly compare defect ensembles extracted from damage probability measurements and damage density measurements performed by raster scan procedure.

5th task – To extend standard damage probability model by considering the interference effects and volumetric nature of defect ensembles within multilayer coatings.

Statements to defend

1st statement – The repeatability of 1-on-1 laser-induced damage threshold values determined for dielectric materials in nanosecond pulse range increases when maximum-likelihood based evaluation procedure is used instead of standard approach based on the least squares method. The accuracy of the determined results increases when fluence fluctuations are taken into account in the damage probability model.

2nd statement – Defect ensemble can be extracted from the damage density data obtained via raster scan procedure by defining an effective laser fluence distribution convolved with corresponding assumed defect ensembles. Defect ensembles extracted by the raster scan and the damage probability measurement do not match due to the surface contamination by ablation particles.

3rd statement – The laser-induced damage threshold of subsurface defects located at Beilby layer in fused silica samples, that limit the optical resistance of dielectric materials in nanosecond pulse regime at a wavelength of 355 nm, might decrease up to 4 times, when fused silica is coated with a monolayer – even in the cases where the coating material does not limit the damage threshold.

4th statement – The laser-induced damage threshold of the top layers of multilayer highly-reflective HfO_2/SiO_2 mirror designed to operate in nanosecond pulse regime at wavelength of 355 nm is higher than the LIDT of layers distributed deeper than 300 nm from the surface. A higher maximal internal electric field at damaging fluence is achieved in multilayer highly-reflective mirrors than in monolayers.

Scientific novelty

1st. It has been shown, that relative uncertainty of laser-induced damage threshold values estimated by linear regression combined with the least square method is high due to the distributions of experimentally measured damage probability being asymmetric, which can be explained by binomial nature of damage event. Also it has been demonstrated that pulse-to-pulse fluence fluctuation causes differences between theoretically assumed and experimentally measured damage probability curves, that leads to additional systematic error in determined LIDT values. An alternative, based on maximum likelihood principle method is suggested, that considers effects caused by experimental uncertainty in measurement process. The method is proven to be suitable for accurate and repeatable estimation of both laser-induced damage threshold and defect density, and evaluation of coverage intervals.

2nd. A direct comparison of defect ensembles extracted by two methods, namely, damage probability and raster scan procedure, has revealed that these methods conclude different results. Three experimental limitations of the raster scan procedure are identified: surface contamination by ablation products, clustering of the craters and effects own to experimental uncertainty in measurement process.

3rd. It has been demonstrated that the laser-induced damage of defect located in Beilby layer might decrease when optical sample is coated with transparent layer, that by itself does not limit the optical resistance. Analysis was performed using volumetric damage probability model, that takes into account electric field distribution caused by interference in multilayer coatings.

4th. It has been shown that the laser-induced damage threshold dependance on angle of incidence and polarization for multilayer highly-reflective HfO_2/SiO_2 mirror, design to operate at 355 nm wavelength can be explained by the volumetric-statistical model, assuming that the damage threshold of distinct layers is not constant and decreases for deeper layers in respect of the top layers.

Practical benefits

1st. An alternative method to estimate laser-induced damage threshold from damage provability curves is suggested. It is based on maximum-likelihood principle and parameterizations of model function, that are the key features which allow to significantly improve both repeatability and accuracy of estimated LIDT values.

2nd. A new approach to determine defect ensemble is introduced, that is capable of taking into account the uncertainty in measurement process. Several considerable risk factories of the raster scan procedure are identified.

3th. A new method to distinguish between coating and polishing defects, thus identifying which manufacturing process limits laser-induced damage threshold of the optical element, is developed. Such method can be used to analyse which procedure – coating or polishing – should be optimized (improved) first.

4th. It has been shown that the laser-induced damage of uncoated fused silica and multilayer highly-reflective HfO_2/SiO_2 mirrors in nanosecond pulse regime and at wavelength of 355 nm is dependant on the polishing and the coating processes, respectively. Meanwhile, the laser-induced damage threshold of monolayer SiO_2/HfO_2 monolayers decreases due the interplay between polishing and coating processes.

Contribution

The author prepared (or actively participated in the preparation of) both theoretical and experimental work presented in this thesis. Her contribution and responsibilities consist of: literature overview, the development of theoretical models, numerical modeling, experimental testing. However, the author would like to specify the significant contribution of these people:

Dr. Andrius Melninkaitis initiated the theme of the thesis. He participated in developing ideas, consulted on experimental design and the interpretation of results;
Egidijus Pupka assisted in 1-on-1 LIDT measurements;
Mindaugas Ščiuka assisted in performing raster scan procedure;
Linas Smalakys helped to create and develop the volumetric damage probability model, introduced in **Chapter 4**.

The author would also like to acknowledge the contribution of:

Povilas Grigas, who provided consultancy on Bayesian approach implementation in LIDT metrology discussed in **Chapter 2**;
Prof. Marijus Radavičius, who provided valuable discussions related to the concept of nonlinear regression application and other statistical models;
Simonas Kičas, who prepared experimental samples;

Dr. Kęstutis Juškevičius and *Saulė Abbas*, who helped to perform with surface analysis by atomic force microscopy.

Approbation

ISI scientific papers directly related to the thesis

A1. **G. Batavičiūtė**, M. Ščiuka, and A. Melninkaitis, Direct comparison of defect ensembles extracted from damage probability and raster scan measurements, J. Appl. Phys., **118**, 105306 (2015).

A2. L. Smalakys, **G. Batavičiūtė**, E. Pupka, and A. Melninkaitis, Parametric analysis of damage probability: a tool to identify weak layers within multilayer coatings, Appl. Opt., **54**(10), 2953–2962 (2015).

A3. **G. Batavičiūtė**, P. Grigas, L. Smalakys, and A. Melninkaitis, Revision of laser-induced damage threshold evaluation from damage probability data, Rev. Sci. Instru., **84**, 045108 (2013).

Other scientific papers directly related to the thesis

A4. **G. Batavičiūtė**, M. Ščiuka, V. Plerpaitė, and A. Melninkaitis, Direct comparison of damage frequency method and raster scan procedure, Proc. SPIE **9632**, 963261 (2015).

A5. L. Smalakys, **G. Batavičiūtė**, E. Pupka, and A. Melninkaitis, Towards separation of bulk and interface defects: damage probability analysis of thin film coatings, Proc. SPIE **9237**, 92371Z (2014).

A6. **G. Batavičiūtė**, P. Grigas, L. Smalakys, and A. Melninkaitis, Bayesian approach of laser-induced damage threshold analysis and determination of error bars, Proc. SPIE **8530**, 85301S (2012).

A7. S. Liukaitytė, **G. Batavičiūtė**, E. Pupka, M. Ščiuka, I. Kraujalienė, D. Tumosa, A. Skrebutėnas, K. Juškevičius, T. Tolenis, S. Kičas, R. Drazdys, R. Buzelis, and A. Melninkaitis, Effect of conventional fused silica preparation and deposition techniques on surface roughness, scattering, and laser damage resistance, Proc. SPIE **8530**, 853027 (2012).

A8. A. Melninkaitis, **G. Batavičiūtė**, and V. Sirutkaitis, Numerical analysis of laser-induced damage threshold search algorithms and their uncertainty, Proc. SPIE **7504**, 75041D (2009).

Conferences directly related to the thesis

C1. **G. Batavičiūtė**, M. Ščiuka, V. Plerpaitė, and A. Melninkaitis, Direct comparison of damage frequency method and raster scan procedure, Boulder Damage Symposium 27–30 September 2015, Boulder, Colorado, USA [9632–61].

C2. L. Smalakys, **G. Batavičiūtė**, E. Pupka, and A. Melninkaitis, Damage probability analysis in thin film coatings containing bulk and interface defects, Boulder Damage Symposium 14–17 September 2014, Boulder, Colorado, USA [9237–74].

C3. **G. Batavičiūtė**, P. Grigas, L. Smalakys, and A. Melninkaitis, Bayesian approach of laser-induced damage threshold analysis and determination of error bars, Boulder Damage Symposium 23–26 September 2012, Boulder, Colorado, USA [8530–73].

C4. S. Liukaitytė, **G. Batavičiūtė**, E. Pupka, M. Ščiuka, I. Kraujalienė, D. Tumosa, K. Juškevičius, A. Skrebutėnas, T. Tolenis, S. Kičas, R. Drazdys, R. Buzelis, and A. Melninkaitis, Effect of conventional fused silica preparation and deposition techniques on surface roughness, scattering, and laser damage resistance, Boulder Damage Symposium 23–26 September 2012, Boulder, Colorado, USA [8530–61].

C5. **G. Batavičiūtė**, A. Melninkaitis, and V. Sirutkaitis, Numerical analysis of laser-induced damage threshold search algorithms and their uncertainty, Boulder Damage Symposium 21–23 September 2009, Boulder, Colorado USA [8530–67].

C6. **G. Batavičiūtė**, A. Melninkaitis, and V. Sirutkaitis, Numerical analysis of laser-induced damage threshold search algorithms and their uncertainty, 38th Lithuania National Physics Conference 8–10 June 2009, Vilnius, Lithuania [S2–54].

ISI and other scientific papers, which are not directly related to the thesis

A9. L. Gallais, D. B. Douti, M. Commandré, **G. Batavičiūtė**, E. Pupka, M. Ščiuka, L. Smalakys, V. Sirutkaitis, and A. Melninkaitis, Wavelength dependence of femtosecond laser-induced damage threshold of optical materials, J. Appl. Phys., **177**(22), 223103 (2015).

A10. A. Žukauskas, **G. Batavičiūtė**, M. Ščiuka, T. Jukna, A. Melninkaitis, and M. Malinauskas, Characterization of photopolymers used in laser 3D micro/nanolithography by means of laser-induced damage threshold (LIDT), Opt. Mater. Express, **4**(8), 1601–1616 (2014).

A11. A. Žukauskas, **G. Batavičiūtė**, M. Ščiuka, Z. Balevičius, A. Melninkaitis, and M. Malinauskas, Effect of the photoinitiator presence and exposure conditions on laser-induced damage threshold of ORMOSIL (SZ2080), Opt. Mater., **39**, 224–231 (2015).

A12. L. Smalakys, **G. Batavičiūtė**, E. Pupka, and A. Melninkaitis, Comprehensive studies of IR to UV light intensification by nodular defects in HfO_2/SiO_2 multilayer mirrors, Proc. SPIE **9237**, 92371I (2014).

A13. A. Žukauskas, **G. Batavičiūtė**, M. Ščiuka, A. Melninkaitis, and M. Malinauskas, Laser-induced damage in photopolymers thin films with ultrashort pulses, Proc. SPIE **9130**, 913013 (2014).

A14. **G. Batavičiūtė**, E. Pupka, V. Pyragaitė, L. Smalakys, and A. Melninkaitis, Effect of longitudinal laser mode beating in damage probability measurements, Proc. SPIE **8885**, 88851M (2013).

A15. K. Juškevičius, S. Kičas, T. Tolenis, R. Buzelis, R. Drazdys, **G. Batavičiūtė**, E. Pupka, L. Smalakys, and A. Melninkaitis, Investigation of subsurface damage impact to resistance of laser radiation of fused silica substrates, Proc. SPIE **8885**, 888529 (2013).

A16. S. Kičas, **G. Batavičiūtė**, K. Juškevičius, T. Tolenis, R. Drazdys, R. Buzelis, and A. Melninkaitis, Characterization and application of HfO_2-SiO_2 mixtures produced by ion-beam sputtering technology, Proc. SPIE **8885**, 888521 (2013).

A17. S. Schrameyer, H. Mädebach, L. Jensen, D. Ristau, C. Heese, J. Piris, A. Ciapponi, B. Sarti, W. Riede, M. Lammers, P. Allenspacher, **G. Batavičiūtė**, L. Smalakys, A. Melninkaitis, and V. Sirutkaitis, Round-Robin experiment on LIDT measurements at 1064 nm in vacuum for space qualification of optics, Proc. SPIE **8885**, 88850F (2013).

A18. S. Liukaitytė, **G. Batavičiūtė**, E. Pupka, M. Ščiuka, I. Kraujalienė, D. Tumosa, A. Skrebutėnas, K. Juškevičius, T. Tolenis, S. Kičas, R. Drazdys, R. Buzelis, and A. Melninkaitis, Effect of conventional fused silica preparation and deposition techniques on surface roughness, scattering, and laser damage resistance, Proc. SPIE **8530**, 853027 (2012).

A19. W. Riede, H. Schröeder, **G. Batavičiūtė**, D. Wernham, A. Tighe, F. Pettazzi, and J. Alves, Laser-induced contamination on space optics, Proc. SPIE **8190**, 81901E (2011).

A20. H. Gebauer, M. Jupè, **G. Batavičiūtė**, D. Ristau, and R. Kling, Measurement of laser power resistance of fibers for PIV systems, Proc. SPIE **7132**, 713219 (2008).

Conferences, which are not directly related to the thesis

C7. L. Smalakys, **G. Batavičiūtė**, E. Pupka, and A. Melninkaitis, Comprehensive studies of UV light intensification by nodular defects in HfO_2-SiO_2 multilayer mirrors, Boulder Damage Symposium 14–17 September 2013, Boulder, Colorado USA [9237–55].

C8. **G. Batavičiūtė**, E. Pupka, V. Pyragaitė, L. Smalakys, and A. Melninkaitis, Effect of longitudinal laser mode beating in damage probability measurements, Boulder Damage Symposium 23–26 September 2013, Boulder, Colorado USA [8885–62].

C9. K. Juškevičius, S. Kičas, T. Tolenis, R. Buzelis, R. Drazdys, **G. Batavičiūtė**, E. Pupka, L. Smalakys, and A. Melninkaitis, Investigation of subsurface damage impact to resistance of laser radiation of fused silica substrates, Boulder Damage Symposium 23–26 September 2013, Boulder, Colorado USA [8885–75].

C10. **G. Batavičiūtė**, E. Pupka, V. Pyragaitė, L. Smalakys, V. Sirutkaitis, and A. Melninkaitis, Statistiniai reiškiniai optinio atsparumo metrologijoje, 40-th national Lithuanian Physics Conference, 10–12 June 2013, Vilnius, Lithuania S4–60.

C11. S. Schrameyer, H. Mädebach, L. Jensen, D. Ristau, C. Heese, J. Piris, A. Ciapponi, B. Sarti, W. Riede, M. Lammers, P. Allenspacher, **G. Batavičiūtė**, L. Smalakys, A. Melninkaitis, and V. Sirutkaitis, Round Robin experiment on LIDT measurements at 1064 nm in vacuum for space qualification of optics, Boulder Damage Symposium 23–26 September 2013, Boulder, Colorado USA [8885–14].

C12. L. Gallais-During, D. L. Douti, **G. Batavičiūtė**, E. Pupka, M. Ščiuka, L. Smalakys, A. Melninkaitis, F. Lemarchand, V. Sirutkaitis, and M. Commandré, Dependence of fs laser resistance of optical materials on wavelength, Boulder Damage Symposium 23–26 September 2013, Boulder, Colorado USA [8885–57].

C13. A. Žukauskas, **G. Batavičiūtė**, M. Ščiuka, A. Melninkaitis, and M. Malinauskas, Laser-induced damage threshold (LIDT) measurements of photopolymers used in 3D ultrafast laser micro/nano-lithography, Boulder Damage Symposium 23–26 September 2013, Boulder, Colorado USA [8885–63].

C14. S. Kičas, K. Juškevičius, T. Tolenis, R. Buzelis, R. Drazdys, **G. Batavičiūtė**, E. Pupka, L. Smalakys, and A. Melninkaitis, Characterization and application of hafnia-silica mixtures produced by ion-beam sputtering technology, Boulder Damage Symposium 23–26 September 2013, Boulder, Colorado USA [8885–80].

C15. S. Liukaitytė, **G. Batavičiūtė**, E. Pupka, M. Ščiuka, I. Kraujalienė, D. Tumosa, K. Juškevičius, A. Skrebutėnas, T. Tolenis, S. Kičas, R. Drazdys, R. Buzelis, and A. Melninkaitis, Effect of conventional fused silica preparation and deposition techniques on surface roughness, scattering, and laser damage resistance, Boulder Damage Symposium 23–26 September 2012, Boulder, Colorado USA [8530–61].

C16. H. Schröder, **G. Batavičiūtė**, and W. Riede, Multichannel laser-induced contamination test bench, Boulder Damage Symposium 23–26 September 2012, Boulder, Colorado USA [8530–35].

C17. A. Melninkaitis, J. Miraukas, **G. Batavičiūtė**, and V. Sirutkaitis, Automated test station for characterization of optical resistance with ultrashort pulses at multikilohertz repetition rates, Boulder Damage Symposium 23–26 September 2012, Boulder, Colorado USA [8530–67].

C18. H. Gebauer, M. Jupè, **G. Batavičiūtė**, D. Ristau, and R. Kling, Measurement of laser power resistance of fibers for PIV systems, Boulder Damage Symposium 21-23 September 2008, Boulder, Colorado USA [7132].

C19. J. Mirauskas, **G. Batavičiūtė**, and A. Melninkaitis, Pseudo accumulation effect on laser induced damage threshold on transparent materials with nanometer sized defects, Open readings 4 April 2008, Vilnius, Lithuania SD24, p. 71.

1 Literature overview of the laser-induced damage related phenomena

"When everything's made to be broken, I just want you to know who I am."
J. J. Theodore, guitarist and frontman of the rock band Goo Goo Dolls.

When an optical sample is exposed to intense laser radiation, it might become damaged (Fig. 1.1: top, left). Laser-induced damage (LID) is understood as **irreversible modification** of the properties of material (Fig. 1.1: bottom, A–C). According to the International Standard Organization (ISO) it is defined as:

> *"...any **permanent** laser radiation induced **change** of the surface characteristics of the specimen which can be observed by an inspection carried out with an incident light microscope having Nomarski-type differential interference contrast. A magnification in the range from 100× to 150× shall be used"* [9].

LID can form in the bulk material, on the surface of a sample or within optical coating (Fig. 1.1: top, right) [2, 3]. The ability of a material to withstand intense laser radiation is quantified as laser-induced damage threshold (LIDT). According to the ISO, it is:

> *"...the highest quantity of laser radiation incident upon the optical component for which the extrapolated probability of damage is zero where the quantity of laser radiation may be expressed in energy density, power density or linear power density"* [9].

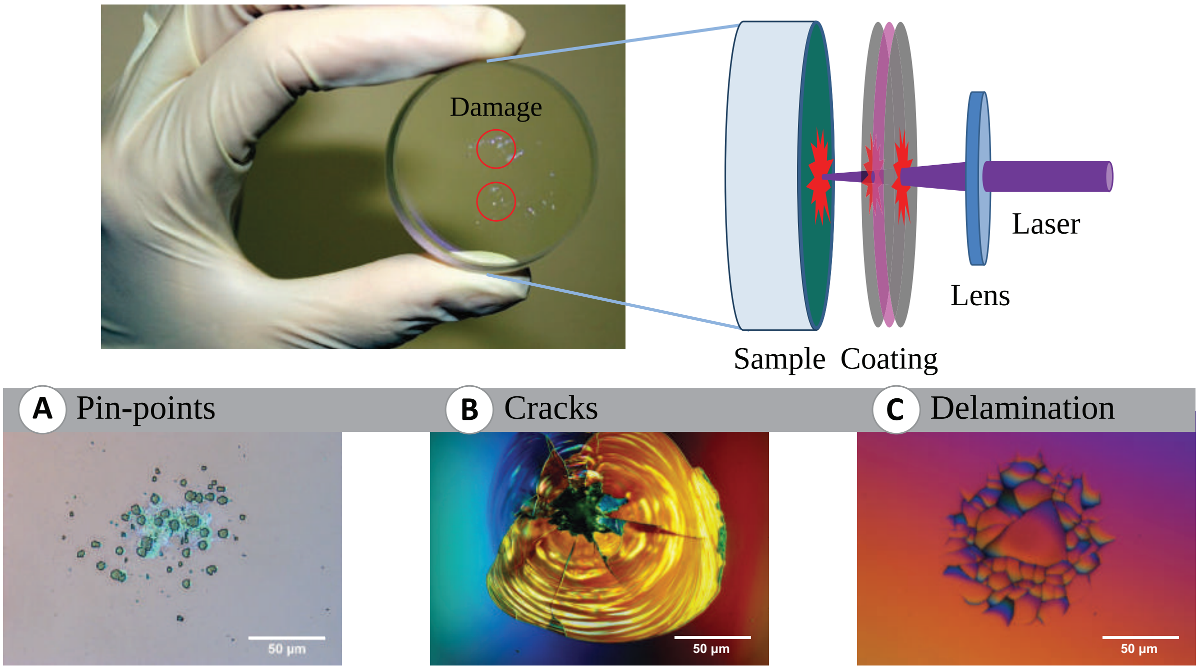

Figure 1.1 **Top, left:** example of possible locations for LID to occur. **Top, right:** LID on uncoated fused silica sample. **A–C:** images of typical LID in optical materials exposed at nanosecond pulse radiation. **A:** "pin-point" type damage. **B:** cracks induced by laser radiation on uncoated fused silica substrate. **C:** delamination of the coating on fused silica substrate with deposited multilayer thin film.

Though the LID is studied since the invention of the first laser [5–8], it is still not fully understood why, how and when the optical elements become damaged. It has been shown that the formation and growth of LID depend on:

- **laser radiation parameters:** wavelength [10–15], pulse duration [2, 16–19], spatial beam profile [51], temporal pulse profile [20], repetition rate [21] etc.;
- **environment conditions**: air, vacuum [24], temperature [25–27], contamination [22, 23] etc.;
- **material properties:** intrinsic [30] and extrinsic [28, 29] defects of the optical component, preparation method and shape.

Historically, the first attempts to explain the formation of the LID were related to a model of avalanche ionization and breakdown in solids, which had

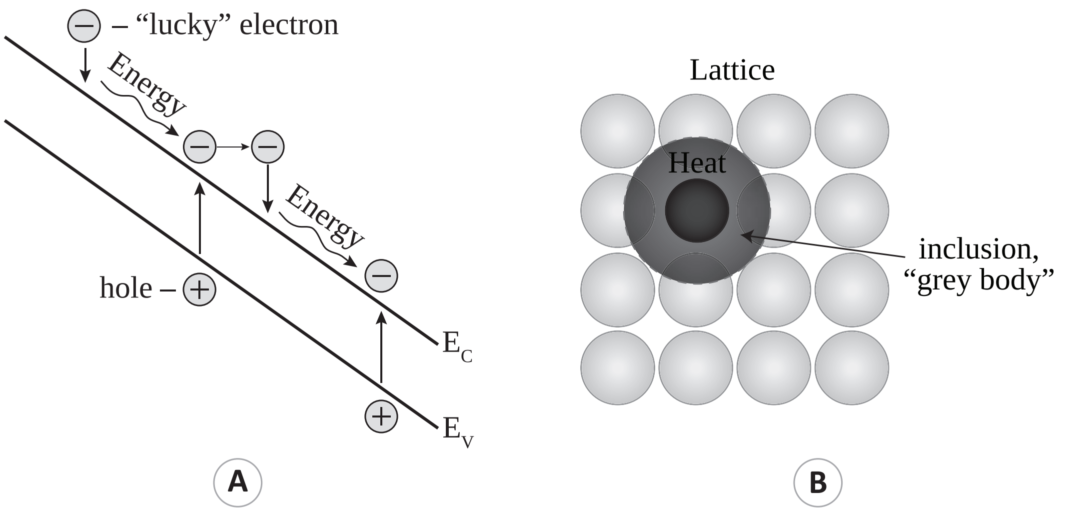

Figure 1.2 The models of LID mechanism. **A**: illustration of the "lucky" electron model based on impact ionization and avalanche multiplication. E_C and E_V represent the energies of conduction and valence bands, respectively. **B**: an illustration of the "grey body" model based on increased absorption by foreign particles.

the best agreement with experimental observations [52]. The pioneering work here was performed by N. Bloembergen, who introduced the "lucky" electron avalanche breakdown model [10], and A. S. Epifanov, who developed the most comprehensive theoretical investigation of LID growth dynamics based on the quantum kinetic equation [53–55]. According to the "lucky" electron model, it is assumed that some electrons are present in the conduction band before the laser pulse (Fig. 1.2: A). The free electrons oscillate in the laser fields and liberate additional electrons by the impact ionization. Electrons multiply in this manner until an opaque plasma is generated. The plasma facilitates rapid absorption during the remaining laser pulse. Based on this model, the damage threshold should increase at frequencies that are large compared to the inverse electron collision time, because of reduced coupling to the lattice.

However, soon this model experienced multiple setbacks. It has been shown to be incompatible with newly observed experimental data [11]. Then another model was suggested by M. Feit et al. [56]. In this case, the LIDT dependence was interpreted by introducing foreign particles in the crystal lattice, which form during material manufacture (Fig. 1.2: B). Such particles act as “grey bodies”. They absorb a fraction of incident radiation. The absorbed energy heats the surrounding host material causing the collapse of bandgap and plasma formation. This model was in a good agreement with the experimentally observed damage morphology recorded in the 3 ns regime [56]. Therefore, in order to investigate the intrinsic damage limiting processes, the elimination of extrinsic defects inherent via optical element manufacturing steps must be ensured. One can say that the LID research evolves together with the progress achieved in optical element production. The better (extrinsic defect free) the optical elements become, the more complicated damage mechanisms are revealed.

However, the “grey body” model is not universal. For instance, the LID at ultra-short laser pulses cannot be attributed to the thermal heating of foreign particles. Other mechanisms causing a nonlinear absorption, such as multi-photon ionization and tunneling, should also be considered as key factors in the damage process. Thus, in order to investigate the LID, it is necessary to understand the key features attributed to particular testing regime.

Research in this thesis is focused on the nanosecond LID at 355 nm wavelength. The laser source used for experiments operates in single mode regime. Testing is performed in clean air environment on four different types of optical elements: uncoated fused silica substrates (FS), FS with a deposited SiO_2 and HfO_2 monolayer coating, FS with multilayer highly-reflective HfO_2/SiO_2 coatings. The LID threshold of the optical elements operating in this regime is known to be limited by production-caused defects rather than by pure materials [3]. Formation of LID under these conditions is known to be the result of a sequence of complex physical processes involving:

- free carrier generation from linear or nonlinear ionization →
- absorption of the laser energy by the free electrons →
- energy transfer from the electron system to the lattice →

- and eventually irreversible modifications of the material through thermal or mechanical mechanisms.

In the following Sections a brief overview of the LID phenomena is presented. Mainly, it is focused on the LID occurrence in a specific range of interest for the thesis. However, to make the results widely adaptable, the selected range is compared with other testing regimes, environmental conditions and materials, thus emphasizing the differences and similarities that knowledge later provided in the thesis might be easefully applied in other cases.

1.1 Irradiation conditions

Since LID threshold of the dielectric materials is highly sensitive to many different external irradiation conditions, the qualitative understanding of one particular term can be achieved only by ensuring reproducible experimental results for well-defined materials. For instance, in order to investigate the LIDT dependence on wavelength, particular attention should be paid to the characterization of the temporal laser pulse and spatial laser beam profiles [57]. Also, self-focusing [10] should be avoided and the external absorbing inclusions [10, 11, 56] should be eliminated. It has been shown that if those issues are not addressed properly, they can lead to a variation in experimental results of nearly 2 orders of magnitude and make it impossible to perform a quantitative study [12, 58].

In order to damage a material that has an energy gap between the valence and conduction bands (semiconductors and dielectrics), it is necessary to supply enough energy to bridge this gap to promote electrons to the conduction band. Thus, the studies of LIDT dependence on wavelength and pulse duration are closely related to the LIDT dependence on the material bandgap [57, 59]. The energy absorption in dielectrics and semiconductors can be either linear or nonlinear, depending on the intensity and incident photon energy. In both cases, the result of the absorption process is the creation of free electrons in the material. Both (linear and nonlinear) absorption mechanisms initiate the excitation process by creating the seed electrons for an avalanche. The resulting free electrons may further absorb single photons and gain energy. Once electrons have gained sufficient energy, they can transfer energy to bound electrons by collisional excitation, thus generating other free electrons. This mechanism may start an avalanche process, which leads to the occurrence of physical damage [60].

1.1.1 LIDT dependence on wavelength

The search of LIDT dependence on wavelength in both nanosecond and femtosecond laser pulse regimes struggled for a long time. In the case of nanosecond pulses, the abovementioned models of “lucky” electron [10] and “grey body” [56] could not explain the observed experimental tendencies. Indeed, the “lucky” electron model did not predict any damage threshold dependence on the wavelength until the laser frequency approaches the inverse of the electron collision time. The “grey body” model has been valid for a while. According to this model, the damage is supposed to be initiated at the site of particles embedded during the optical element manufacturing. Consequently, the damage was expected to occur at discrete localized centers and not necessarily at the peak fluence of applied laser radiation. Thus, for a uniform particle size distribution, the “grey body” model predicted a smooth $1/\lambda$ LIDT dependence on the wavelength λ. A similar relationship was approved by multiple researches [12, 13]. However, these studies were carried out on a limited range of the spectrum. Later experiments performed by C. Carr et al. on DKDP crystals have shown that $1/\lambda$ dependence cannot be applied to the whole wavelength range in the nanosecond pulse regime

[14]. In this study, 50% damage probability fluence was obtained for 21 different wavelengths. There are sharp steps in the damage threshold centered at 2.55 eV (487 nm) and 3.90 eV (318 nm) (Fig. 1.3). The existence of those steps could be explained via defect-assisted multistep photon mechanism [14]. Defect states in the bandgap alter the cross section for multiphoton absorption, in fact turning the process into a series of reduced order absorptions. In the presence of intraband defect states, excited state absorption can reduce the order of the multiphoton process needed for an electron to make a transition to the conduction band. Whether the mechanism is a series of single photon absorptions or a mixture of single and multiphoton absorptions, this model accounts for sharp steps in the damage threshold. The width of steps is most likely governed by the thermal distribution of electrons in the valence band. Up till now this model of assisted multistep photon mechanism is the only one that is capable of explaining LIDT dependence on wavelength within a wide range of spectrum at nanosecond pulse regime.

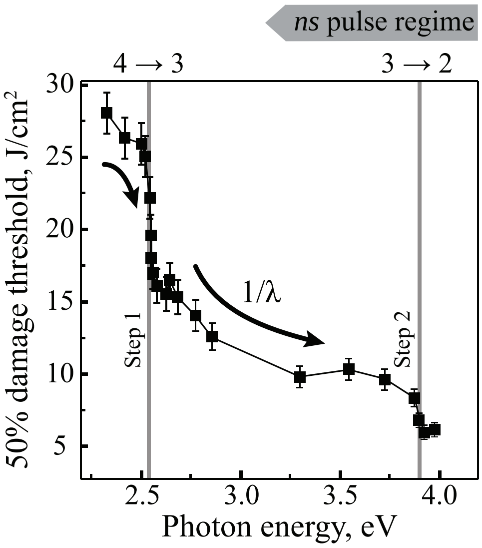

Figure 1.3 A wavelength dependent damage threshold of a DKDP crystal is obtained by plotting photon energy versus the fluence at which the sample is damaged 50% of the time. Transitions 4 → 3 and 3 → 2 mark the reduced order of multiphoton process needed for an electron to make a transition to the conduction band due to the existence of intraband defect states. Data are adapted from [14].

In the case of femtosecond pulse regime, the energy is absorbed by electrons faster than it is transferred to the lattice. The evolution of free electron density drives the LID. Photoionization is often modeled using Keldysh theory [61], which defines photoionization, tunneling and multiphoton ionization processes via relatively simple formalism. The free carrier absorption leading *fs* pulse regime

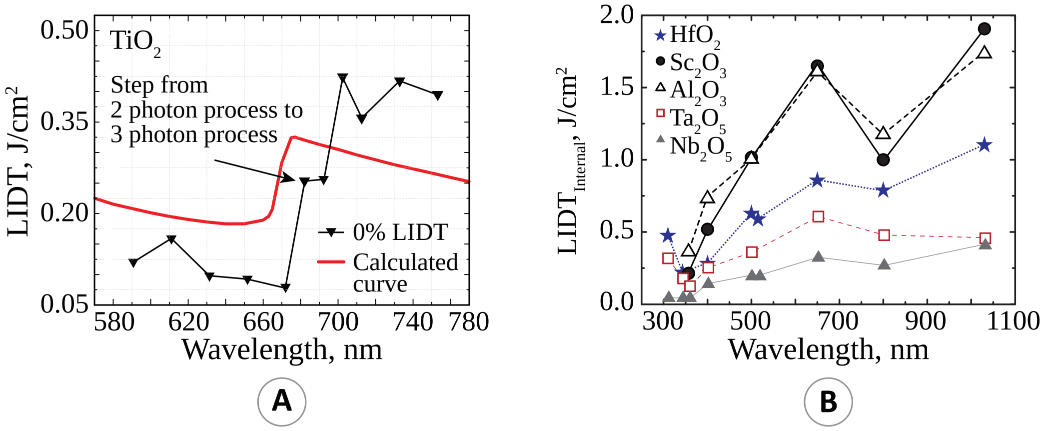

Figure 1.4 LIDT dependence on wavelength. **A:** data obtained from M. Jupé et al. [15]. **B:** data obtained from L. Gallais et al. [31].

to impact ionization and avalanche can be described by different models, such as single rate equation [57] or multiple rate equation [62]. Most recent studies about LIDT dependence on wavelength based on Keldysh theory and multiple rate equation modeling have been reported by two groups of researchers led by M. Jupé et al. [15] and L. Gallais et al. [31] (Fig. 1.4). Studies has been performed on different oxide thin films. M. Jupé et al. investigated TiO_2 single layer dependence on the wavelength (Fig. 1.4: A). Presented results show that below approximately 670 nm two-photon absorption is observed. At 680 nm the predicted step of the LIDT towards three photon absorption is evident. Thus, it has been shown for the first time, that in femtosecond case regime there is also a sharp step in LIDT dependence on wavelength, which is attributed to multiphoton ionization process. However, such dependence is hardly recognizable in experimental data reported by L. Gallais et al. (Fig. 1.4: B). In that research, 5 different monolayer coatings have been investigated: tantala, niobia, hafnia, scandia and alumina. In order to make the measured LIDT values comparable with testing in a bulk material, experimentally determined LIDT values have been rescaled taking into account the electric field distribution in the oxide films. The internal, or the so-called intrinsic, LIDT has been derived, which is the relevant value for comparisons:

$$\mathrm{LIDT}_{\mathrm{internal}} = |E_{\mathrm{max}}/E_{\mathrm{inc}}|^2 \cdot \mathrm{LIDT}_{\mathrm{measured}} \, , \tag{1.1}$$

where $E_{\mathrm{max}}/E_{\mathrm{inc}}$ is the ratio of maximum of the standing wave electric field distribution in the film to the incident one. The study claimed that taking into account the change in the dielectric function of the materials during the laser pulse and its consequences on the intensity distribution in the material, and then applying a critical energy level for the theoretical damage threshold, a fair description of the experimental data could be obtained, both for the localization of the damage initiation and the quantitative evolution of the damage threshold with photon energy and material properties. To go further, the influence of a third parameter such as the pulse duration should be analyzed to explore the range of validity of the approach and its limitations.

1.1.2 LIDT dependence on pulse duration

Laser damage sensitivity to applied laser pulse duration has been proven in multiple cases for dielectric materials [16, 17, 57, 59, 63]. Two pulse duration intervals can be distinguished here: nanosecond to picosecond pulses and picosecond to femtosecond pulses [57] (Fig. 1.5). In the case of nanosecond to picosecond pulses (also referred as long pulses), namely, in the range of 20 ps to over 100 ns (Fig. 1.5: A), a well-accepted mechanism of damage formation is based on conventional heat deposition [19]. Incident laser radiation heats electrons in the conduction band, then accumulated energy is transferred to the lattice on a time scale of pulse duration. This energy is then carried out of the focal volume by thermal diffusion. Damage occurs when absorbed heat is sufficient to trigger melting, boiling or fracturing processes. The occurrence of laser damage is defined via the relative rate of energy deposition and thermal diffusion. This model predicts $\tau^{1/2}$ dependence of threshold damage fluence upon a pulse duration τ [10, 16, 64]. It has been shown to be in a good agreement with many experiments [17, 19, 65–69]. Damage morphology recorded under long pulse irradiation approves the thermal nature of damage mechanism (Fig. 1.5: B). Usually, damage occurs over the entire irradiated area. Surface of optical elements is melted or fractured [57, 57].

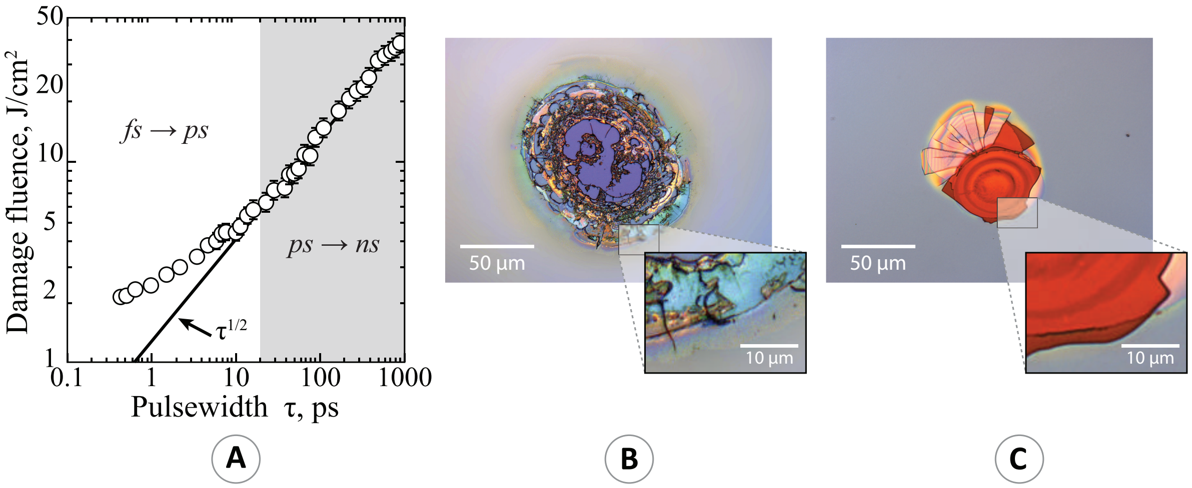

Figure 1.5 **A:** LIDT dependence on pulse duration in fused silica. Data adapted from [57]. **B, C:** typical morphologies of LID on fused silica at long and short pulse regimes respectively.

In the case of ultrashort pulses (tens of picoseconds to femtoseconds), also known as sub-picosecond pulse regime (Fig. 1.5: A), the thermal model is no longer acceptable because absorption occurs on a time scale much shorter than needed for energy transfer to the lattice and resulting heating processes. In the range of 10–20 ps to fs, departure from $\tau^{1/2}$ dependence has been observed [19, 57, 70]. Damage mechanism in ultrashort pulse range was first suggested by B. C. Stuart et al. [57]. It assumes that electrons in the conduction band are heated by the laser pulse much faster than they can cool by phonon emission. Two processes take place in the generation of conduction band electrons: photo-ionization and avalanche ionization. They can go together or one of them can be dominating. For instance, photo-ionization by the leading edge of a laser pulse provides the seed electrons for avalanche ionization during the rest of the pulse. Then, electron density grows through avalanche ionization – until plasma frequency approaches the frequency of incident laser radiation – achieving what is also known as the "critical" plasma density [57].

1.1.3 LIDT dependence on temporal pulse shape

LIDT was also shown to depend on temporal pulse shape in both nanosecond [20, 71, 72] and femtosecond [73] laser pulse regimes. In the case of nanosecond pulses, it has been revealed that longitudinal mode structure has an impact on both damage morphology and LID probability curve for uncoated samples [20, 71, 72]. $\tau^{1/2}$ scaling law is unable to explain observed differences when comparing damage probability curves obtained under single- and multi-longitudinal mode laser radiation. Characterization of effective pulse duration is insufficient for temporal pulse definition in damage probability measurements. Longitudinal mode structure should also be taken into account when multilongitudinal mode laser radiation is used [20, 71]. Additionally, qualitative differences in damage morphologies are reported [20, 71] (Fig. 1.6).

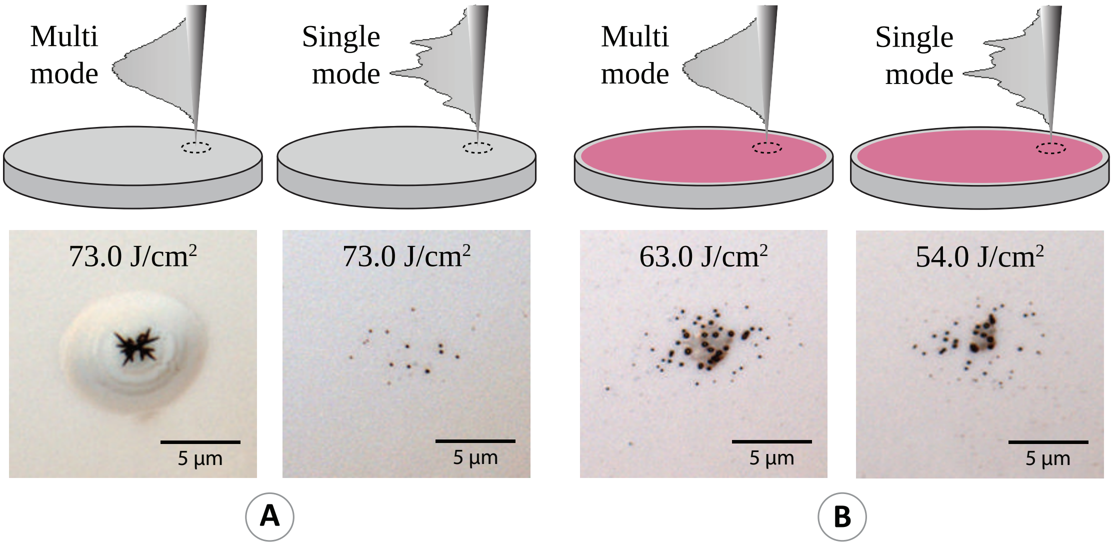

Figure 1.6 LID morphologies recorded for uncoated (**A**) and coated (**B**) fused silica samples when irradiated under single and multilongitudinal laser radiation [20].

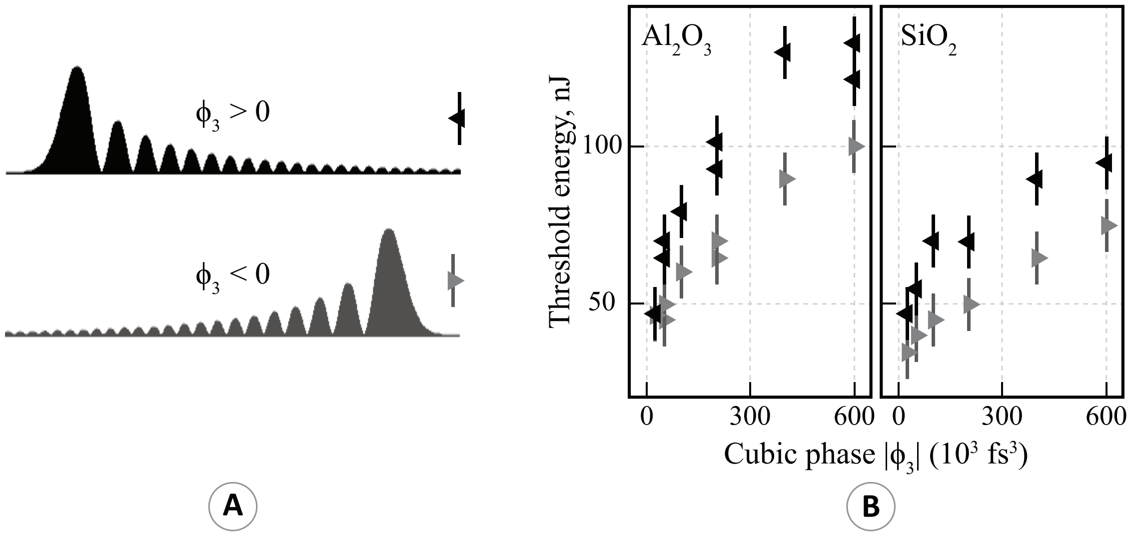

Figure 1.7 **A:** asymmetric temporal pulse shape used for tailoring measurements. **B:** LID thresholds recorded for different temporal pulse shape.

In the case of uncoated fused silica substrate tested at 355 nm wavelength multilongitudinal mode irradiation, damages of different diameters are formed from radial cracks in the center and surrounding rims (Fig. 1.6: A, left). They significantly differ from damages observed when the same sample exposed at single-longitudinal mode irradiation (Fig. 1.6: A, right). For coated samples, no difference in damage morphologies was observed. This indicates possible changes in damage formation mechanism.

In the case of femtosecond pulses, the influence of pulse shape was demonstrated in the research of L. Englert et al. [73]. Two optical samples, sapphire and fused silica (FS), have been exposed to temporally asymmetric pulses of identical fluence, spectrum and pulse duration (Fig. 1.7: A). Shaped pulses are characterized by the implemented phase functions occasionally checked via direct cross-correlation measurements, which are described in detail in ref [73]. One pulse featured tailoring before the peak (positive cubic phase ϕ_3>0) and another pulse featured tailoring after the peak (negative cubic phase ϕ_3<0). It has been proved that for asymmetrical pulses the final free electron densities differ. For pulses with tailoring before the peak the total free electron density increases strongly at the beginning of irradiation and further gradual increase at the end of the laser pulse. In contrast, for pulses with tailoring after the peak, the total free electron density increases only by the end of the laser pulse, when the peak intensity of the pulse train is reached. This results in the observation of different thresholds for surface material modification in sapphire and fused silica (Fig. 1.7: B). The observed threshold is shown as a function of the cubic phase parameter [73]. Damage threshold has been found to be lower for the pulse with pulse tailoring after the peak. Therefore, femtosecond pulse tailoring provides a possibility to control the transient free electron density until the critical density for dielectric breakdown is reached. This opens the route to develop tailored pulse shapes for controlled nanoscale material laser processing of dielectrics. Nevertheless, more investigations are required in this field to conclude LIDT dependence on temporal pulse shape.

1.1.4 LIDT dependence on beam diameter

The LIDT dependence on laser beam diameter has been acknowledged since the early studies of optical resistance [43, 74–76]. Three quantitative models have been developed to explain observed dependences: the point defect model [74], the heat accumulation model [77, 78] and the plasma shielding effect [79].

Point defect model

This model mostly applied to explain the LIDT dependence on beam diameter in the case of single pulse LIDT measurements carried out in nanosecond and picosecond pulse regimes. It is based on the assumption that the surface of a material is covered with randomly distributed point-sized defects [74]. When beam diameter used to test the LIDT of the material is decreased, the probability to hit a defect is also reduced. The damage probability and the beam diameter on the sample surface in the focal plane can be related via Poisson statistics [43, 74–76]. When measured with smaller beam diameters, the effect of an increased LIDT is fully dependent on the achieved coverage of the tested surface. This means that the number of test sites should be greatly increased in order to result in equal damage threshold [80]. In contrast to the prevailing opinion, A. V. Smith et al. found no difference of LIDT values in nanosecond pulse regime when beam diameters varied in a small range (8–16 μm) [72]. They suggested that self-focusing and stimulated Brillouin scattering are more likely to complicate LIDT measurements.

Heat accumulation model

This model is mostly attributed to multipulse LIDT measurements in ultrashort pulse regime. In the case of small beam diameter, heat diffusion into the bulk is hemispheric and in the case of large beam diameter, diffusion is mainly linear. According to this model, cooling is more efficient for smaller beam diameters. B. M. Kim et al. [77] observed that at small beam diameters – 130 μm, determined at full width at half maximum (FWHM) intensity level — the thresholds were not affected by repetition rates tested at 100, 500 and 1000 Hz. As the beam diameter becomes larger (175 and 260 μm) , the effect of repetition rate becomes significant and the threshold decreases. However, at low repetition rates (below 100 Hz), the thresholds were not significantly dependent on beam diameter. Studies concluded that observed dependence can be explained via the heat accumulation rather than the incubation of electronic defects. Thus, thermal damage can be important for high repetition rate ultrashort pulse laser ablation.

Plasma shielding effect

The ablation rate (i. e. the ablation depth per pulse) dependence for different materials is explained as a function of the laser beam diameter. Studies were reported by B. Wolff-Rottke et al. [79]. The experiments were performed with excimer lasers at two pulse durations (24 ns and 500 fs), three wavelengths (193, 248 and 308 nm) on three types of samples (polymers, aluminum oxide ceramics and glasses) under vacuum and regular atmosphere conditions. It was concluded that in the case of nanosecond pulse regime the ablation rate decreases for larger beam diameters while in the case of femtosecond pulse regime there is no such dependence. In order to explain these results, plasma shielding effect was introduced [79]. It has been shown that incident laser beam is attenuated by absorption and scattering on the ablation plume in the case of nanosecond pulse irradiation. The ablation plume is expanding with a certain angle distribution over the surface of the target and only the central portion of the plume will interact with the nanosecond laser pulse. In general, the smaller the size of ablated spot, the smaller the relative part of the ablated material that falls within the laser beam path, thus the smaller overall shielding effect [79, 81]. In the case of femtosecond pulse irradiation, no ablation plume develops during the laser pulse, thus no dependence on beam diameter is observed [79].

1.1.5 Fatigue effect

In practice, most optical elements work under multipulse laser irradiation. When optical element is exposed to an increasing number of pulses S, damage occurs at lower fluences as compared to single-pulse irradiation [82–94]. This is the so-called “fatigue effect” or cumulative damage. There are at least four different models which explain this phenomenon: “Statistical fatigue interpretation” [82–84], “fatigue interpretation via material modification” [88, 92], “fatigue interpretation via thermal accumulation” [77, 78], and “statistical pseudo-fatigue” [91, 95].

Statistical fatigue interpretation

According to this model, fatigue effect can be explained by a probability for LID to occur [82–84]. As mentioned previously, the first model explaining damage occurrence was based on the “lucky” electron model. It was assumed that free electrons of unspecified origin are forced to undergo repetitive accelerations and collisions with lattice under the driving influence of the incident laser field. The average free electron gains little energy from the applied field since the collisions are frequent. Occasionally, it obtains ionizing energy through a sequence of “lucky” momentum-reversing collisions and accelerations. Avalanche breakdown occurs once a single electron in the focal volume is capable of ionizing its surrounding. Based on this model it was suggested that, if the applied laser fluence is stable, there is a constant probability p_1 that a damage will be produced by a single pulse. Then, the probability that the damage will be produced by Nth pulse, is given by

$$p_N = (1 - p_1)^{N-1} \cdot p_1 \, , \tag{1.2}$$

where p_N defines the composite probability that there are exactly $N - 1$ non-damaging pulses followed by one that caused the damage. However, experimental evidence that could not be explained by this model was gradually acucumulated [85–87]. It was suggested that the statistical fatigue interpretation is influenced by extrinsic defects, such as absorbing inclusions or structural inhomogeneities. Threshold fluence of the extrinsic defect is lower than the same expected for pure host material. Thus, when testing different sites on the optical component, there is always a possibility to hit a coarsely spaced damage precursor. Then damage will be induced by extrinsic defect and not due to cumulative processes. Inability to distinguish between intrinsic and extrinsic defect induced damage was the major drawback for the statistical fatigue interpretation. However, in recent studies it has been shown that if executed with care the statistical interpretation of fatigue effect model might still be applicable [91].

Fatigue interpretation via material modification

In 1983 L. D. Merkle et al. showed that damage probability with increasing number of pulses can be predicted by Poisson distribution [86]. The action of each pulse is an event dependent on the prior irradiation. It means that even “non-damaging” pulses enable one to modify the material. Within the scope of that research, it was also revealed that a “safe” (non-damaging) fluence, at which no large number of pulses could produce catastrophic damage, exists [86]. Irreversible changes in transparent materials were proven experimentally by several methods. At first, it was shown that light scattering from the surface [96] and from the bulk [97] of dielectric material increases with increased number of pulses. The latter effect points out a nonlinear character of the scattering process. One can consider it as a direct evidence of the material modification within the passing laser pulse. Furthermore, studies based on infrared spectroscopy concluded that the breaking of chemical bonds in glasses appears when optical equipment is exposed to multipulse laser irradiation at fluencies close to the threshold fluence (sub-threshold fluences) [98]. It was also shown that the presence of pre-existing broken bonds affects the optical strength [99]. Spectroscopic investigation led to a conclusion that in multicomponent glasses, only the breakage of the glass-forming chemical bonds reduces the damage threshold, while the breaking of bonds involving glass-modifying atoms (such as Na, K, etc.) has no significance for the laser strength [88]. By employing pump and probe measurement with ultrashort pulses, the time limit of irreversible changes in solids (including the forming of broken chemical bonds [100]) has been established. The average lifetime of photo-generated carriers in the conduction band of crystalline and amorphous SiO_2 is of the order of 150 fs [101]. This time interval is sufficient to generate a defect population which can grow under repeated laser shots. However, in some femtosecond experiments, no sub-threshold damage in glasses and crystals [102] was observed. This led to the conclusion that some restrictions exist for the cumulative process.

Fatigue interpretation via thermal accumulation

Fatigue effect might be also attributed to the heat accumulation caused by pulse-to-pulse temperature increase [77, 78]. The laser energy deposited in the material will ultimately be transferred to the lattice and converted to heat, resulting in a local temperature rise. The temperature of the lattice grows when pulse repetition rate is high enough to ensure that the time interval between incident laser pulses is shorter than the time required for heat diffusion. The typical heat diffusion time is of the order of ~ 1 μs [103]. The longer material is exposed to a train of pulses, the higher the temperature rises and the larger region is heated. The energy is accumulated around the focal volume until the material is melted, evaporated or experiences other structural changes. Thus, heat accumulation caused fatigue effect becomes significantly important in multipulse experiments at high repetition rates (up to 1 Mhz). However, LID formation is highly dependent on factors such as absorption and thermal diffusivity, so there is no reliable method for determining when a high repetition rate laser will damage an optical element due to thermal effects.

Statistical pseudo-fatigue

The statistical pseudo-fatigue effect is caused by the measurement uncertainty – pulse-to-pulse fluctuations of laser energy and depointing of the laser beam on the optical element surface [91, 95]. Such instabilities during the measurement increase the probed volume during multipulse LIDT experiments. The probability to hit a defect within a larger area is higher. Thus, the probability of causing damage increases with increasing pulse number. The influence of this effect exists in addition to any true physical accumulation in the sample.

1.2 Environment conditions

This study is limited to LID investigation in air environment and room temperatures. However, it is advantageous for some laser systems to operate under hostile conditions such as vacuum or low temperatures. The changes of the LID phenomenon when altering different environmental conditions have been addressed by numerous studies. Three most common environmental factors that affect the LID behavior are discussed: vacuum [24, 104–116], laser-induced contamination [23, 117, 118] and low (cryogenic) temperatures [25–27, 119–122].

1.2.1 LID phenomenon in vacuum

In the nanosecond pulse regime parallel testing of the dielectric coatings, which include anti-reflective (AR) coatings, highly reflective (HR) coatings and dichroic mirrors, showed a distinct decrease of LIDT under vacuum compared to atmospheric environment [24, 109, 114]. Differences were also observed in recorded damage morphologies. Neighborhood of the damaged site in vacuum is free of debris, whereas typical laser damage in air features tiny molten droplets, which were emitted from the damaged spot and redirected back to the surface [109, 111, 114]. The depth measurements of damage sites showed that the damage in atmosphere environments is mainly within the top layer, while the damage irradiated by the same laser fluence in vacuum deepens below the top layer [112]. The degrading effect was found to depend on the residence time [109]. The longer the dielectric coating was exposed to vacuum prior to the measurement, the more distinct degradation of optical resistance was observed. Porous dielectric coatings degraded in vacuum more than dense ones. LIDT of electron beam (e-beam) evaporated coatings significantly decreased under vacuum, while coatings produced by ion-assisted deposition (IAD) or ion beam sputtering (IBS) offered a good, independent of the environment conditions damage threshold stability [24]. It was hypothesized that a local strain in the film induced by adsorbed water reduces the damage threshold [24]. It was also suggested that an increased coupling of the plasma shockwave in a vacuum which has low gas pressure should be also considered as a possible cause of low LIDT [112]. Continuing studies are needed in order to fully understand the laser damage degradation in the vacuum.

In femtosecond pulse regime no differences were observed on single pulse LIDT of dielectric oxide films (hafnia and silica) in vacuum. However, multiple pulse threshold decreased with decreasing atmospheric pressure. The decrease has been shown to correlate with the water vapour and oxygen content of the environmental gas [113]. It is most likely associated with the accumulation of defects derived from oxygen deficiency, for example, vacancies. Damage morphologies also differ. Typical fs laser damage at atmospheric air pressure starts deterministically at the center of the beam and grows in diameter as the fluence increases. Under vacuum, damage morphologies changes for some materials. In hafnia films damage will be initiated at random sites within the exposed area. These sites are most likely created at predisposed sample locations (for example, boundaries between different material phases) as a result of charging the film surface under laser radiation [113]. This produces absorbing states distributed randomly across the film. In contrast, damage morphology remains deterministic in silica films, which are known to exhibit a greater degree of amorphousness than hafnia films. [113]. As in nanosecond pulse regime more work should be carried out to characterize effect of vacuum environment for femtosecond LIDT.

1.2.2 Laser-induced contamination

Laser-induced contamination (LIC) [23, 118] is the formation of a deposit on the surface of an optical component due to the interaction among laser beam, the surface of the optical component and the outgassing from nearby materials. Only molecular contamination is considered here, excluding particulate contamination. Optical sample deposited with organic contaminants incur transmission losses and catastrophically degrades in optical resistance performance. LIC is mostly evident in high-vacuum laser systems. Although a vacuum is considered to be an empty space, practically the ability to create and maintain a high-quality vacuum depends on the materials used in the sealed system. For instance, polymers and epoxies start to outgas in low-pressure [117]. The deposit growth is proposed to be the result of photochemical and photothermal mechanisms [118, 123]. Structure [124, 125] and growth rate [124–126] of laser-induced contamination strongly depend on applied fluence and irradiation. LIC is mostly observed in the UV range [23, 127, 128]. In order to prevent LIC, no outgassing materials (only metals and ceramics) should be used in the systems. Practically this task is hardly achievable considering the weight, price, and construction requirements for nowadays laser systems. Alternative solution is the reintroduction of oxygen into the vacuum chamber [129].

1.2.3 LID phenomenon at low temperatures

Dramatic improvements in laser characteristics have been achieved via cryogenic cooling [130, 131]. For instance, much higher efficiencies are obtained from cryogenically cooled Yb:YAG crystal, because low temperatures turn the quasi-three-level system into four-level system [132]. This leads to the increased interest in the LIDT dependence on temperature. Up till now results are inconclusive. Primarily experiments reported in 1978 showed that LIDT of NaCl increases with decreasing temperature when exposed to ruby and CO_2 laser radiation. However, LIDTs measured with Nd:YAG laser remained constant [119]. Also, no evident LIDT dependence on temperature was recorded for bulk damage in crystalline quartz, fused silica, and BK7 borosilicate glass tested with Q-switched Nd:YAG laser at two wavelengths (1064 and 532 nm) in nanosecond pulse regime [120]. In contrast, a scientific group from Osaka University led by K. Mikami reported a series of researches that have proved otherwise [25, 26, 121, 122]. Their results have clearly shown that LIDT of bulk damage in silica glasses increase linearly with decreasing temperature both at 1064 and 532 nm wavelengths. Linear dependence was related with changes of stimulated Brillouin scattering at a different temperature [122, 133]. Later the same group demonstrated the LIDT dependence on temperature for a glass surface, single-layer optical dielectric and metal coatings [25]. LIDTs for dielectric coatings linearly increased, while damage thresholds for metal coatings linearly decreased by cooling. Such behavior was explained via two opposite processes. At low temperature, the free electron generation and electron multiplication decrease, resulting in an increase of damage threshold in the dielectric materials, but the plasma heating increases, thus causing a decrease of damage threshold in metal coatings [25]. Further, dielectric coatings were tested for the LIDT dependence on temperature, with varying the pulse width from femtosecond to nanosecond regimes (Fig. 1.8) [26].

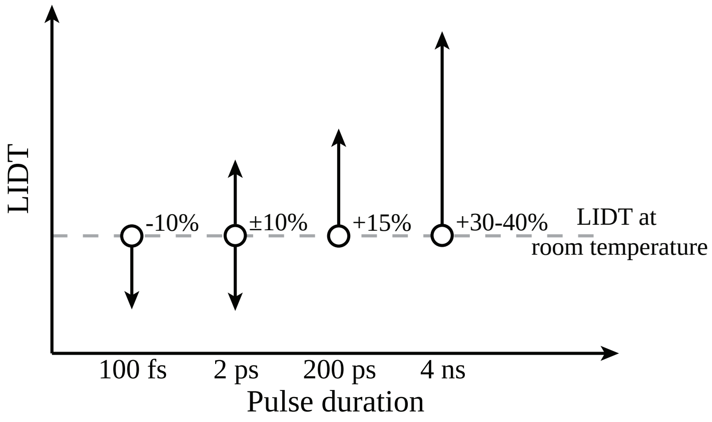

Figure 1.8 The trend in LIDTs in respect to decreasing temperature and different pulse duration. The representative scheme is based on results presented in [26].

For pulses longer than few picoseconds (namely, 4 ns and 200 ps in Fig. 1.8), the LIDT of coated substrates increased with decreasing temperature. This dependence was reversed for ultrashort pulses (namely, 100 fs in Fig. 1.8). At 2 ps laser pulse, the LIDT dependence on the temperature becomes sensitive to coating materials. Two theories have been introduced to explain the LIDT dependence on pulse duration under cryogenic temperatures [26, 27]. The first one assumed that for pulses longer than few picoseconds, the initial temperature influences the generation of free-electron, electron avalanche, and critical electron density, which are responsible for the increased LIDTs [26]. The second theory suggested that heat deposition in the lattice causes the temperature of the lattice to rise: the lower the temperature of the lattice is, the higher is the LIDT [27]. This model is in a good agreement with experimental results.

1.3 LIDT dependence on material properties

1.3.1 LIDT dependence on bandgap

The LIDT dependence on bandgap in femtosecond laser pulse regime has been closely investigated by M. Mero et al. [21]. Experiments were carried on various optical elements: different oxides (niobia, tantalum oxide, hafnia, scandia, aluminum oxide, silica), calcium fluoride, and zinc selenide in femtosecond laser pulse regime. The studies concluded that the breakdown fluence at a constant pulse duration shows an approximately linear dependence on the bandgap energy (Fig. 1.9: A).

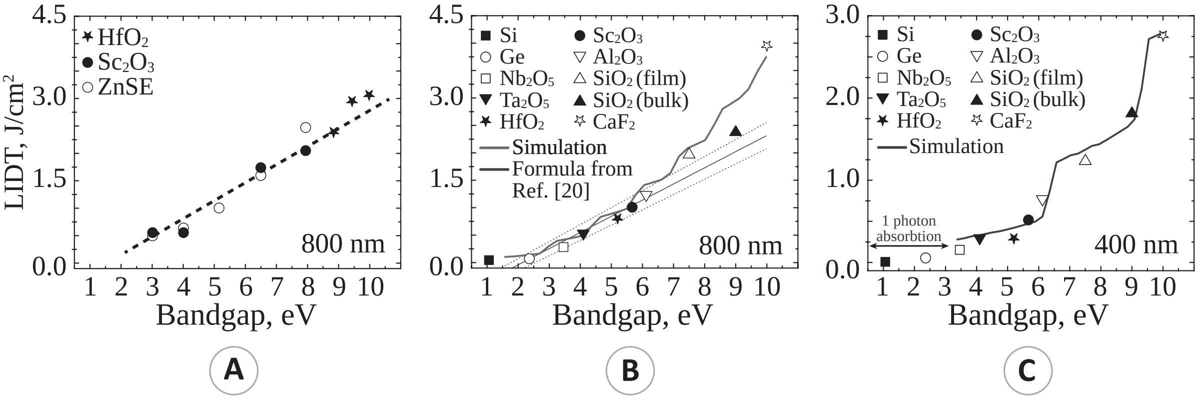

Figure 1.9 **A–C** LIDT dependence on material bandgap. **A**: data obtained from measurements performed by M. Mero et al. [21]. **B, C**: data are obtained from measurements performed by L. Gallais et al. [31].

Photoionization was identified as the process that controls this behavior. Similar dependence has been recognized in L. Gallais et al. studies at the same wavelength (Fig. 1.9: B) [31]. However, a linear approach has been shown to be valid only for a limited number of materials. In the case of high bandgap materials (calcium fluoride in this case), there is a deviation from this linear relationship. Different behavior is also observed for 400 nm wavelength (Fig. 1.9: C). Experimental results reveal a decrease of the damage threshold with the wavelength with a dependence on the bandgap of the material. In order to explain these results numerical model based on nonlinear ionization processes have been applied using Keldysh photoionization theory and the description of impact ionization by a multiple-rate equation system. The model is described in details elsewhere [31]. It shows that fair description of the experimental data could be obtained both for the localization of the damage initiation and for the quantitative evolution of the damage threshold with photon energy and material properties.

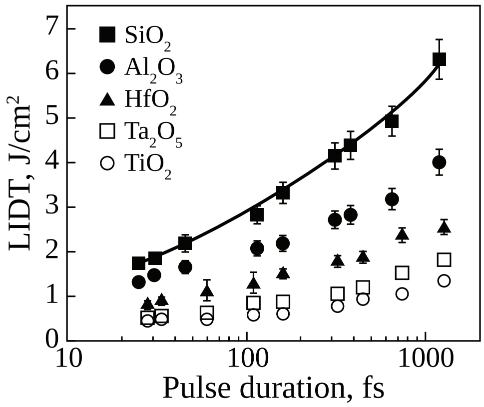

Figure 1.10 Incident laser fluence at which dielectric breakdown occurs measured as a function of the pulse duration for five oxide films. Data are adapted from [21].

The scaling of the threshold fluence with pulse duration was demonstrated on five oxide films (Fig. 1.10). It is interpreted by a phenomenological rate equation model containing three material-dependent figures of merit: the multiphoton absorption coefficient, the impact ionization parameter, and an effective relaxation time of conduction band electrons [21]. For each material, the breakdown fluence scales as $\tau_p k$, where $k < 0.3$, and, therefore, it is rather independent of the actual bandgap energy. Based on the values of the fit parameters in the phenomenological model, such behavior was attributed to a dominant contribution of the avalanche ionization to the carrier excitation even at pulse durations as short as few tens of fs. The breakdown fluence at a constant pulse duration shows an approximately linear dependence on the bandgap energy. Photoionization was identified as the process that controls this behavior. These findings for the oxide films suggested a phenomenological formula [21]

$$F_{\mathrm{th}} = (c_1 + c_2 E_{\mathrm{g}})\tau_p^k \,, \tag{1.3}$$

where the threshold fluence, F_{th} is determined only by the bandgap of the material, with a possible additional factor that depends on the material type and growth process.

1.3.2 Influence of production-caused defects on LIDT

A perfect optical component simply does not exist. As mentioned in previous chapters, nanosecond LIDT is mainly limited by the damage precursors (defects) inherent to the optical element manufacturing processes. Defects related to sample properties can be intrinsic or extrinsic (Fig. 1.11). Intrinsic defects are perturbations in a perfect atomic structure of a pure material. In the case of quartz, those are various stoichiometric imperfections formed within the optical element production processes or induced by applied laser radiation [30, 134–139]. Intrinsic defects are sometimes called native defects because they are a fundamental parameter of the pure material and set the ultimate limit to the highest possible laser-induced damage threshold value. Extrinsic defects are inherent to optical element production processes: glass shaping, polishing, cleaning and deposition procedures [28, 29, 41, 42, 140, 141]. These are impurities (usually isolated nm size particles) that result in band tail states and surface states (film interfaces and grain boundaries), scratches, pits, fractures and other macro and microscale structures that are formed or embedded during the external treatment of the material. Extrinsic defects can be controlled, minimized and in some cases eliminated. Within the scope of this study, an overview of the most common defect types related to laser damage phenomenon in dielectric materials is provided in following Subsections.

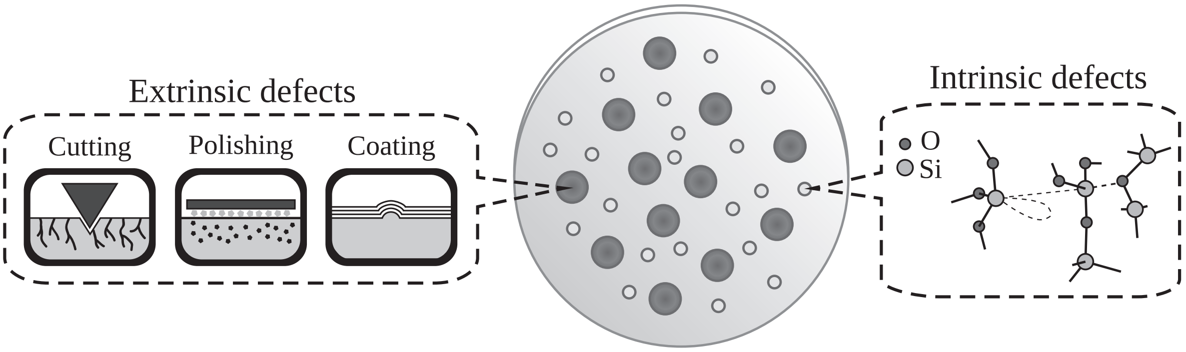

Figure 1.11 Representation of basic defects present in a coated optical glass sample. Extrinsic defects are inherent to production processes such as glass shaping, polishing, coating etc. Intrinsic defects are stoichiometric imperfections induced in electronic structure.

Physical properties of defects can be investigated by several destructive and non-destructive techniques [142, 143]. Destructive methods involve physical modification in components to expose the structure below the ground surface. It is commonly used to explore physical properties of the subsurface defects (SSD). In order to observe the subsurface defects directly, they should be "opened" and enlarged. A good example here is polishing. It is assumed that the polishing process induces little additional damage to materials, thus it is commonly used to obtain the morphology of subsurface defects [144–146]. Another major kind of destructive techniques is chemical erosion. The recently developed chemical etching method measures the variations in surface roughness with the etching time or material etched away [147]. Etching of the material enlarges the profiles of subsurface microcracks. Enlarged cracks can be readily tested with suitable contact stylus or optical profilometer [147–149]. The cross-sectioning by focused ion beam (FIB) milling procedure can be used to observe both subsurface [150–152] and nodular defects [141, 153]. Subsurface cracks can also be investigated by dye impregnation. The dyes contrasting in colour against the optical substrate or contrasting against substrate after being irradiated with X-rays, laser, etc. can be pressed into the materials [154–156]. Besides the dyes, quantum dots might be also used for this purpose [157, 158]. Then the properties of the subsurface defects are analyzed by examining the intensity of fluorescence signal. All destructive identification techniques are usually time consuming and tedious. In addition, they inspect only the localized areas and unavoidably destroy the tested substrate. As a consequence, a variety of methods are developed to evaluate the defects (especially SSD) non-destructively. For instance, subsurface damage can be related to surface roughness when the glass is ground in brittle removal mode [144, 159–161]. A common choice for non-destructive defect analysis is the application of numerous surface analysis techniques such as laser-modulated scattering [162, 163], total internal reflection microscopy [164–166], optical coherent tomography [167–171], white light interferometry [172, 173] and high-frequency scanning acoustic microscopy [174]

Intrinsic (bulk) defects

Intrinsic defects are stoichiometric imperfections in the electronic structure of the material. They can exist as an internal property of the nascent material or they can be induced by the applied laser radiation (especially with intense ultrashort pulses) [175]. In general, the energy absorbed by a solid material can be converted into elementary electronic excitations – electrons and holes, which relax and reduce their energy inside the solid through both delocalized and localized carrier–lattice interaction channels [175]. In the case of wide gap dielectric materials, the most important relaxation mechanism is the localization of the energy stored in the electron-hole pair that creates a self-trapped carrier, which provides energy necessary for a localized lattice rearrangement and thus, defect accumulation. A good example there is a self-trapped exciton – STE. Optical excitation can be sufficient to generate vacancies and interstitials in a perfect dielectric lattice, due to the existence of STEs. The most common intrinsic defects, related to laser damage phenomena in silica, are the so-called colour centers [30, 135–137]. The colour center is formed when an anionic vacancy in a crystal is filled by one or more electrons (Fig. 1.12: A). Electrons in such a vacancy absorb the incident light, thus a material that is usually transparent becomes coloured (Fig. 1.12: B). The colour is the result of the absorption of a photon by the trapped electron and the colour center excitation from the ground state to an excited state. Formation of the colour centers is associated with ion excitation and displacement from their normal crystallographic positions, leaving behind some electrons in the vacated spaces.

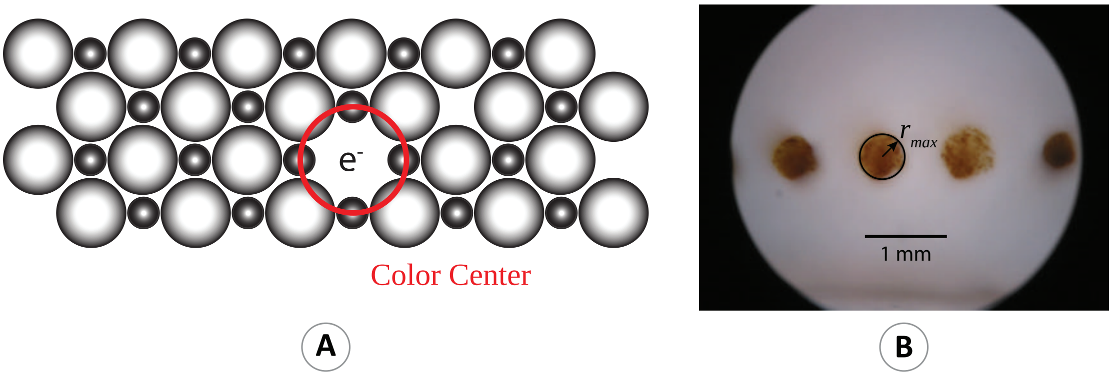

Figure 1.12 **A:** colour center – a point defect in which an electron (e^-) occupies an anion vacancy in lattice. **B:** image of colour center tracks induced by ultrashort (60 fs) high intensity (10 GW) laser pulses in LiF single crystals. Images are recorded with an optical microscope [137].

In the case of synthetic silica, colour centers form due to oxygen deficiency or excess [30, 136]. Oxygen deficiency related defects (also known as vacancies) are the family of different paramagnetic oxygen monovacancies with a trapped hole (known as E′ centers) and two kinds of diamagnetic “oxygen deficiency centers”, most commonly denoted as ODC(I) and ODC(II) [30]. These defects are known to dominate the induced optical absorption spectrum in glassy silica at 5.8 eV (E′ centers) and 7.6 eV (ODC(I)). Up till now ODC(I) is known to be the lowest-energy oxygen-deficiency-related defect in silica. Oxygen-excess-related defects (also known as interstitial) are mostly associ-

Table 1.1 Basic intrinsic defects in α-quartz, glassy silica and on the surface of SiO_2 [136].

Defect	**Structure**	**Absorbtion range**	**Surface**	**Bulk**
E′ centers	$\equiv$ Si$^{\bullet}$Si $\equiv$	—	Yes	Yes
ODC (I) – O vacancy	$\equiv$ Si-Si $\equiv$	UV* (VUV**)	Unknown	Yes
ODC (II) – divalent Si	$\equiv$ Si-O-Si-O-Si $\equiv$	UV (VUV)	Yes	Yes
Oxygen dangling bond	$\equiv$ Si-O$^{\bullet}$	—	Yes	Yes
Peroxy radical	$\equiv$ Si-O-O$^{\bullet}$	—	Yes	Yes

* Ultraviolet spectrum range.

** Vacuum ultraviolet spectrum range.

ated with oxygen dangling bonds denoted also as non-bridging oxygen or non-bridging oxygen hole center (NBOHC). It has strong UV absorption bands at 4.8 eV [30]. Oxygen deficiency and excess related defects are known to form both on the optical sample surface and in the bulk material. Basic examples of intrinsic defects are summarized in Table 1.1 [136].

Changes in the electronic structure of the material can also occur due to impurities or dopants. Despite the fact that the synthetic SiO_2 glass is often referred to as a "high purity silica", it still contains significant quantities (up to 1000 parts per million, ppm, or more) of chlorine or hydrogenic impurities, depending on its type [30]. Glasses are doped with fluorine in order to improve their spectral characteristics and radiation resistance [30]. For example, the silica glasses co-doped with fluorine and hydrogen have the best vacuum UV transparency.

Extrinsic (surface) defects

Extrinsic defects are associated with optical element manufacturing techniques (Fig. 1.13). It all starts with a raw material. Any substrate should be shaped and polished. This is a vital but also a harmful procedure that causes

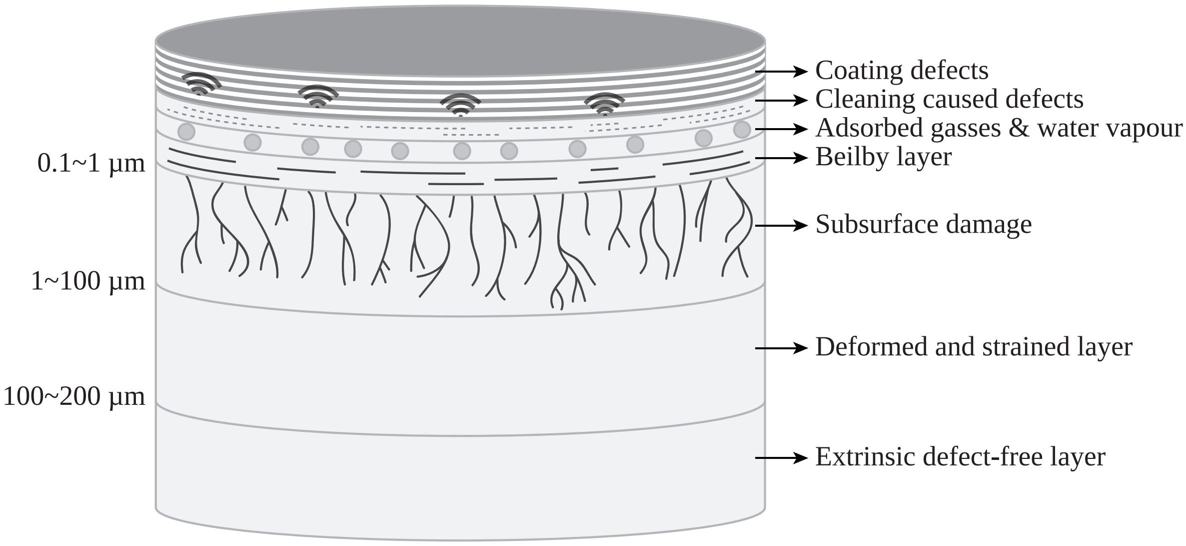

Figure 1.13 The schematic illustration of the extrinsic defect location in an optical glass substrate, which is polished, cleaned and with deposited thin films. The picture is adapted from [142].

the growth of SSDs – cracks, porous and other structures beyond the surface [28, 142]. SSD layer is known to be at 1–100 μm depth from the uncoated sample surface. After the optical element polishing, the surface is smoothed with a so-called Beilby layer [176]. It masks the remains of used abrasive substance (the so-called slurry residuals) and hides thousands of surface scratches and cracks. Beilby layer is located at 0.1–1 μm depth. Then, there is a layer containing adsorbed gasses or water vapours. It is formed due to surface interaction with the outer environment. Later defects created in cleaning and annealing processes are introduced into the layer system [177]. Moreover, when optical coatings are deposited on surfaces, the variety of damage initiators expands. Coating procedure might be influenced by previously created defects and can also cause generation of new ones. Herewith, we will discuss three main groups of the defects and the mechanism, which leads to the damage formation when extrinsic defects interact with intense laser radiation.

Subsurface defects

SSDs result from the mechanism of brittle material removal. These are micro cracks, scratches, voids, fractures, absorbing particles and other structures, which weaken the mechanical strength of the material [28]. The generation of subsurface defects is mostly related to the glass shaping processes, such as grinding, lapping and polishing [142]. In general, shaping defines a process by which the material is precisely removed from a workpiece (or specimen). Two surfaces are rubbed together with an abrasive between until the desired dimension, surface finish, or shape is reached. Shaping can be performed by hand movement or by a machine. Based on the smoothness of produced surface finish, shaping is divided into three steps: grinding, lapping, and polishing.

Grinding defines a rapid material removal from a sample. It is used to reduce the sample size and remove large irregularities from the surface. Grinding is performed with coarse, bonded abrasive particles ($>40\ \mu$m). The grinding wheel or plate typically rotates at a high speed around 200–1000 revolutions per minute (RPM). This process is associated with the growth of deepest sub-surface defects, especially cracks [142].

Lapping is used to produce a smooth, flat, unpolished surface, which features high tolerances (generally less than 2.5 μm uniformity). There are two lapping regimes: free abrasive lapping and fixed abrasive lapping. In the first case, an abrasive slurry is applied directly to a lapping plate. This is perhaps the most accurate method for producing specimens and causes the least amount of damage. In the case of fixed abrasive lapping, an abrasive particle is bonded to a substrate. Lapping is performed with mid-range abrasive particle (5–20 μm). The lapping plate rotates at a low speed (<80 RPM). This process helps to reduce deep subsurface damage but does not eliminate it completely [142].

Polishing intends to produce a scratch-free, specular surface using fine ($<3\ \mu$m) abrasive particles and very low speeds. There are many polishing techniques:

- **Conventional polishing.** Technical innovations over the past 20 years have made pad polishing the predominant conventional polishing method. Optical elements are polished using laps faced with polishing pads made of polyurethane or other more specified material. Such synthetic pads work well with particular polishing compounds that have been optimized for use with the pad. Laps faced with these polishing pads are extremely stable. Polishing plates can be manufactured relatively quickly. Mostly they are versatile and can be used for most polishing applications by adjusting the polishing process variable parameter.
- **Chemical-mechanical polishing (CMP).** This is a process where a sample surface is polished with a slurry containing an abrasive grit, namely cerium oxide, suspended within reactive chemical agents. The polishing action is partly mechanical and partly chemical. The mechanical element of the process applies downward pressure while the chemical reaction that takes place increases the material removal rate. The cerium oxide smooths out microscopic bumps and indentations on the glass surface. Consequently, particles of glass clump together with particles of polishing material in the used slurry, making it difficult to remove from the glass component. It is a complicated chemical-mechanical process during which a hydrated layer is given a rise to and deposited on the top surface. This is the so-called Beilby layer [176]. The Beilby layer is an amorphous or microcrystalline structure that conceals remaining scratches and confines leftover polishing material. This layer defines the optical resistance performance of conventionally polished optical elements.
- **Magnetorheological finishing (MRF).** It is a deterministic method that enable the production of complex optical elements with one-figure ac-

curacy <50 nm and possesses advantages over traditional polishing techniques in terms of subsurface damage [142, 178]. MRF performance is based on magnetorheological fluids (MR), which are generally composed of non-colloidal suspensions of 1–5 μm diameter magnetizable particles (such as iron) in carrier fluids (such as water or oil). The particles are magnetically polydomain. They possess no overall intrinsic magnetic moment but attain large magnetic moments when placed into a magnetic field, which leads to the alignment of the particles into long columns or chains. Due to this alignment, the viscosity of the fluid increases in the presence of a magnetic field. The stronger the field, the stiffer the fluid becomes. The increase in viscosity in the presence of a magnetic field is called magnetoviscous effect [179]. The ability of such a fluid to transmit force can be controlled by the strength of the applied magnetic field. A magnetic-field-stiffened ribbon of fluid is applied to polish out optical elements. The material removal is due to the great tangential effects as opposed to normal force in conventional polishing. Significant shear forces eliminating subsurface defects are created by the interaction among the wheel, MR fluid, and the specimen surface because the MR fluid ribbon flows through a converging gap between the lens and the wheel [143]. Consequently, it has been shown, that optical elements polished by MRF feature better optical resistance performance [180, 181].

- **Ion beam etching (IBE)**. The method is based on the optical surface exposure to an ion beam whereupon the material is removed by sputtering [182]. Optical performance with ion beam etching can be improved by a factor of two and increases with IBE depth. The final quality of the optical surface treated with ion beam depends on the applied ion beam voltage. As for fused silica glass, the depth of SSD is about 100 nm [182, 183].
- **Superpolishing**. Most super polishing techniques modify the conventional method by completely submerging the entire spindle/lap assembly

in a polishing fluid. This provides two main advantages. Firstly, the lap and workpiece is protected from the outside contaminants, which can scratch the optical surface. Secondly, submersion increases the thermal conductivity which causes the lap and substrate to be at virtually the same temperature. This results in improved shape consistency of the tool and workpiece, which is also a factor in achieving a smoother polished surface.

- **CO_2-laser polishing.** Surface of a sample is polished by exposing it to a carbon dioxide (CO_2) laser beam [184]. The surface is processed by scanning it with varying output laser power. It has been shown that CO_2-laser polishing strongly increases the damage resistance of a fused silica optic surface at the 355 nm wavelength. However, this method also introduces a level of stress and laser beam wavefront perturbations which continue to be the technology barriers for full deployment into optical element processing mainstream [185].

Absorbing particles

Absorbing particles are inclusions, slurry residuals or atomic clusters embedded within the polishing and deposition processes [28, 186–189]. Contaminants such as specks of dust or outgassed molecules, which settle on the optical surface from an outer environment or storage containers also act as absorbing particles [190]. There were several attempts to link the damage initiator properties such as nature, size distribution, and density to the observed laser damage statistics [186, 188]. When dealing with nanometric to micrometric defects, it is common to consider in a calculation the bulk material properties. For small particles the dielectric function depends on the particle size and differs from the bulk values because of the increasing importance of the surfaces compared to the volume, the change of the atomic structure, and the inhomogeneities of the electron density. Thus, the Mie theory has been used to evaluate the absorption of a defect [188]. Critical fluence has been shown to increase with decreasing particle size for different kind of defects (Fig. 1.14: A).

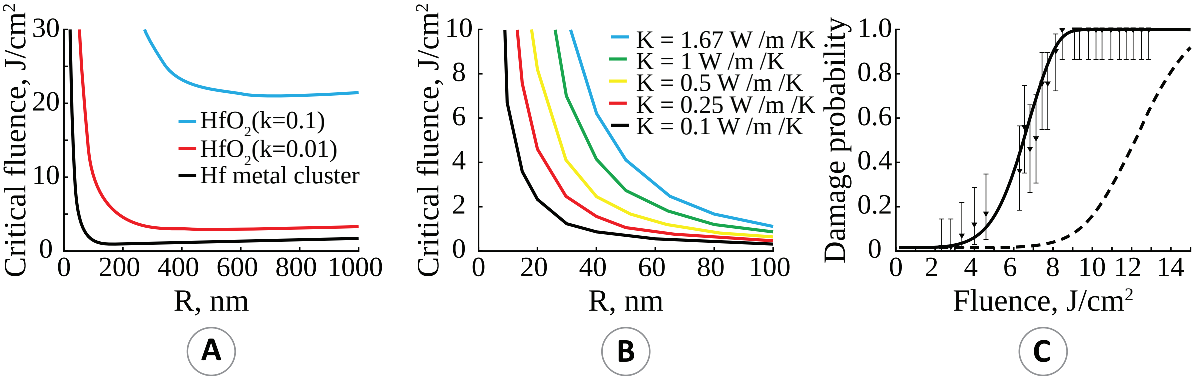

Figure 1.14 **A:** Critical fluence calculated for different inclusions (hafnium metal or off-stoichiometric absorbing HfO_2 defects) in hafnia matrix. **B:** Critical fluence calculated for a hafnium inclusion in hafnia matrix with different conductivities. **C:** The best fit of damage probability curves obtained by varying the thermal conductivity of the particles. Irradiation is at 1064 nm with a pulse duration of 12 ns at $1/e$ (Gaussian temporal shape). Data adapted from [188].

Such dependence can be used to identify both the type and the size of the LIDT limiting particles. Additionally, the influence of the thermal conductivity of the host material on the damage threshold was studied by plotting the critical fluence calculated for a hafnium inclusion in a hafnia matrix with different thermal conductivities (Fig. 1.14: B). A reasonably good agreement was reported by fitting laser damage statistics with varying thermal conductivity (Fig. 1.14: C, [188]). It has been shown that experimental results for various laser damage spot sizes and the dependences on material properties can be explained by the same kind of defects having a given density and size distribution. There are several models, which attempt to explain the experimental results related to the interaction of the laser beam and absorbing particles.

Thermal approach

Damage occurrence is explained via the existence of a threshold temperature. It is assumed that a material becomes damaged when the temperature of matrix material with absorbers reaches the critical temperature T_c, due to local absorption induced by a laser beam. A one-dimensional thermal diffusion model considers heat conduction as the dominating energy dissipation mechanism from the laser heated absorber [191]. According to this model, the thermal conductivity of absorber is much higher than the conductivity of the matrix and the temperature is homogeneous inside the absorber [192]. However, in order to fully understand and predict the forming of damage, the temperature dependence of thermal and optical properties, nonhomogeneous beam spatial profile and phase transformations of the heated material should be considered. Thus, finding an analytical solution becomes impossible and numerical techniques need to be developed. For the long pulse or continuous wave, thermal absorption is the dominant process. Temperature evolution, residual stress and strain, and melting morphology (if the laser intensity is high enough) can be estimated using heat conduction model. In the ultrahigh-power, short-pulse laser irradiation, firstly, thermal explosion indicates the generation of plasma fireball by ionization. Then the laser energy absorbed by plasma inside the material is released in different forms. Some energy drives the movement of crashed material (fireball growth model) [187], some is transported by the shock (impact cratering model).

Thermal Explosion and Fireball Growth Model

According to this theory, absorption is not confined to the nanoscale absorber but, upon temperature increase, spreads out to the surrounding matrix, thus proving the theory of thermal explosion and forming of a plasma "fireball" [187]. Generation and growth of the plasma "fireball" can be treated as the hydrodynamic motion of a highly heated and crashed material leading to the crater occurrence. The explosion is considered as instantaneous energy deposition, which initiates material motion. Forming of the crater can be defined in a simple hydrodynamic description, which agrees well with the experimental data and verifies the validity of the hypothesis of damage initiation by small absorbers [193, 194].

Impact Cratering Model

According to this model, plasma at the rear surface of components ejects into the material with certain initial kinetic energy and then the energy is redistributed between plasma and material. Under subsequent intense irradiation, a strong shock wave is launched in both plasma and material along their interface. The resulting pressure vastly exceeds the strength of material and the plasma penetrates the interface which leads to component deformation, material crash, and crater deformation [193, 194].

Cracks

Grinding of a glass can be described by brittle fractures caused by an ensemble of normally-loaded hard-indenters (abrasives) sliding and rolling across the surface of the glass workpiece. The brittle fracture will lead to both material removal and development of SSD. There are three basic types of fractures that can occur by static indentation [195, 196]: Hertzian cracks (Fig. 1.15: A), radial cracks (Fig. 1.15: B) and lateral cracks (Fig. 1.15: C). Based on their geometry, lateral cracks provide the largest material removal and also contribute significantly to the observed surface roughness. Hertzian and radial cracks contribute to deeper SSD and potentially to some material removal through the intersection with other cracks.

Cracks can be related to the macroscopic damage formation via three mechanisms: field intensification, energy absorption and mechanical weakness.

Field intensification. There are two approaches. First one considered crack as a thin slit with a width much smaller than the laser wavelength [28]. In this case, the field inside the crack is treated as electrostatic. However, calculations show, that based on this approach, maximum achieved field intensification is

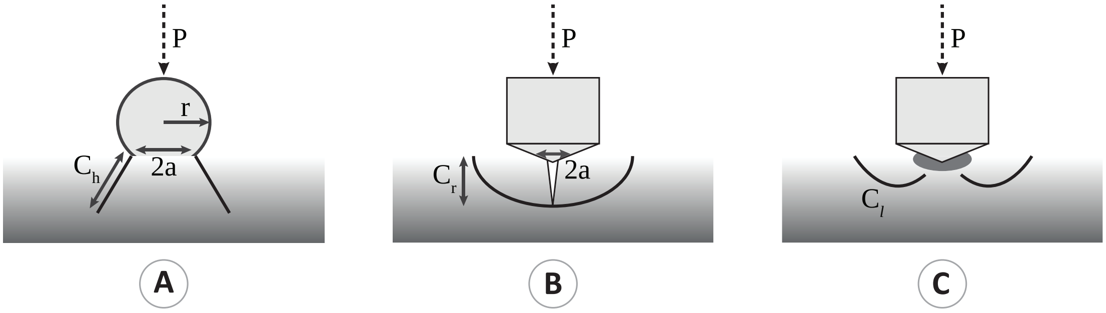

Figure 1.15 Schematic illustration of the fracture geometry of the idealized fractures created by static indentation. **A:** Hertzian cone crack from a blunt indenter. **B:** radial or median cracks from a sharp indenter. **C:** lateral crack from a sharp indenter [196]. P is normal load; r is radius of curvature for indent indenter; a is contact zone radius for a Hertzian indent; C_h, C_r, C_l are Hertzian, radial and lateral crack depths, respectively.

not sufficient to produce intrinsic damage [192]. Second approach suggests that a crack can reflect laser light. Reflected light then interferes with the main beam causing intensity hot-spots. Multiple reflections from cracks with the right orientation and from the rear surface are particularly effective since a total internal reflection can occur [197]. The numerical calculations have been employed in order to analyze the intensity distribution of an initially plane light wave incident on the planar and conical surface cracks [198]. The results show that the light intensity enhancements caused by the interference of internal reflections at the crack and the surface are very sensitive to the light polarization, the beam angle of incidence, and the crack geometry (e.g., crack width and orientation with the surface). The light intensity enhancement factor can locally reach 2 orders of magnitude for conical cracks of ideal shape. Furthermore, the electric field direction relative to the crack surfaces determines the light intensity profile around the crack. It has been shown that based on this knowledge, it is possible to quantitatively predict the magnitude of the LIDT drop on the surface [198].

Energy absorption in cracks. There are two factors that might increase absorption in the cracks. On the one hand, absorption can be increased by trapped nanoparticles from the polishing slurry. On the other hand, increased absorption might be caused by oxygen deficiency centers (ODC), which tend to form when an element is breaking. Oxygen deficiency results in a strong UV absorption so the clusters of ODCs can form a nano absorber [192].

Mechanical weakness. There are two types of material modification that occur under high-pressure [192]. One is a hoop stress around the explosion site fracture surrounding material. Brittle fracture is characterized by the fracture toughness. According to the Griffith [199] theory, fracture occurs when the stress at the crack tip is high enough that the energy expended in forming a new surface area is balanced by the energy gained in releasing a strain energy. Another type of deformation is the plastic one. A large damage spot must be surrounded by a fracture zone. Small sites correspond to smaller amounts of released energy. In this case, it is difficult to open cracks, and the damage site consists of only plastic deformation.

Coating defects

Most optical elements are coated to serve different purposes. Deposition of thin films adds another dimension of complexity by introducing new types of defects. Nodules are the most common type of defects detected in multilayer coatings [29, 51, 140, 200]. These are defects that grow from seeds or particulate into an inverted conical shape with a domed top protruding above the surface of the film (Fig. 1.16 A). For a few decades since 1990 nodules remain in a spotlight of various investigations. Multiple studies have been performed on nodule properties [29, 51, 140, 200–203], growth mechanism [51, 204–208] and interaction with applied laser radiation [141, 153, 203, 209–212]. They act as focusing lenses or induce complex interference patterns due to multiple reflections caused by conical defect geometry [141, 153, 202]. Light intensification by nodular defects has been shown to be sensitive to various nodular characteristics (size, geometry, depth, etc.) as well as laser irradiation conditions

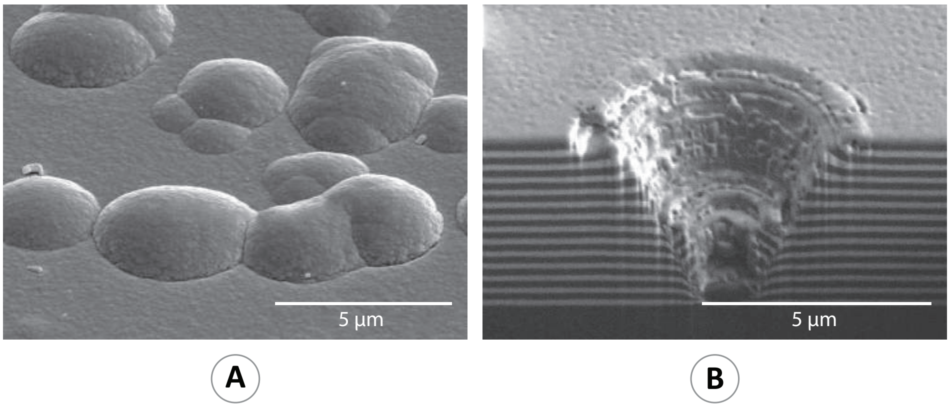

Figure 1.16 Typical images of a nodule visible on the sample surface by optical microscopy (**A**) [214] and focusing ion beam technology (**B**) [141].

(wavelength, polarization, angle of incidence, etc.) [141, 153, 203, 209–212]. Mostly, light interaction with nodular defects is investigated in terms of enhancement of squared electric field $|E|^2$ by employing numerical simulations. Up to now most of the parametric studies were carried out for the infrared (IR) spectral range. There still is a lack of studies analyzing the significance of the nodule defects in multilayer coatings designed for ultraviolet (UV) applications [213].

Coatings can also contain absorbing defects. For instance, metallic clusters with higher absorption than surrounding matrix are known to form within a coating due to the incomplete partial pressure of oxidation during the deposition process [215]. Absorbing defects can also originate from the contamination of the deposition chamber. Evaporated contaminants might be embedded within the deposited layers as atomic impurities [189]. Furthermore, the properties of the existing defects can change after covering them with dielectric layers [187].

2 Advancing the optical resistance metrology

"Perfection is not attainable, but if we chase perfection we can catch excellence."
Vincent Thomas "Vince" Lombardi, an American football player, coach, and executive

Material related to this chapter is published in *A3, A6, A7, A8, A16, C3–C7*

This work has been awarded with "The Best Poster Presentation Award" at SPIE Laser Damage 2012 conference in Boulder Colorado, USA

In the development of high-power laser systems, it is crucial to understand thoroughly the physics of optical resistance of optical materials. Assessing accurately LIDT is of equal importance. Main principle of LIDT testing is the damage frequency method (DFM) [9]. It is a statistical procedure witch relates damage probability with incident laser peak fluence. Despite international acceptance, day by day use of the DFM method encounters many practical problems. International round-robin measurements [37–39, 39, 40] and Monte-Carlo based modelling of LIDT testing [48] have shown that the LIDT values estimated by DFM are widely scattered. Poor accuracy and repeatability of DFM raise a major concern among optical equipment developers and users, since reported LIDT values from different institutions can't be compared unambiguously. It also impedes the understanding of physics of laser-induced damage phenomena and its causes. These issues have been approached in several studies [216, 217]. However, a uniform solution has not yet been found. This inspired the detailed investigation of LIDT testing procedure carried out in this thesis. It includes a detailed inspection of the metrology process and identification of the sources causing the poor DFM performance. Collected knowledge leads to the revision procedure of LIDT testing, introduced at the end of this

Chapter. It is based on maximum-likelihood principle. Monte Carlo-based numerical simulations and real world experiments are used to test the properties of the novel corrections applied to DFM use. The primary findings show that the LIDT results obtained using the revised DFM are highly reliable and repeatable.

2.1 Introduction into metrology

The study starts with a brief overview of the measurement characterization according to the International Committee for Weights and Measures (abbreviated CIPM from the French **C**omité **I**nternational des **P**oids et **M**esures). It is based on two international standards: Guide to the Expression of Uncertainty in Measurement (GUM) [218] and International Vocabulary of Metrology (VIM) [219].

Measurement defines the process of experimental information gathering about the magnitude of a quantity. The quantity that is intended to be measured is called a measurand [219]. Any experiment is influenced and ultimately limited by many factors, such as sampling, instrument drifts and calibration, the accuracy of measuring devices, human factors, environmental effects, approximation models etc. Thus, there is no such thing as an ideal measurement. The result of a measurement is only an estimate of the true measurand value. Since there is no perfect measurement, the true measurand value is never known. Two hypotheses have been made about the true measurand value. The first assumption suggests that the true measurand value is single and invariant, thus stating that the existence of a true measurand value is accepted as an axiom. This is the so-called "**Error approach**", also known as "**Traditional approach**" or "**True value approach**" (Fig. 2.1: A) [218]. In this case, the difference between the measured value (estimate) and the 'true value'

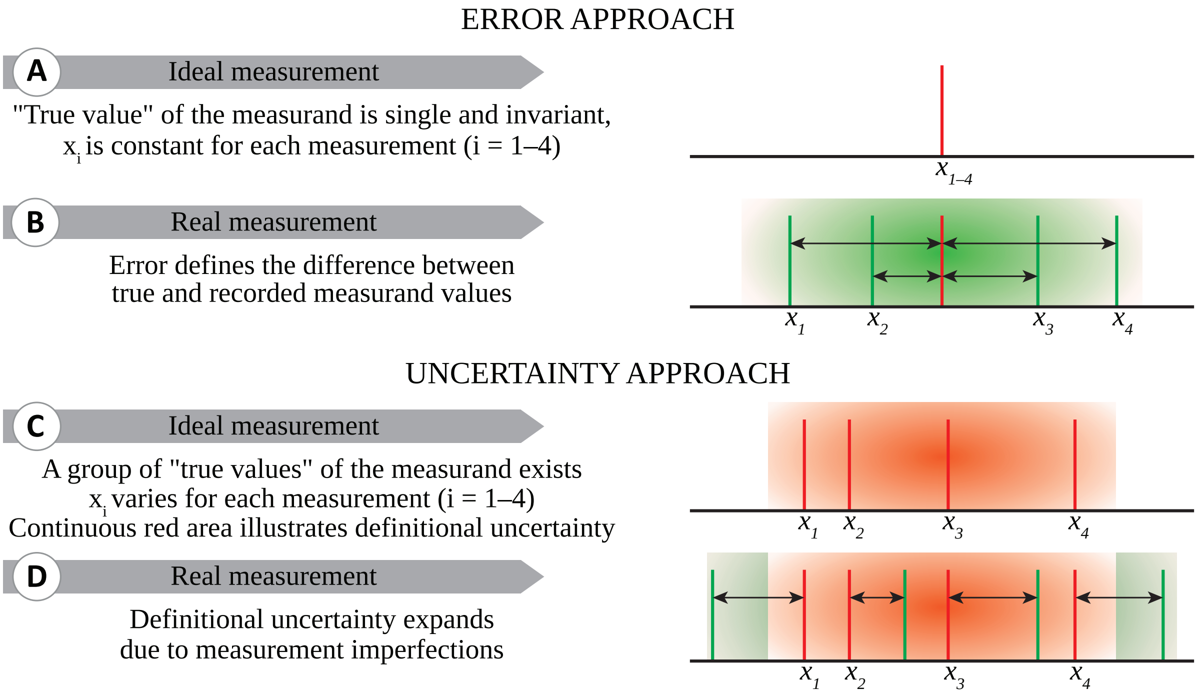

Figure 2.1 The basics of error approach (**A, B**) and uncertainty approach (**C, D**). Red and green bars correspond to measurand and measured values of single trial. Red and green gradient areas illustrate definitional and measurements uncertainty intervals, respectively.

of the quantity being measured is defined by the absolute error:

$$\text{error} = \text{estimate} - \text{‘true value’}\,. \tag{2.1}$$

Therefore, the measurement result is complete only when accompanied by a quantitative statement of its error,

$$\text{measurement result} = \text{best estimate} \pm \text{error}\,. \tag{2.2}$$

The aim of this approach is to characterize the error as the largest deviation from the true measurand value (Fig. 2.1: B). In this case, the error is understood as a standard error meaning ±2 standard deviations. It is also assumed that it follows the normal distribution and is symmetric. The main disadvantage of this technique is that the physical quantities intended to be measured often are not invariants. Their properties might change due to environment conditions (such as temperature, pressure, humidity etc.) or time. Also, the full information about the measurand is never known. As an example, suppose that the measurand is the thickness of a given sheet of metal. It is a well-known fact that metals expand with heat, thus the thickness measurements should be performed at a specific temperature. However, there are many other factors, that might conceivably affect the thickness, such as the barometric pressure, the altitude of the sheet in the gravitational field, the way it is supported, etc. So, if the measurement is not performed within an idealized environment, there always are doubts about the recorded results. The absolute measurand value can also change with time. For example: measuring the volume of evaporating liquid in a closed system. Even if the environment conditions remain constant, the true value of the measurand will change each time measurement is performed due to evaporation and condensation processes. In general, every measurand has such an "intrinsic" uncertainty at some level. Thus, the concept of the single true value has become obsolete. As a solution, an alternative definition of the true measurand value has been proposed. In this case, the true measurand value is defined not as a single invariant but rather as a continuous distribution of "true values" that can be reasonably attributed to the measurand. This is the so-called "**Uncertainty approach**" [218, 219]. Uncertainty resulting from the inherently finite amount of detail in the definition of a measurand is called definitional uncertainty (Fig. 2.1: C). The imperfection of the measurement expands this uncertainty. In this case, the measurement result is a combination of the best estimate and full measurement uncertainty:

$$\text{measurement result} = \text{best estimate} \pm \text{uncertainty}\,. \tag{2.3}$$

The uncertainty of measurement is a parameter that characterizes the dispersion of the quantity values that are being attributed to a measurand, based on the information used. Definitional uncertainty is included in every measurement uncertainty (Fig. 2.1: D). The "Uncertainty approach" is now validated by CIPM and VIM. Thus, it is also applied for measurement characterization in this study. However, "Error approach" has been used for a long time in scientific researches. Thus, in order to avoid confusion in terminology when comparing the measurement characterization techniques before and after internationally accepted transition, the difference of the core concept of both approaches should be well understood.

Uncertainty evaluations start with identification of uncertainty sources. As discussed above, there are many factors that might influence the final measurement result. Though, it is impractical and not necessary to consider all of them. The most significant contributions to the full measurement uncertainty should be recognized by the operator. Within the scope of this study, two sources of uncertainty are considered:

- **Experimental uncertainty**. It can be both random and systematic. Random experimental uncertainty can be noticed by repeating a measurement for many times using exactly the same settings for all inputs/variables. Systematic experimental uncertainty is related to the measuring instruments. Results obtained by the instruments can deviate from the true value due to bias, changes caused by aging effect, wear, or other kinds of drift. Also, poor readability, noise (for electrical instruments) and many other problems.
- **Model uncertainty**. This uncertainty is introduced due to simplifications of reality. The model used to measure and evaluate an item might be incomplete, inaccurate or not representative.

All uncertainties are grouped into two categories according to the method used to estimate their numerical values [218, 219]:

- ***A* type uncertainties** – these are uncertainties, which are evaluated by statistical analysis of a series of observations. In this case, uncertainties are estimated on the basis of repeated measurements, usually assuming the normal distribution for the variability in the mean of the values.
- ***B* type uncertainties** – these are uncertainties, which are evaluated from any other information, such as knowledge from the past experience of the measurements, from calibration certificates, manufacturer specifications, etc. In this case, uncertainties are obtained by assuming a particular probability distribution, such as normal, a rectangular, a triangular or other distribution.

Such categorization seems to be familiar with classification of random and systematic errors. Though, there is no equivalency. Type *B* might be used to evaluate random uncertainty as well as type *A* can be used to characterize systematic uncertainty. In this study, analysis of each variable recorded in order to determine the LIDT is performed by employing Monte Carlo-based simulations. It means that distribution of each tested variable can be obtained and corresponding uncertainties can be determined directly from these distributions. Thus, further review is focused only on the Type A uncertainty evaluation.

Type *A* uncertainty of a random variable is obtained from a probability density function (PDF), which is derived from an observed frequency distribution of the measurand. PDF describes the relative likelihood (probability) for continuous random variable falling within a particular range of values (Fig. 2.2). Probability that a continuous random variable X is in the range $[a, b]$ is defined by the integral of density of this variable over the range $[a, b]$:

$$P(a \leq X \leq b) = \int_a^b f(x)\,\mathrm{d}x\,, \tag{2.4}$$

where, a and b are real numbers, $f(x)$ is probability density function, which satisfies two properties. Firstly, $f(x) \geq 0$. Secondly, $\int_{-\infty}^{+\infty} f(x)\,\mathrm{d}x = 1$.

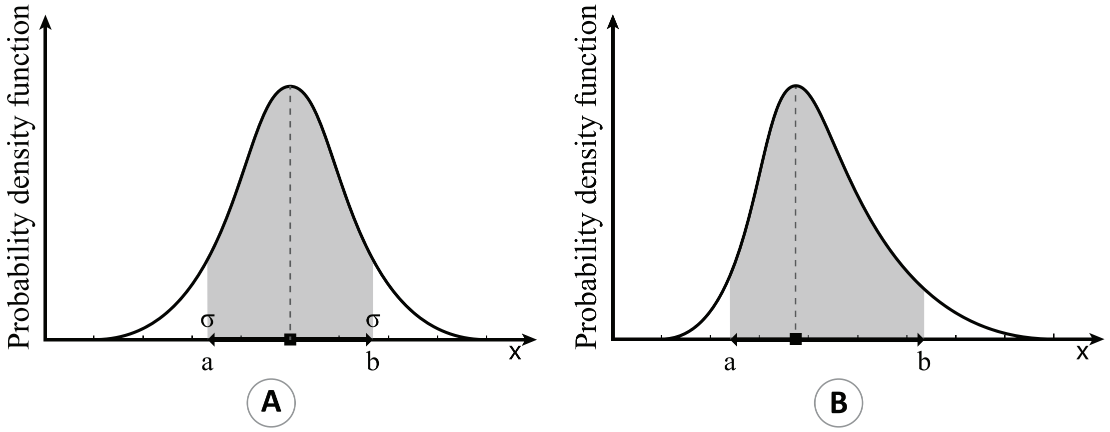

Figure 2.2 An example of PDFs. **A:** symmetric. **B:** asymmetric. σ is standard deviation of a measurement. Coverage interval is defined by the interval $[a, b]$.

If a random variable features unimodal and symmetric PDF (for instance, Gaussian), the uncertainty components are quantified by variances σ^2 or standard deviations σ. For convenience, the measurement uncertainty expressed as a standard deviation is often called Type A standard uncertainty u. In the case of Gaussian distribution, interval covered by $\pm\sigma$ corresponds to 68% of the PDF plot (Fig. 2.2: A). It means that the reported value lies within the stated uncertainty interval with a 68% probability. In practice, there is a need to ensure measured results with a higher confidence. Thus, the standard uncertainty is expanded. According to GUM [218], the expanded uncertainty U is defined as a quantity defining an interval about the result of a measurement that may be expected to encompass a large fraction of the distribution of values that could reasonably be attributed to the measurand. Thus, the expanded uncertainty is also referred to as a coverage probability and the defined fraction of the distribution is referred to as a coverage interval. In the case of normal distribution, the expanded uncertainty U can be calculated by multiplying the standard uncertainty u by a coverage factor k. Typically the coverage factor is in the range of 2 to 3. For instance, for variables featuring a Gaussian PDF, the measurement result is usually reported with 95% coverage probability, which corresponds to the coverage interval defined by $\pm 2u$ that equals to $\pm 2\sigma$. If PDF of the random distribution is bimodal or asymmetric, the uncertainty intervals are no longer symmetric and cannot be defined by a standard deviation σ or variance σ^2. Then a measure of uncertainty is the coverage interval [218]. If PDF of the tested variable is asymmetric but unimodal (single-peaked) (Fig. 2.2: B), then its uncertainty can be defined as a coverage interval for a quantity with a shortest length among all the coverage intervals for that quantity having the same coverage probability [218]. Coverage interval is determined numerically. Generally there is more than one coverage interval for a stated probability. For instance, if PDF or the variable is bimodal or multimodal. Within the scope of this thesis, two types of PDF will be addressed: unimodal symmetric (namely, Gaussian) and unimodal asymmetric.

Nowadays most measurements are complex. Usually, the reported result is the outcome of several directly measured variables, which feature linear or nonlinear relationship. Furthermore, it is important to note that each measuring device has its own response function. Any measured distribution of the quantity is indeed a convolution between the real distribution and the instrument response function (IRF). Thus, uncertainty propagation during the measurement should be considered. There are different ways to demonstrate such propagation. The most known is the GUM uncertainty framework [218]. It is based on the application of the law of propagation of uncertainty and the characterization of the output quantity by a Gaussian distribution or a scaled and shifted t-distribution in order to provide a coverage interval. Another way is to employ the Monte Carlo method. In this case, the propagation of distributions are evaluated by performing a random sampling from probability distributions. Illustration of the propagation of distributions of two input quantities featuring asymmetric PDF are shown in Fig. 2.3.

Although the metrology guides such as VIM and GUM provide a framework for assessing uncertainty, they also state that the provided tools cannot be a substitute for critical thinking, intellectual honesty, and professional skill. The

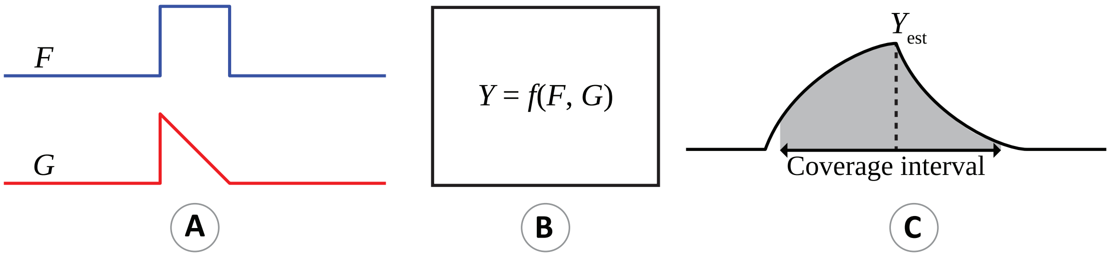

Figure 2.3 The basics of convolution procedure. **A:** F and G are PDFs of the input quantities. **B:** model function of the output quantity Y. **C:** evaluation of the best Y estimate and coverage interval.

evaluation of uncertainty is neither a routine task nor a purely mathematical one. It depends on detailed knowledge of the nature of the measurand and of the measurement. The quality and utility of the uncertainty quoted for the result of a measurement therefore ultimately depend on the understanding, critical analysis, and integrity of those who contribute to the assignment of its value. Thus, analysis presented within this study is based but not limited to the herewith described uncertainty evaluation recommendations.

2.2 LIDT metrology

LIDT test procedure is destructive: an intense laser radiation is applied on a sample surface, which is monitored for damage occurrence. There are several ways to relate damage event with threshold fluence when damage occurs. They all fall into three categories based on the method used for the LIDT determination.

Physical approach. One way to determine the critical fluence when a material becomes damaged is to inspect the LID morphology. Ablation threshold can be estimated either from the fluence-dependent crater diameter [220], crater depth [221] or ablated volume [222] relations. This approach is commonly used in the micro-machining community (mostly in the nontransparent spectral region), while, in this case, the ablation threshold is often treated as a criterion for the LIDT. However, the laser damage may also appear as a colourized region or a fracture without any material removal, thus the LIDT estimation from the ablation crater dependence on peak fluence is not always applicable.

Statistical approach. This is the most common approach used for the LIDT determination. Often this technique is also referred to as the damage probability method or the so-called statistical damage frequency method (DFM). Due to its wide application, the DFM was taken as a basis for international standard ISO 21254 1-4 [9, 223, 224]. It is the main document, which defines the LIDT measurement technique and evaluation procedure. Consequently, it is also the main LIDT testing technique analyzed within this thesis. Applying this approach, the LIDT is measured by interpreting the damage probability statistics obtained from a sequence of fresh sites exposed to well characterized, separated in time and space, laser pulses on the optical surface. There are several statistical LIDT determination methods, which differ in sample exposure algorithms [217, 225, 226] and data interpretation methods [35, 36, 216]. Detailed description of the used DFM is provided in the **Subsection 2.2.2**.

Raster scan approach. Within the last decades, one more approach has been added in the ISO 21254 standard as an alternative LIDT test procedure. This is the so-called raster scan procedure. The sample surface is raster scanned for defects using varying peak fluences. The damage density is estimated from optical microscopy pictures obtained after the sample exposure. Then the damage density is plotted as a function of applied peak fluence used to raster scan particular area. In this case, the LIDT is defined by fitting the recorded dependence. Raster scan approach is particularly useful when dealing with large optical elements and very low defect density. It shows promising results in terms of LIDT characterization based on the damage density determined for applied laser fluences [186, 227–229]. Raster scan procedure will be analyzed in detail in **Chapter 3**.

2.2.1 Probabilistic nature of laser damage

Damage occurrence is a probabilistic event. Probabilistic damage nature is caused by three conditions (Fig. 2.4). Firstly, nanosecond LIDT is mostly limited by nanometer-sized defects inherent to the optical element manufacturing processes [28, 41, 42]. Defects are randomly distributed both on the sample's surface and in the bulk. When the sample surface is irradiated with a laser beam, there is a random chance to expose a defect in the laser beam affected area (Fig. 2.4: A).

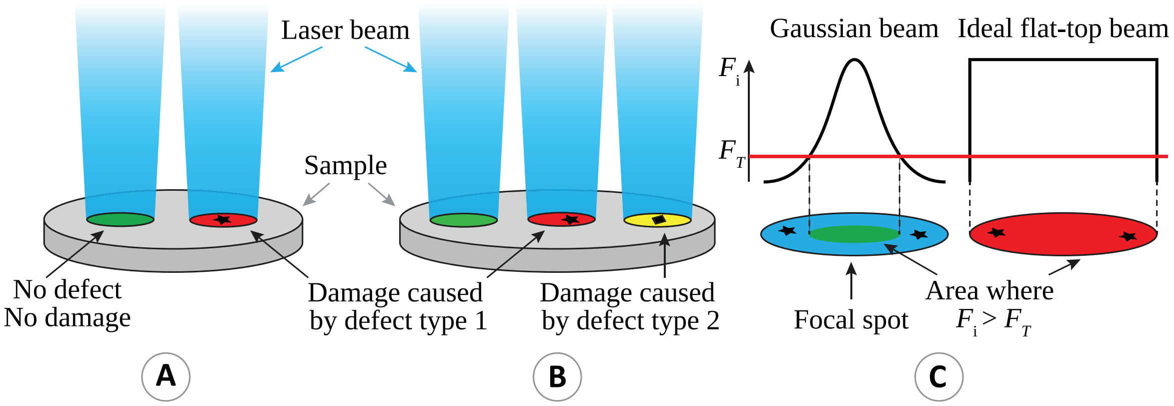

Figure 2.4 The visualization of three conditions causing a probabilistic damage nature. **A:** random defect distribution. **B:** random threshold fluence distribution. **C:** fluence distribution when the testing with Gaussian beams is compared with the fluence distribution when testing with top-hat or ideal flat-topped beams over the focal spot. F_i is applied fluence, F_{T} is threshold fluence.

Secondly, the critical fluence, necessary to cause damage, might vary for different defects. For instance, the damage might be caused by different defect types, such as absorbing inclusions, and scratches, featuring different constant threshold fluence (Fig. 2.4: B). In this case, the damage occurrence and critical fluence depend on two random conditions: whether a defect is exposed and which defect is randomly exposed.

Finally, probabilistic damage nature is always observed if testing is performed with a Gaussian-like spatial beam profile. Usually, the spatial beam profile is characterized for a peak laser fluence, which is defined as

$$F_{\mathrm{p}} = \frac{E}{S}\,, \tag{2.5}$$

where F_{p} is peak fluence [J/cm^2], E is laser pulse energy [J], S is effective focal spot area [cm^2]. In the case of top-hat or ideal flat-topped focal spot, the fluence distribution within the entire exposed area would be the same. Though, for Gaussian-like beams, the fluence distribution within the whole laser beam affected area differs (Fig. 2.4: C). Here we discuss a statistical phenomenological model that relates the laser damage probability distribution, surface defects and the applied laser radiation, which features Gaussian-like spatial beam profile and is characterized for a peak laser fluence.

2.2.2 Damage probability model

Damage probability model is constructed from three parts. The first part deals with the characterization of critical (threshold) fluences needed for randomly distributed defects to cause damage. For this purpose, the so-called defect ensembles are introduced. The second part describes the exposure of a defect to a Gaussian-like spatial profile beam. The relationship between applied local fluence and threshold fluence of a defect is discussed. The third part discusses the probability to "hit" the defect on a sample surface. Sample exposure to laser radiation is considered as a binomial event with two possible outcomes: damage either occurs or not.

Defect ensemble is a mathematical model used to characterize the actual distribution of defects within the optical elements via their threshold fluences. It is defined as

> *"distribution of the local defect damage threshold in respect to their density at the surface of interest"* [9]

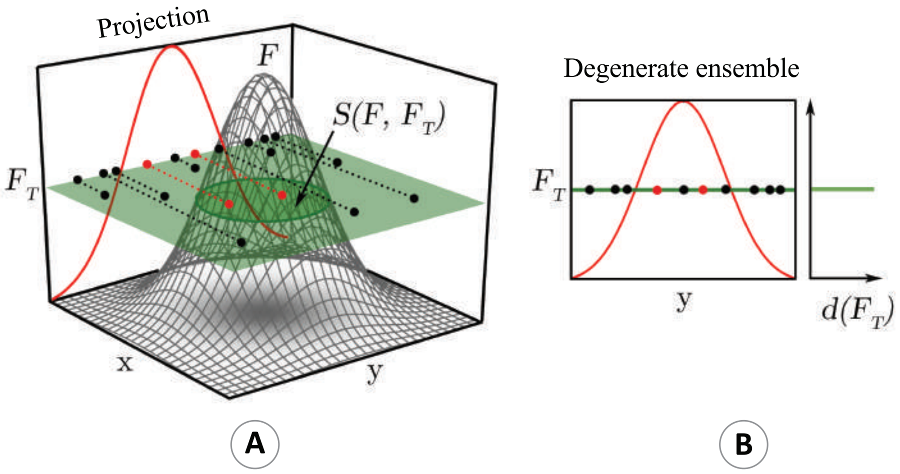

Figure 2.5 **A:** irradiation of the surface of a sample, covered by randomly distributed defects with defined damage threshold level, by laser beam having Gaussian intensity profile. **B:** degenerate defect ensemble function.

The true defect ensemble is never known prior to the LIDT measurement. It only can be assumed. More attention to distinct defect ensembles will be dedicated in the **Chapter 3**. In order to exemplify the reproducibility issues in the LIDT test procedure, here only the simplest defect ensemble – the degenerate one – will be used [43].

The degenerate defect ensemble is based on the assumption that all defects located on the sample surface are identical and have a constant damage threshold, F_{T}. Mathematically such a situation can be defined by a Dirac delta function (Fig. 2.5: B):

$$d(F_{\mathrm{T}}) = M\delta(F_i - F_{\mathrm{T}})\,, \tag{2.6}$$

where F_{T} corresponds to the threshold fluence and F_i is applied fluence. M defines the average defect density on the unit surface area.

At first, the parametrization of LIDT limiting defects via degenerate defect ensemble was suggested by S. R. Foltyn [43]. Further, this approach was developed by J. O. Porteus et al. [44] and R. M. O'Connell [46]. It was suggested that defect ensembles are more complicated than assumed within the degenerate case. Over the time, different hypotheses were made about possible defect ensembles and their critical fluence threshold distribution $d(F_\mathrm{T})$: Gaussian law [47], power law [44, 46, 230], or their combinations [45, 48, 49] were investigated. Comparison of these defect ensembles will be discussed in detail in **Chapter 3**.

As an example, let us consider a single isolated defect exposed to the laser radiation. The defect triggers a damage if the local fluence F_i is exceeding F_T (Fig. 2.5: A). In the case of Gaussian laser pulses the local fluence $F_i(r)$ is expressed as

$$F_i(r) = F_\mathrm{p} \exp\left[-2(r/w)^2\right] , \tag{2.7}$$

where F_p is the peak fluence (energy density), r is radial coordinate and w is Gaussian beam radius at 1/e^2 level of F_p.

The significant area a, when the local fluence exceeds the threshold fluence F_T, is limited by a circle, the size of which varies when the peak fluence F_p changes:

$$a(F_\mathrm{p}, w, F_\mathrm{T}) = 0.5 \cdot S \cdot \ln(F_\mathrm{p}/F_\mathrm{T}) , \tag{2.8}$$

where $S = \pi w^2$ is the focal laser spot area size defined at 1/e^2 level with respect to peak fluence.

In practice, there is more than one defect in the area a. The average amount of the damage causing defects found within the irradiated zone is equal to $\lambda_\mathrm{d} = a \cdot M$. As the peak fluence F_p increases, the area a and the average number of "laser activated" defects λ are also increasing. The probability $P(F_{\mathrm{p}i})$ to irradiate a defect with sufficient fluence within the area a during a single shot laser exposure is derived from Poisson statistics [231]:

$$Pr(d) = \frac{(\lambda_\mathrm{d})^d}{d!} \cdot \exp(-\lambda_d) , \tag{2.9}$$

where $Pr(d)$ is the probability to hit exactly d number of defects inside area a when the average amount of d (defined from many such experiments) is λ_d.

When optical elements are exposed to laser radiation, one of the two outcomes is possible: irradiated area becomes damaged or stays non-damaged:

$$P(D) + P(ND) = 1 \,. \tag{2.10}$$

In other words, the probability to either damage (D) or not to damage (ND) the sample after irradiation is always a necessary event. The $P(ND)$ can be found from the expression 2.9 when the number of defects is equal to zero. Then, it is obvious that the probability of damaging at least one defect within an irradiated area can be expressed as

$$P(D) = 1 - P(ND) = 1 - Pr(0) = 1 - \exp(-\lambda_{\mathrm{d}}) \,. \tag{2.11}$$

If we take into account the dependence of area a on $F_{\mathrm{p}i}$ (Eq. 2.8), we can derive the probability of damage that is expected to be found experimentally under ideal irradiation conditions (Fig. 2.5: 4):

$$P(F_{\mathrm{p}}) = \begin{cases} 0 & \text{if } F_{\mathrm{p}} < F_{\mathrm{T}} \,, \\ 1 - \exp\left[-M(S/2) \ln F_{\mathrm{p}}/F_{\mathrm{T}}\right] & \text{if } F_{\mathrm{p}} \geq F_{\mathrm{T}} \,. \end{cases} \tag{2.12}$$

2.2.3 Experimental set-up

The automated in-house built LIDT test bench (Fig. 2.6) was developed at the Vilnius University Laser Research Center. It is based on a single longitudinal mode, injection seeded, Q-switched Nd:YAG laser delivering linearly polarized pulses with full-width half-maximum (FWHM) of 8 ns at 1064 nm wavelength. Since the object of this thesis is LIDT under UV radiation, the laser source is equipped with two nonlinear crystals, which are able to generate pulses of 4.8 ns (FWHM) at 355 nm wavelength. Fluence is adjusted with a motorized attenuator, consisting of a half-wave plate and a polarizer. Laser pulse energy is monitored by a calibrated photodiode. Spatial beam profile is characterized before the measurement by a charge coupled device (CCD camera) with 10× magnification optical equipment. The lateral pixel resolution of the CCD camera is 3.75 μm. A mechanical shutter is employed in order to pick up separate shots from a pulse train with 50 Hz repetition frequency.

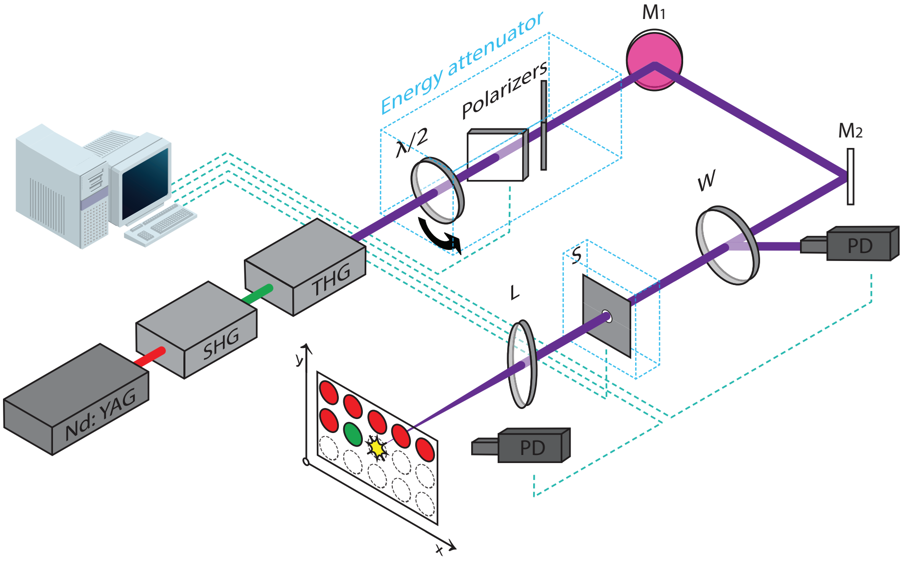

Figure 2.6 The schematics of an experimental LIDT test bench. SHG is unit for second harmonic generation, THG is unit for third harmonic generation, $\lambda/2$ is a half-wave plate, M1, M2 are steering mirrors, W a wedge, PD a photodiode, S a mechanical shutter.

In the measurements designed to investigate the LIDT testing metrology presented in this chapter, the beam size of 34.6±1.6 μm (taken at $1/\mathrm{e}^2$ level of peak fluence) was set by using plano-convex lens of 30 cm focal distance. Small beam diameter is used due to limited sample surface in order to ensure high-resolution statistical measurements and to collect sufficient statistical data. Sample exposure and the testing algorithm will be explained in detail in the following Subsection 2.2.4. The online damage detection system was based on monitoring the backscattered light. Whenever the damage occurs, the signal of backscatter light changes: it increases or decreases. A photodiode sensor was used to track the laser radiation induced surface changes. The off-line inspection of irradiated sites was performed by Nomarski microscopy after irradiation exposure. For the criterion of damage, we consider any visible modifications that can be seen by Nomarski microscope as recommended in ISO-21254 standard [9].

2.2.4 1-on-1 test procedure

In a typical damage probability experiment, the surface of a sample is virtually divided into a matrix of individual sites. Each site is exposed to a separate and well spatially and temporally characterized laser pulse (Fig. 2.7). After irradiation, each site is observed by Nomarski microscope in order to inspect for the possible visual changes (damage) of the surface. Its status is recorded as damaged (red sites in Fig. 2.7) or non-damaged (green sites in Fig. 2.7). A constant number of sites is irradiated by single laser pulses at a constant laser fluence. The probability of damage is then calculated as the ratio of damaged k_i and total irradiated n_i sites, for each ith individual fluence level, $F_{\mathrm{p}i}$:

$$P_i = \frac{k_i}{n_i}\,. \tag{2.13}$$

The same procedure is repeated at different fluence levels in order to collect sufficient statistics of damaged and non-damaged sites. Following this algorithm, the whole optical element surface is exposed. The obtained probabilities of damage are then plotted as a function of averaged maximal fluence. Typical damage probability curve is shown in Fig. 2.7 on the right. A measurement result is only complete if it is accompanied by a statement of the uncertainty in the measurement. Thus, for each measured point, fluence (Fig. 2.7: horizontal axis) and damage probability (Fig. 2.7: vertical axis) uncertainty interval should be established. Uncertainty intervals can be estimated from probability distributions of the measured variables. Several assumptions are made about possible probability distributions of fluence and damage probabil-

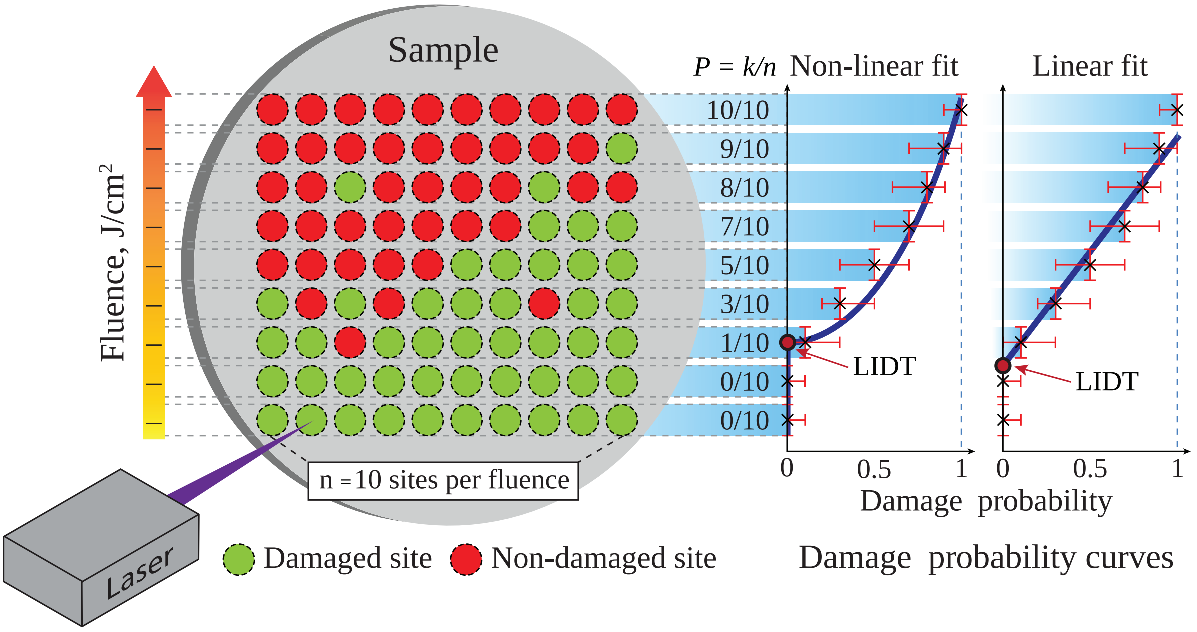

Figure 2.7 The basics of 1-on-1 LIDT test procedure. On the **left** there is a sample: each site of the matrix which is exposed to a single shot laser radiation corresponding to particular peak fluence. On the **right** there are damage probabilities that are extrapolated by either linear or nonlinear models to determine the LIDT value.

ity. The standard approach will be discussed in detail in the following Subsection 2.2.5. The alternatives will be addressed within ongoing analysis carried out in this Chapter. The damage threshold is estimated by fitting damage probability statistics versus applied fluence relation by appropriate extrapolation model: either linear [9, 216] (Fig. 2.7: linear fit) or nonlinear (Fig. 2.7: nonlinear fit) [232].

2.2.5 LIDT evaluation by least squares fitting

According to the ISO 21254-2 standard, the LIDT is determined by linear regression [9]. The damage probability data are extrapolated to zero damage probability (Fig. 2.8) [9]. The slope m, and intercept b of the linear fit is calculated by the least squares estimation (LSE) [233]. It is a mathematical procedure created to find the best-fitting curve to a given set of points by minimizing the sum of the squares of the offsets (also referred as "the residuals") of the points from the curve.

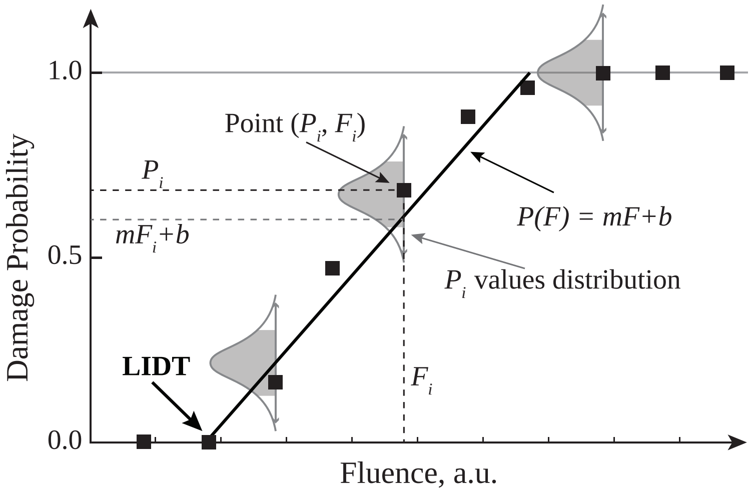

Figure 2.8 The LIDT determination from damage probability curve fitted by the least squares method. The gray area within the plotted normal distributions of dependent variable (fluence) corresponds to ± standard deviation σ. For simplicity, PDFs are visualized only for several points.

If these conditions are satisfied, then parameters *m* and *b* can be evaluated as follows:

$$m = \frac{1}{\Delta}\left\{\sum_{i=1} \frac{1}{\sigma_i^2}\right\}\left\{\sum_{i=1} \frac{P_i F_i}{\sigma_i^2}\right\} - \left\{\sum_{i=1} \frac{F_i}{\sigma_i^2}\right\}\left\{\sum_{i=1} \frac{P_i}{\sigma_i^2}\right\}, \tag{2.14}$$

$$b = \frac{1}{\Delta}\left\{\sum_{i=1} \frac{F_i^2}{\sigma_i^2}\right\}\left\{\sum_{i=1} \frac{P_i}{\sigma_i^2}\right\} - \left\{\sum_{i=1} \frac{F_i}{\sigma_i^2}\right\}\left\{\sum_{i=1} \frac{P_i F_i}{\sigma_i^2}\right\}, \tag{2.15}$$

$$\Delta = \left\{ \sum_{i=1} \frac{1}{\sigma_i^2} \right\} \left\{ \sum_{i=1} \frac{F_i^2}{\sigma_i^2} \right\} - \left\{ \sum_{i=1} \frac{F_i}{\sigma_i^2} \right\}^2 . \tag{2.16}$$

Then, the damage threshold is determined by the expression

$$F_{\mathrm{T}} = -\frac{b}{m} . \tag{2.17}$$

Since the least squares (LS) method is not restricted to ensure positive values of the F_{T}, an additional condition was added to the ISO 21254 standard. The calculated threshold fluence should be both positive and less than or equal to the lowest observed fluence causing damage. If the F_{T} value is not positive, the reported threshold should be given as the lowest observed energy density causing damage.

According to the ISO 21254–2 standard, the uncertainty of the measured LIDT value is determined by the classical error approach [9]. In order to evaluate the uncertainty of the estimated LIDT result, three factors should be considered: fluence uncertainty interval (horizontal bars), the uncertainty of the damage probability (vertical bars) and fitting uncertainty. Both the fluence and the damage probability uncertainty are referred to as measurement uncertainty and estimated by equation

$$\sigma_i = \begin{cases} \sqrt{\frac{n_i - k_i}{k_i \cdot n_i} + \varepsilon_{\mathrm{F}}^2} & \text{when } k_i > 0 , \\ \sqrt{\varepsilon_{\mathrm{F}}^2} & \text{when } k_i = 0 , \end{cases} \tag{2.18}$$

where ε_{F} is fractional uncertainty in the measured laser peak fluence. The uncertainty in the threshold is determined using

$$\sigma_T^2 = \sigma_m^2 \left\{ \frac{\partial F_{\mathrm{T}}}{\partial m} \right\}^2 + \sigma_b^2 \left\{ \frac{\partial F_{\mathrm{T}}}{\partial b} . \right\}^2 \tag{2.19}$$

The equation can be simplified to

$$\sigma_T = \frac{1}{m^2}\sqrt{b^2\sigma_m^2 + m^2\sigma_b^2}\,, \tag{2.20}$$

where σ_m and σ_b is calculated as

$$\sigma_b = \sqrt{\frac{1}{\Delta}\sum_{i=1}\frac{F_i^2}{\sigma_i^2}}\,, \tag{2.21}$$

$$\sigma_m = \sqrt{\frac{1}{\Delta}\sum_{i=1}\frac{1}{\sigma_i^2}}\,. \tag{2.22}$$

2.3 Verification of DFM by round-robin experiments

Over the years of damage frequency method application, reliability and practicability of this procedure has been tested by several round-robin experiments [37, 39, 40]. As an example, let us examine the round-robin experiment for the measurement of the 1-on-1 LIDT testing by DFM for typical laser components at 1064 nm [38–40]. Within this campaign, three laboratories were asked to test six different types of samples:

1. Highly reflective coatings at AOI 0° with protective layer: HR 0° PL;
2. Highly reflective coatings at AOI 0°: HR 0°;
3. Highly reflective coatings at AOI 45°: HR 45°;
4. Anti-reflective coatings: AR 0° beids;
5. Uncoated substrates from fused silica: SUP uc;
6. Uncoated substrates from borosilicate glass: BK7 uc.

For each sample type, four identical optical elements were tested to increase the statistical certainty. Since each laboratory used different laser sources, it

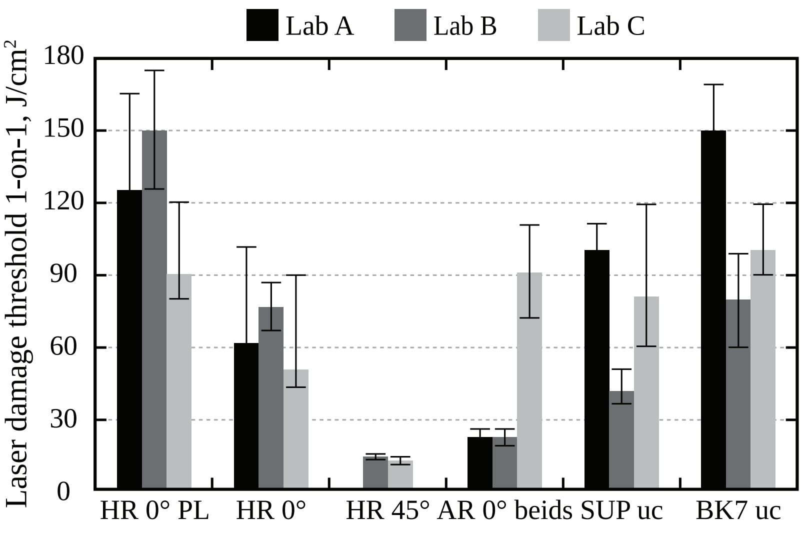

Figure 2.9 Result of a round-robin experiment for 1-on-1 LIDT testing at 1064 nm and ns-pulses. Data are adapted from Ref. [234].

was not possible to ensure a fully uniform testing conditions. The pulse duration of the laser systems was in the range of 10 to 15 ns, and the test spot diameter differed from 160 to 600 μm. Furthermore, the pulse energies necessary for achieving the same energy density varied by a factor of 15 among testing institutions. The results of reported LIDT values during this round-robin experiment are shown in Fig. 2.9. The presented comparison caused a lot of scientific debates. On the one hand, it is clear that the LIDT values of the same samples determined by different laboratories are widely scattered. This indicates probable errors during the damage test or the data processing. On the other hand, results are comparable within reported uncertainty intervals because error budget stated by the testing institutions was large. Thus, the study declared that LIDT values determined according to DFM are repetitive within the reported uncertainty interval. However, these results raised a huge concern among optical equipment developers and users. Despite the fact that results are comparable, reported uncertainty intervals are too large to remain informative. For instance, the LIDT value of uncoated substrate from borosilicate glass reported by Lab A is 150 J/cm^2. The uncertainty interval states that it might vary from 75 to 170 J/cm^2 (Fig. 2.9). If a reported LIDT value varies within the range of 100 J/cm^2, neither the developer or the user of the optical element can benefit from this information. Similar situation can also be observed for samples HR 0° PL, HR 0° and SUP uc (Fig. 2.9). However, the LIDT values reported for samples HR 0° (Lab A and Lab B) and AR 0° beids (Lab A and Lab B) appear to be both accurate and repeatable (Fig. 2.9). While test parameters (laser beam size and pulse duration) varied among laboratories, it remained the same for each type of samples in each testing institution. Thus, the observed behaviour cannot be attributed only to the variability of the test parameters. Other issues, such as error budget evaluation, data processing algorithm [216, 234] and operator experience [234] should be considered.

Damage frequency method is a statistical procedure. Thus, in order to obtain accurate and repeatable results, a human error free statistical data should be collected. In practice, it is hard to fulfil this requirement due to the limited size of test samples. During the LIDT test, two opposite conditions should be balanced. On the one hand, the more sites are tested at one particular fluence level, the smaller uncertainty of measured damage probability is ensured. According to the ISO-21254 standard, the minimum amount of points exposed at one fluence level should be at least 10. On the other hand, in order to successfully apply DFM procedure it is necessary to have a sufficient quantity of data points within a transition interval between zero and one damage probability. If the transition region is narrow and there is no previous information on the optical resistance performance of the test sample, these requirements become hard to fulfil. Another factor that impedes data processing algorithm is the shape of the damage probability curve. It has been shown that in many cases the linear damage probability dependence on fluence might not be observed or could be hardly distinguished [45, 49] (Fig. 2.10: A). Furthermore, in many cases, the selection of damage probability data points used for linear fitting depends on the operator's personal experience. ISO-21254 standard does not provide a recommendation on how the linear interval should be selected in the case shown in Fig. 2.10: B. Since the rules are not strictly defined, the same damage probability curve can be fitted differently by two operators (Fig. 2.10: B). Finally, the applicability of the fitting procedure and the fitting model should be addressed. Several improvements in linear fitting procedure have been suggested, such as regression function transformation into linear form [216] or damage probability data smoothing by applying simple moving average concept [232]. However, the main sources causing poor DFM performance are still not clear.

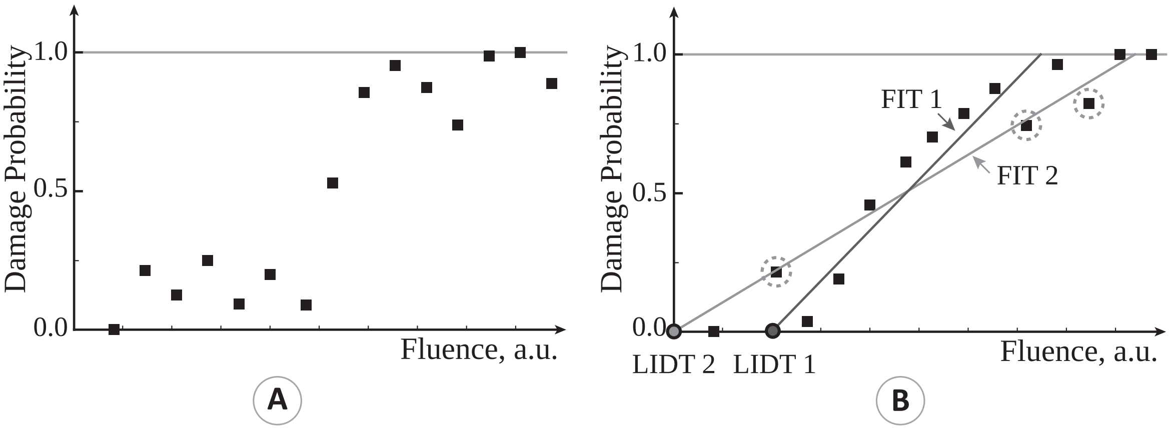

Figure 2.10 **A:** example of damage probability curve, when the interval with linear damage probability dependence on the applied peak fluence is hardly distinguished. **B:** example of two possible fittings for one damage probability curve. Fit 1 excludes marked points, while Fit 2 is with the points included.

Also, a Monte Carlo model has been used to check that the accuracy and repeatability problems of LIDT values determined by DFM indeed exist [232]. An experimental error free 1-on-1 damage probability measurement has been performed on the synthetic sample, featuring a degenerate defect ensemble. The defect density was set to 1000 defects/cm^2 and the onset damage threshold was set to 150 J/cm^2. Damage probability has been tested for 10 peak fluences. At each particular fluence, 30 sites have been exposed. That resulted in 300 tested sites overall. Such quantity of test sites is compatible with the real world measurements limitations. The LIDT was determined from the damage probability curve using linear regression and least squares fitting. Measurement was repeated for 1000 synthetically generated samples. Distribution of estimated LIDT values is presented in Fig. 2.11. It is clearly seen that the distribution of reported LIDT values features both systematic and random deviation from the onset value. This indicates that both the fitting procedure and the fitting model can be inadequate. Thus, the goal of this study is to perform detailed DFM analysis in order to understand how the experimental issues (such as fluence fluctuations) and the data processing algorithm (fitting procedure and fitting model) affect the reported LIDT results.

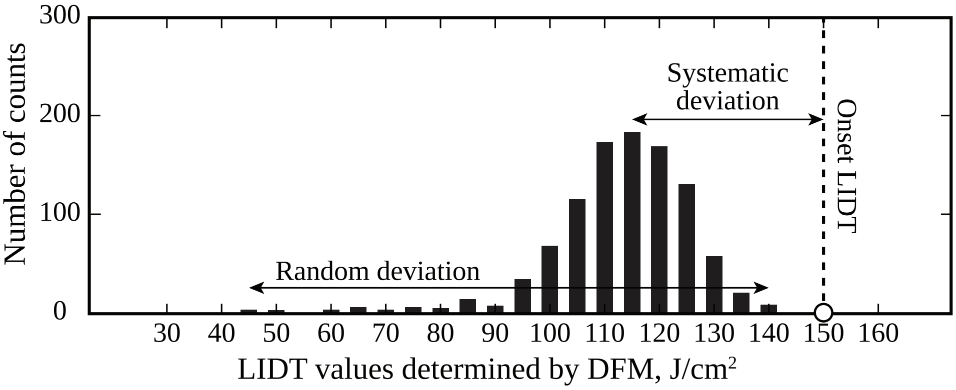

Figure 2.11 A histogram of the LIDT results determined from 1-on-1 LIDT test using DFM procedure based on least squares fitting.

2.4 Discussion: uncertainty sources in LIDT testing

In this Section the applicability and effect of the fitting method are discussed. According to the ISO-21254, both the damage probability and the fluence are supposed to have a normal probability distribution. Thus, the linear least squares regression can be applied for the LIDT determination. Within this Section, the PDFs and uncertainty intervals of both variables are investigated in order to test this assumption.

2.4.1 Statistical uncertainty of the damage probability

Basically, optical resistance measurements might be considered as a Bernoulli experiment with possible “1 – damage” and “0 – no damage” result as an outcome. By doing n such experiments we can analyze the measured probability data in two ways. The first approach is to consider the measured probability (a ratio k/n) as a random variable of normal distribution with a standard deviation [235, 236]:

$$\sigma_P = \sqrt{\frac{p(1-p)}{n}}\,. \tag{2.23}$$

This consideration is valid with the high confidence for the measured intermediate probability levels (in the proximity of 0.5) suggesting that a least squares linear fitting is appropriate for regression. However, if the measured probability is close or equal to either 0 or 1, the probability distribution deviates from normal and the reported uncertainty interval is in conflict with experimental data. In other words, the measured probability is never negative or higher than 1. However, the σ_P allows the measured data points to be distributed around the mean with equal probability in both directions, thus also negative (Fig. 2.8). This discrepancy is overcome by using the second approach, and namely, the Bayesian interpretation of binomial data published in the work of A. Hildenbrand and coworkers [237]. It has been demonstrated that, even though the damage probability p is derived from the Poisson statistics, due to only two possible outcomes the DFM testing results in a probability distribution that is binomial in nature. Accordingly, the probability to receive exactly k successful outcomes after n trials, assuming probability of success p, is defined by the binomial PDF:

$$\mathrm{PDF}_P(k|n,p) = \binom{n}{k} p^k (1-p)^{n-k}\,, \tag{2.24}$$

where $\binom{n}{k}$ is a binomial coefficient. As we can see, the result of binomial experiment is non-deterministic: n different outcomes can be obtained in principle. We call it "vertical uncertainty interval" of the measurement. Now let us consider the PDF_P – a probability density function. An outcome of real world p measurement in LIDT experiment, $p_{\text{est}} = k/n$ is obtained and it is not necessarily equal to p – the idealized (Poisson) probability of damage that needs to be measured. Though the p value is never known prior to the real world experiment, we can estimate the likelihood of all possible values of p within the interval 0 to 1 by applying experimentally obtained n and k values from p_{est} in combination with binomial distribution. In this particular case, the outcome of Eq. 2.24, PDF_P, is always maximized at $p = p_{\text{est}}$. This can be proven numerically. Variation of p will draw a distribution that depends on the numbers of damaged and tested sites, k and n (Fig. 2.12: red distributions). We can benefit from this distribution when analyzing the nonlinear fitting of damage probability data. It defines how probable the tested p_{est} value is. Integration over 95% area of the defined distribution can be used for uncertainty interval calculation. This could be done for each damage probability data point obtained at different fluence. The distributions obtained following the binomial formula are asymmetric when the damage probability is close to 0 or 1. Thus, the statistical error bars were shown to be asymmetric in this range, too [237]. Asymmetric distributions suit well the physical damage probability model. No negative or higher than 1 damage probability values are possible.

2.4.2 The nature of laser fluence uncertainty

In the LID testing experiments the estimation of laser fluence is one of the most important steps determining the overall accuracy of the measurement. By discussing the details we presume that all the LIDT tests are performed in the configuration recommended by ISO standards [9, 223] where laser fluence is varied by attenuator consisting of $\lambda/2$ plate and polarizer. Typically the

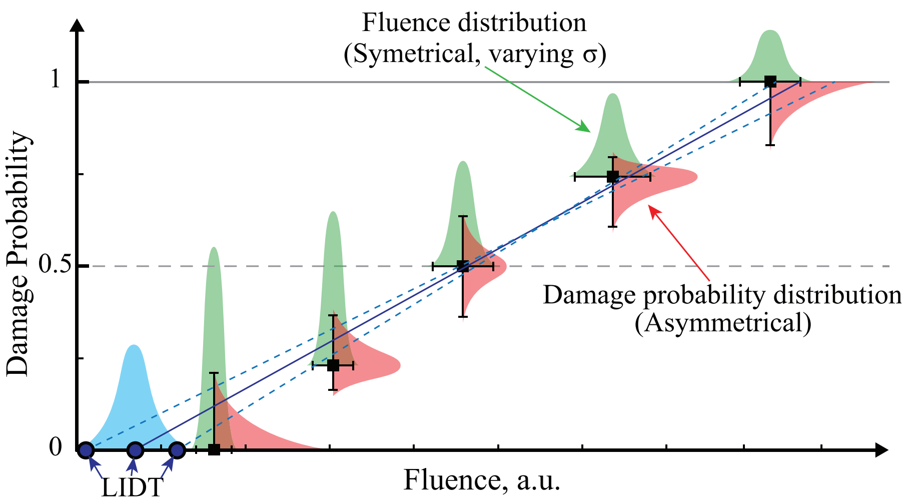

Figure 2.12 The investigation of damage probability curve uncertainty intervals: normal distribution of measured average laser peak fluence (green); asymmetric nature of damage probability distribution (red); distribution of LIDT (measurand) outcomes caused by fitting procedure (blue).

shot to shot laser pulse energy fluctuations are of normal distribution and their amplitude is described by a standard deviation parameter:

$$\mathrm{PDF}_F(F_\mathrm{p}, \sigma_F) \propto \exp\left[-0.5\left(\frac{F - F_\mathrm{p}}{\sigma_F}\right)^2\right]. \tag{2.25}$$

Since the amplitude of fluctuations is directly proportional to the average laser fluence F_est, the standard deviation $\sigma_F = \mathrm{const} \cdot F_\mathrm{est}$ varies in absolute scale of fluence when the average laser power is adjusted by attenuator (Fig. 2.12: green distribution). As it will be shown later, fluctuations and their amplitude have an impact on the measured damage frequency. We call it “horizontal uncertainty” of the measurement (Fig. 2.12). In practice three different factors exist that might affect the horizontal uncertainty. These are the laser pulse energy, the beam diameter and the shape variation on a pulse-to-pulse basis. For the sake of simplicity only the pulse energy variation described by a normal distribution of fluence is considered here. Other effects, however, can be treated in similar manner.

2.5 Discussion: the fitting procedure

The LSE is based on assumption that the measured variables feature normal distribution and display the same (constant) amplitude of standard deviation. In order to apply the LS method, several strict assumptions should be satisfied.

1. **Linearity and additivity**. The dependent variable should have a linear relationship to the independent variable. In our case, the dependent variable is damage probability and the independent variable is fluence. It is assumed that within every measured damage probability curve, a region where damage probability depends on fluence linearly can be distinguished. In previous ISO standard (ISO-11254) [9], it was recommended to use damage probability in the range of 0.05 to 0.6 for linear fitting application.
2. **Homoscedasticity.** For each value of fluence, the probability distribution of damage probability should have the same standard deviation σ (Fig. 2.8).
3. **Statistical independence.** For any given value of fluence, the damage probability values should be independent.
4. **Normality.** For any given fluence value, the values of damage probability should be roughly normally distributed – meaning that its PDF is Gaussian and symmetric.

As it was demonstrated, this is not the case: neither the damage nor the fluence PDFs are normal. Since the application of the least squares method for a damage probability curve fitting procedure is inadequate, this can explain a wide random scattering of the measured LIDT values observed in Fig. 2.11 and other researches [48, 238]. A possible solution here is to replace the least squares approach by another appropriate approach – the maximum-likelihood estimation (MLE) [239].

2.5.1 Maximum-likelihood approach

In order to explain the main principle of the maximum-likelihood approach, let us consider a following example. Suppose a random continuous variable X, the probability distribution of which depends on some unknown parameter θ (Fig. 2.13: A). Since θ is unknown, every damage probability distribution should be considered equally probable prior to the measurement. After a measurement, when a data set of X values (x_1, x_2, ..., x_n) are obtained, it becomes clear that some probability distributions (and consequently, θ values) are more probable than others (Fig. 2.13: B). Thus, the primary goal is to find a point estimator $u(X)$ such that $u(x_1, x_2, \ldots, x_n)$ is a "good" point estimate of θ.

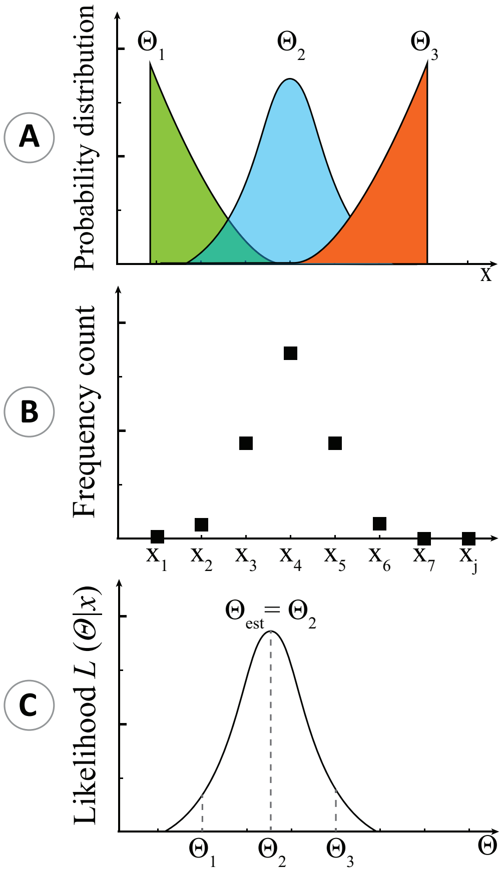

Figure 2.13 The principles of the maximum-likelihood estimation.
A: probability distribution dependence on θ parameter of a random continuous variable X. **B:** measured probability distribution of the random continuous variable X, which indicates that some θ values are more probable than others. **C:** likelihood function, which finds the most probable θ values for the observed measurement. In this case, the best θ estimate is the most likely θ value for observed distribution.

It seems reasonable that a good estimate of the unknown parameter θ would be the value of θ that maximizes the probability or the likelihood of getting the observed data distribution. In practice, such likelihood is evaluated through a combination of PDF and likelihood function [239]. PDF defines the probability of observing data vector *x* given the parameter θ. In general, the parameter $\theta = (\theta_1, \ldots \theta_n)$ is a vector defined on a multidimensional parameter space. If individual observations x_i are statistically independent of one another, then, according to the theory of probability, the PDF for the data $x = (x_1, \dots, x_m)$, given the parameter vector θ, can be expressed as a multiplication of PDFs for individual observations:

$$f(x = (x_1, x_2, \dots, x_n)|\theta) = f_1(x_1|\theta)f_2(x_2\theta)\dots f_n(x_m|\theta)\,. \tag{2.26}$$

In reality, however, we have already observed the data. Accordingly, an inverse problem should be solved. Given the observed data and a model of interest, find the one PDF, among all the probability densities that the model prescribes, that is most likely to have produced the data. To solve this inverse problem, we define the likelihood function (Fig. 2.13: C) by reversing the roles of the data vector *x* and the parameter vector θ in $f(x|\theta)$:

$$L(\theta|x) = f(x|\theta)\,. \tag{2.27}$$

Thus, $L(\theta|x)$ represents the likelihood of the parameter θ, given the observed data x, and as such is a function of θ. In general, the likelihood function can be interpreted as the joint probability density function of data x:

$$L = \prod_{i}^{n} f(x_i, \theta)\,. \tag{2.28}$$

2.5.2 The role of model function

The model function used to fit the experimental data is another important factor that can cause large systematic deviation from the onset LIDT value observed in Fig. 2.11. Two issues should be considered here: this model function and the experimental uncertainty parametrization. As discussed at the beginning of this Section, the identification of linear dependence interval might be a difficult task. This problem can be avoided if the damage probability curve is fitted by a model function described in Eq. 2.18. This can be readily achieved by applying the maximum-likelihood approach.

2.6 Monte Carlo model for LIDT testing

A Monte Carlo based LIDT measurement model has been created. It emulates a plain sample surface covered with uniformly distributed defects (Fig. 2.14). A single defect is interpreted as a point with randomly generated coordinates. In the context of this work, all defects feature (but are not limited to) the same damage threshold. This corresponds to the degenerate ensemble of defect distribution. The sample surface is divided into horizontal and vertical sections. Horizontal sections are dedicated for constant tested fluences. Vertical divisions define sites tested at each particular fluence. Thus, the subdivided surface might be interpreted as a matrix of testing sites used for real LIDT measurements. Each section is virtually scanned with simulated laser

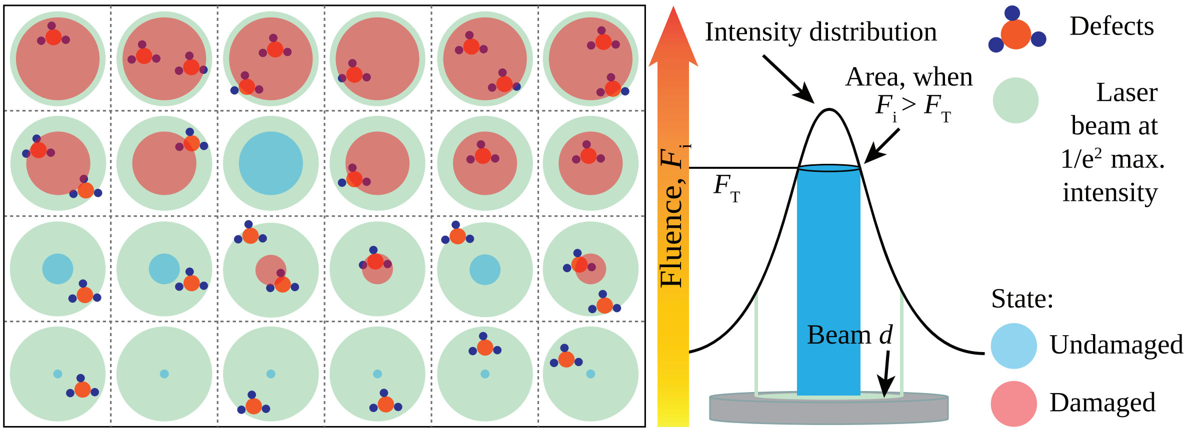

Figure 2.14 The principle of Monte Carlo based LIDT measurement model. Sample surface is divided into sections corresponding to fluence levels and number of sites tested at each fluence value. Green circle is laser beam area S limited by fluence level F_p/e^2. Inner circle (marked either blue or red) is used to scan for defects. It corresponds to the area above F_T. Radius of this circle is changing according to possibility for damage to occur. Red colour identifies damage event, blue colour means that tested site is non-damaged.

beam spot at $1/e^2$ level of F_p (green circle). Damage occurs only when the applied localized fluence is higher than the predefined threshold of the defects (Fig. 2.14). Therefore the area of the inner circle (blue or red) changes according to Eq. 2.8. If at least one defect passes into the inner area, the virtual testing site is registered as damaged (red). Otherwise, it is treated as non-damaged (blue). Damaged sites are indicated as $k_i = 1$ and non-damaged as $k_i = 0$. Such a marking allows a simple damage probability estimation. The LIDT determination is possible using various linear and nonlinear model functions in combination with appropriate regression methods. Additionally, peak fluence fluctuations can be included into the LIDT measurement simulations. This helps to keep virtual model closer to the actual measurements. Virtual LIDT measurement base can be used to determine how well the differently obtained LIDT results correlate with the onset value. It might also be used to investigate how much the LIDT values are reflected or underestimated due to various changes in testing parameters. Therefore, the LIDT measurements simulation model is a convenient tool for the detailed DFM investigation.

2.7 Results

2.7.1 Effect of fluence uncertainty

Any experimentally collected data are affected by the measurement uncertainty. Thus, experimental uncertainties should be well parameterized and model function should be expanded to compensate the effects of measurement-caused data fluctuations. Studies of discrepancies in the damage probability curve due to nonrepeatable fluence in every interrogating laser pulse have been carried out under the following conditions. A sample featuring the degenerate defect ensemble has been simulated using the previously described Monte Carlo based LIDT measurement model. The onset damage

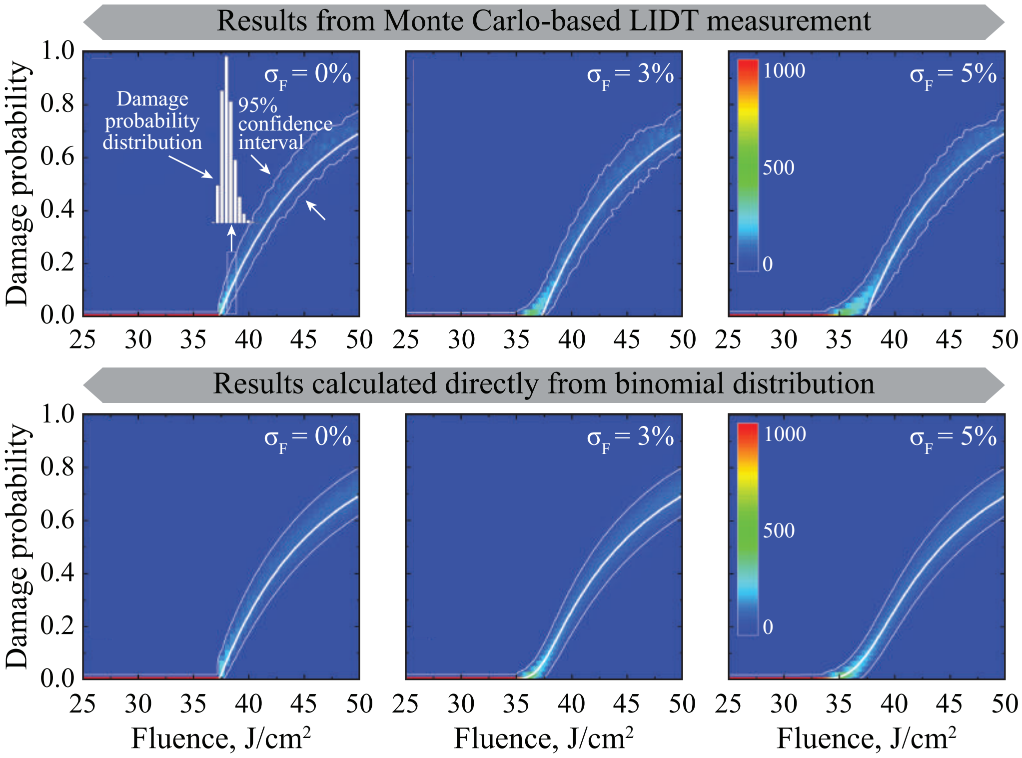

Figure 2.15 The statistical results of virtual LIDT experiments. In **top row** the background picture denotes the histograms of measured damage probability after 1000 virtual experiments when interrogating the sample having an idealized damage probability (degenerate ensemble), indicated by the white line in the middle. The **bottom row** indicates the theoretical prediction of the Monte Carlo experiments. In this case the white line in the middle corresponds to the improved fitting function defined by Eq. 2.30. Colour intensity corresponds to the number of counts in the damage probability distribution.

threshold of defects was 37 J/cm^2. The defect density on the sample surface was set to 1000 defects/cm^2. Following the ISO standard requirements the beam radius was 500 μm. The fluence applied for the measurement varied from 25 up to 50 J/cm^2 with 0.1 J/cm^2 increment. The damage probability has been estimated for 250 mean peak fluences overall. Fifty sites have been virtually examined at each fluence. Up to fifty sites per one average peak fluence were chosen in order to collect sufficient statistical data and to minimize the statistical (vertical) uncertainty. Wide discrepancies of damage probability data would impede the investigation of fluence uncertainty by introducing additional effects in the damage probability curve. Such procedure is repeated for 1000 times and two-dimensional statistical distributions (histograms) have been depicted. The same procedure has been repeated by introducing fluence noise characterized by standard deviation varying up to 5%. The distributions of obtained histograms tend to bend due to increased noise (Fig. 2.15: top row). Hence, the fluence noise affected data differs from the theoretical model described by Porteus and Seitel 2.18 (Fig. 2.15: top row, white middle curve). Furthermore, as expected, the histograms were asymmetric due to their binomial nature close to the onset value of LIDT. These discrepancies might be interpreted as an introduced systematic uncertainty of the LIDT measurement. Fitting of obtained measurement data by currently existing linear or nonlinear models leads to underestimation of LIDT.

2.7.2 Maximum-likelihood application

In the case of LIDT testing, the maximum-likelihood approach links each pair of measured damage probability data (k_i/n_i) and average peak fluence F_{0i} individually with PDF_{Pi} defined by Eq. 2.24 and normalized [237]. Maximum-likelihood function L is constructed by using a selected model function according to Eq. 2.18 and PDF_{Pi} corresponding to each damage probability data point. To obtain the best maximum-likelihood estimates of unknown parameters M, F_T and σ_F, the likelihood function L is calculated numerically.

$$L = \prod_i \mathrm{PDF}_{Pi}(F_\mathrm{T}, \sigma_F, M \mid n_i, k_i, F_{\mathrm{p}i})\,. \tag{2.29}$$

If σ_F is known from the measurement, it might be considered as a constant of *a priori* knowledge before conducting the experiment and analyzing the data. Then the variation of function L above the parameter space of M and F_T will result in a mapped surface (Fig. 2.16: A). Colour intensity in the map indicates the likelihood of the parameter set. In general, the numerical values of L function might be very large and can impede the numerical calculation. Thus, often the logarithm of the likelihood function is used. The most suitable combination of parameters will maximize the L function. We consider those parameters as the best fit approximation. In general, σ_F can also be varied and estimated from a fit.

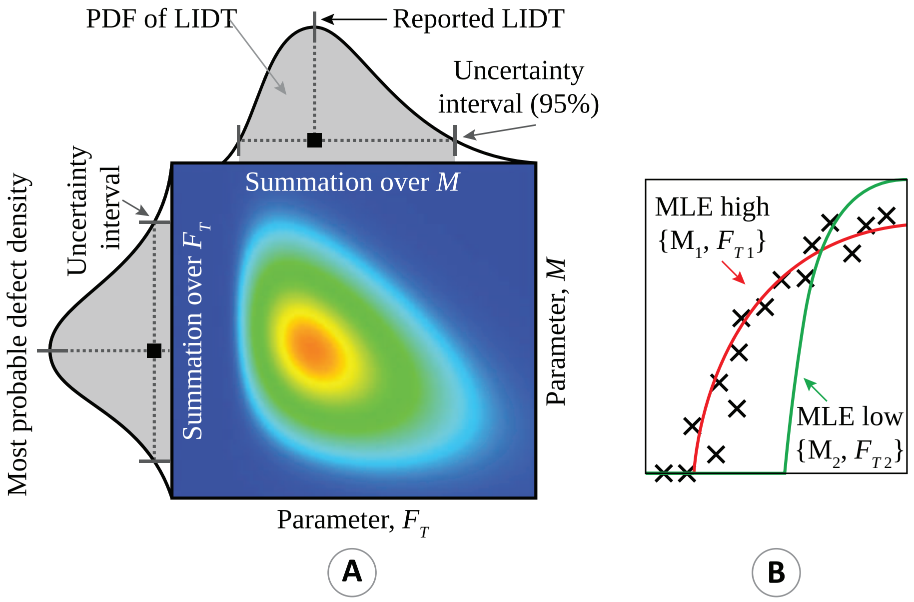

Figure 2.16 A typical result obtained from the maximum-likelihood function maximization. For simplicity the fluctuations of fluence are fixed to a measured value.

The same approach would also work with other types of defect ensembles. However, the type of ensemble function should be known or guessed before analyzing the data. The MLE technique also allows the calculations of uncertainty as coverage intervals, both for the estimated defect density and the damage threshold at specified coverage probability. It might be evaluated by integrating the obtained L surface over one of the parameters (Fig. 2.16: B). As it is be seen, the reported uncertainty interval of LIDT measurement corresponding to 95% coverage interval is asymmetric and also non-negative. This result of practical importance is in agreement with the nature of the LIDT testing.

2.7.3 Revised testing procedure

To overcome the abovementioned limitations, several improvements are suggested. Firstly, a way to improve the chosen fitting function for damage probability analysis is introduced, which is capable of taking into account the shape distortion caused by the measurement and the uncertainty of peak fluence. Fluctuations of fluence are considered as a parameter that can either be measured prior to damage testing procedure or used as a free fitting parameter in the case when damage probability is known to experience a steep, deterministic transition. Secondly, the fitting procedure should be compatible with the asymmetric nature of PDF_P. Here, the MLE is applied, since it is a well-known procedure, which can be used with nonsymmetric distributions of the variables.

In the case when damage is driven by identical surface defects, Eq. 2.18 derived directly from Poisson statistics has a steep transition from zero to higher damage probability (almost linear for lower $P(F_{0i})$ part) and only includes two model parameters. These parameters are the defect density M and the damage threshold of defects F_T. However, as shown by Monte Carlo simulations, the typical experimental damage probability data has a smooth S type transition as a function of fluence. Such transition is mostly related to the averaging effect of laser pulse-to-pulse instability. To extract the true LIDTs, an appropriate data regression model has to be used. This can be done by parameterizing the damage probability curve by means of σ_F. Since the averaged fluence F_{0i} is used for plotting the measured probability data, the theoretical Eq. 2.18 convolved with a varying kernel of Gaussian distribution (Eq. 2.25) defined by standard deviation is a good candidate for a fitting function:

$$p_{\text{est}}(F_{i\ \text{average}}) = P(F_{\text{p}i}, F_{\text{T}}, M) \otimes \text{PDF}_F(F_{\text{p}i}, \sigma_F i)\,. \tag{2.30}$$

This assumption is further tested numerically by performing the Monte Carlo experiments.

2.7.4 Application of revised fitting procedure

We investigated the validity of newly proposed fitting function correction 2.30 by simulating the ideal outcome of Monte Carlo experiment. Two-dimensional model histograms of damage probability were calculated under the previously introduced experimental conditions. By doing so, we take the damage probability predicted by the improved fitting function 2.30 and combine it with PDF_P binomial distribution 2.24. As can be seen, both the Monte Carlo (top row) and the theoretical prediction (bottom row) distributions perfectly match each other. The improved fitting function (Fig. 2.15: bottom row, white curve) is sensitive to the damage probability changes due to the fluence instability. Accordingly, it is capable of predicting the data of non-ideal LIDT testing experiment. As the fluence noise parametrization is correct, it is useful for damage threshold evaluation. When combined with the MLE fitting technique, it allows one to correct the LIDT determination independent of the fluence instabilities. Furthermore, other types of defect ensembles or their combinations can be applied by using the same strategy. Thus, the fluence noise has to be characterized prior to the evaluation of damage probability.

2.7.5 Comparison of DFM testing reproducibility

The developed nonlinear and fluence uncertainty sensitive LIDT estimation model, employing Bayesian (maximum-likelihood) fitting approach, has been compared with the standard least squares procedure with a linear fitting function regarding its accuracy and repeatability. One thousand Monte Carlo based measurement's have been simulated to collect reliable statistics of DFM data. Data were analyzed by employing both classical and improved approaches. Simulation's conditions are summarized in Fig. 2.17. Onset 3% standard deviation from the mean fluence values was allowed for in virtual measurements. For each measurement, the standard and proposed approximation models have been applied for the LIDT determination. Distributions of obtained LIDT values are drawn in Fig. 2.17. As predicted, the statistical distribution of LIDTs estimated by ISO least squares method linear fitting is broad. Poor accuracy determines a large uncertainty interval. Practically, it means that the calculation of LIDT value is unreliable and might incredibly differ from the real damage threshold value. However, a nonlinear fluence-noise sensitive model is shown to feature better accuracy and repeatability. Such discrepancies observed between the two methods can be directly linked to the presented uncertainty studies of damage probability curve data. Firstly, the least squares regression is incompatible with an asymmetric and varying distribution of the variables. So, this application of the wrong approximation technique is unable to produce a correct value continuously. On the other hand, neglecting the fluence-caused transformation of damage probability curve causes additional

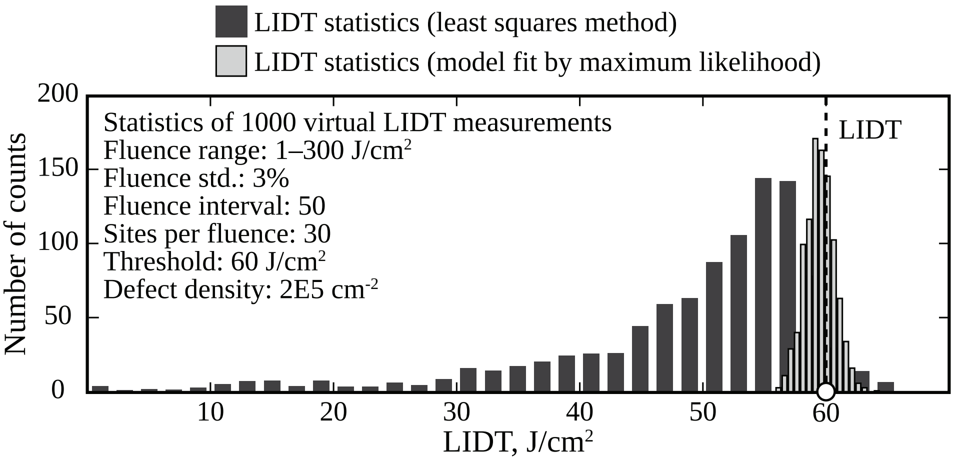

Figure 2.17 A statistical comparison of LIDT values determined by the error sensitive maximum-likelihood based model fit and the ISO least squares linear fitting regarding accuracy and repeatability.

systematic uncertainty using any fitting procedure. In this case, a theoretical model will not explain the measured data. Once again calculated LIDT could not be estimated correctly without considering all of the factors. The accuracy of the revised fitting procedure can be limited by a few factors. Firstly, the effect of the statistical damage probability (vertical) uncertainty has been neglected. In practice, the number of test sites at a particular fluence level is limited by the sample size. If the damage probability data is statistically unreliable (for instance, less than 10 points are tested at each fluence), then the vertical uncertainty of each data point in the damage probability curve will be large. The larger the vertical uncertainty, the larger will be the uncertainty of the measured LIDT. Furthermore, the suitability of the model function should be considered. In our analysis, the degenerate defect ensemble has been assumed. However, this model might oversimplify or deviate from the reality. Fitting with a nonideal model would also enlarge the overall LIDT uncertainty. Finally, the influence of other measurement uncertainty sources such as pulse duration [20] and deviations from the beam shape should be addressed, since they might also result in the changes of damage probability curve.

Application of advanced fitting procedure to the real world samples

In order to prove the validity of the revised fitting technique, two conventionally polished and SiO_2 deposited fused silica samples were tested regarding their damage threshold. Measurement test bench and sample irradiation conditions are described in **Subsection 2.2.3**. One of the samples was chemically etched for 2 min. Typical morphology of LID on both samples is shown in Fig. 2.18. Damages dominating on the non-etched sample consist of multiple clearly separated dots. Polished surfaces contain various absorbing centres (nano-defects). They cause the observed damage pattern. Chemical etching reduces this type of damage precursors. Most damages on the non-etched sample originate from discrete defects localized on the surface.

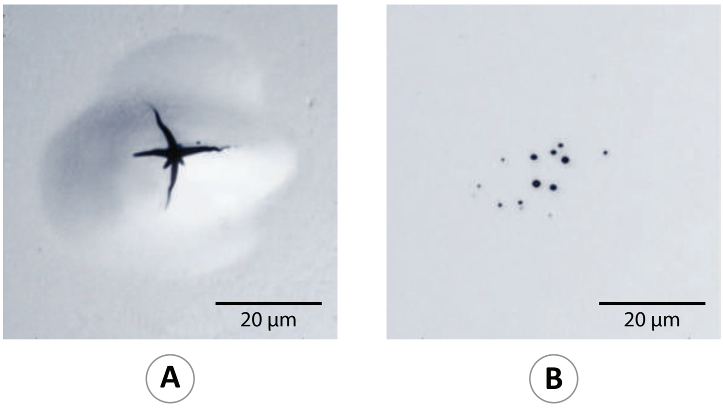

Figure 2.18 A typical morphology of LID on etched (**A**) and non-etched (**B**) samples.

The raw data obtained by the previously described LIDT testing conditions are presented in Fig. 2.19. The damage probability curve of the nonetched sample is steep. This behaviour is defined by a large quantity of low damage threshold nano-defects distributed over the whole surface. In the case of an etched sample, the threshold curve with two kinds of defects is obtained. The density of the nano-defects (the first type of defects) is minimized by chemical etching. Thus, a secondary type of defects is revealed. The damage threshold of the secondary defects is assumed to be the onset LIDT of the material. The model fit by maximum-likelihood and the ISO least squares fit were applied for the LIDT determination. According to the modelling results (Fig. 2.15), data of the damage probability curves is assumed to be distorted by the fluence uncertainty. This distortion might be characterized using a varying kernel of Gaussian noise function (corresponding to the estimated fluctuations of peak fluence). In this particular case, the fluence fluctuations were characterized by an energy meter and a CCD camera prior to the measurement. The standard deviation of the fluence σ_F was estimated to be of about 10%. This number was used as a constant fitting parameter. The characterized kernel function was convolved with the damage probability model function. In the case of one type defects, it is directly derived from the Poisson statistics 2.9. A concept model of the damage probability curve with multiple kinds of defects is presented by J.Y. Natolli and co-workers [235]. The degenerate defect ensemble was assumed for all types of observed defects. Then the revised fitting function was used in combination with the MLE technique. As can be seen from Fig. 2.19, the model was capable of reproducing the measured data with high confidence for both samples. Damage thresholds and defect densities were extracted by maximizing the likelihood function (Table 2.1).

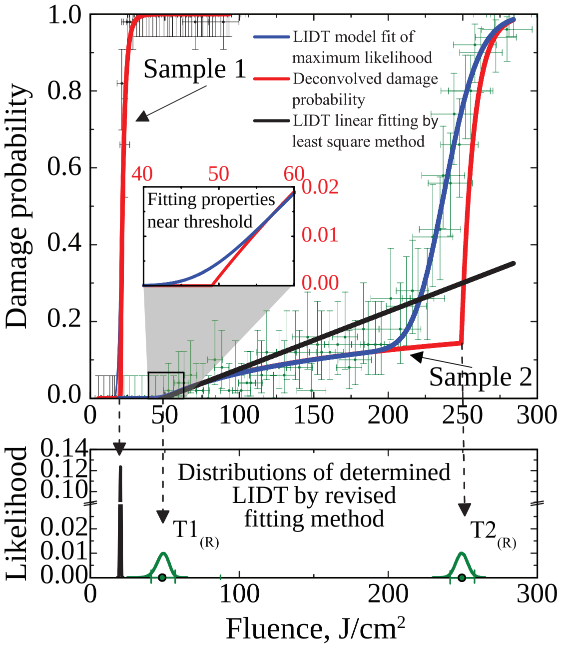

Figure 2.19 An example of the revised fitting application for to determine the LIDT of different fused silica samples.

Experimental uncertainty intervals were calculated in accordance with the previously described techniques (Subsections 2.1 and 2.7.3). They were found to be asymmetric and very small compared to the noise parameter σ_F. Another advantage of the maximum-likelihood approach is the ability to extract the damage threshold and the density of secondary defects. This information is complementary when evaluating the sample quality in comparative tests. Though wide statistical data were collected for the LIDT measurement, it was not enough to apply the ISO least squares fitting technique in the case of the

Table 2.1 The comparison of LIDTs estimated by the revised fitting method (R) and the ISO least squares method using a weighted linear fitting (S). An X means the value is not possible to extract.

Samples	**Non-etched**	**Etched**
$T1_{\mathrm{S}}$, J/cm^2	X	142±5723
$T1_{\mathrm{R}}$, J/cm^2	44.2≤45.6≤47.1	87≤109≤125
$M1_{\mathrm{S}} \cdot 10^6$, defects/cm^2	X	X
$M1_{\mathrm{R}} \cdot 10^6$, defects/cm^2	3.9≤4.8≤6.0	0.3≤0.4≤0.5
$T2_{\mathrm{S}}$, J/cm^2	Does not exist	X
$T2_{\mathrm{R}}$, J/cm^2	Does not exist	539≤556≤573
$M2_{\mathrm{S}} \cdot 10^6$, defects/cm^2	Does not exist	X
$M2_{\mathrm{R}} \cdot 10^6$, defects/cm^2	Does not exist	6≤13≤19

non-etched sample successfully. According to the standard procedure, the linear fit must be applied for the damage probabilities between 0.05 and 0.6. No data were recorded within this range for the unetched sample. So, by using the standard approach, the measurement should be repeated to collect the missing information. However, this is not required by the improved fitting approach. Furthermore, it is also clearly seen (Eq. 2.19) that the linear fitting with LS regression is inapplicable in the case of two dominating defect ensembles. The calculated LIDT value is overestimated (Table 2.1) due to the slope discontinuities. Considering the improvements in optical element coating and manufacturing technologies, we believe that a nonlinear regression model might become an important alternative to be considered for the LIDT determination.

2.8 Conclusions

Within this chapter, the practical importance of considering the laser peak fluence-noise caused uncertainty in the LIDT measurements has been investigated. Two types of uncertainties were proved to limit the accuracy of the ISO recommended damage threshold testing procedure. Firstly, the statistical damage probability distribution is asymmetric (binomial) in nature. Therefore, the linear regression based on the least squares fitting causes significant deviations due to the systematic uncertainty when determining the LIDT. Secondly, the fluence uncertainty intervals of the LIDT measurement data are non-constant variables. They change on the absolute value by varying the average laser peak fluence. Accordingly, the collected damage probability data suffers from a systemic uncertainty of the applied fitting function. These findings suggest several courses of action for the LIDT metrology improvement. A new concept of fluence uncertainty interval parameterization has been proposed for the construction of an improved damage probability model curve. It has been validated by Monte Carlo simulations. The validity of dynamic Gaussian kernel function was tested on synthetic and real experimental data. For the first time, it has been shown that the maximum-likelihood technique in combination with the proposed fit model features superior reproducibility and accuracy of the LIDTs determined by the DFM laser damage testing method. Furthermore, a nonlinear regression based on maximum-likelihood algorithm has been used to estimate both the realistic error bars of the LIDT measurement as well as the rough measure of the damage precursor density. The improved model of the experimental damage probability curve, considering the fluctuations of fluence, has been shown to reproduce the characteristic features of real-world experimental data and, therefore, is of practical importance.

3 Quantitative evaluation of laser damage precursors

"By doubting we are led to question, by questioning we arrive at the truth."
Peter Abelard, a medieval French preeminent philosopher and theologian.

Material related to this chapter is published in *A1, A7, C1*

In **Chapter 2** we have discussed a statistical model which relates the damage probability to a defect ensemble and defect density. Defect density can be estimated directly from the damage probability measurements by applying the revised LIDT testing procedure presented in **Chapter 2**. However, in that case, the defect ensemble (distribution of the threshold fluences) is never known prior to the measurement and is only assumed. Thus, the main goal of the presented study is an attempt to determine the true defect ensemble.

Investigation starts with a closer look at the existing assumptions about the defect ensembles. Two approaches are used to extract the distributions of localized damage precursors (defects), namely, the damage probability, which was presented in **Chapter 2**, and the damage density measurements, which will be introduced within this Chapter. Testing is performed on uncoated and having SiO_2 monolayer film coated fused silica substrates exposed to pulsed UV irradiation (355 nm, 4.8 ns). Then a direct comparison of the defect ensembles obtained from both methods is carried out. Our analysis indicates apparent differences between the two methods that are discussed in detail.

3.1 Defect ensembles of laser damage precursors

Since the concept of defect ensembles has been introduced, several different hypotheses were made about the possible distribution functions used to define defect ensembles. Herewith we discuss the four common assumptions: degenerate [43, 44], power law [44, 46, 50], Gaussian [47] and mixed defect ensemble [45, 48, 49].

Degenerate approach assumes that all the defects located on or within the optical sample are identical and feature the same threshold fluence. It was discussed in detail in **Chapter 2**. Defect ensemble is defined via delta-function (Fig. 3.1: A) [43, 44]. In this case, the damage probability curve features a distinct bend at the threshold fluence. The LIDT is strictly defined as the highest fluence with zero damage probability.

With **Power law** approach, defect density dependence on peak laser fluence is defined via power law [44, 46]. The shape of this ensemble depends on the power parameter p, which provides a curvature flexibility. In the earlier works [44, 46], the parameter p was varied within the range of -1 to 0, where -1 corresponds to degenerate defect ensemble distribution and 0 corresponds to uniform distribution of the local defect damage thresholds. Later, a piecewise-defined exponential model was suggested [50], since an exponential defect density growth has been observed experimentally for low fluences [240]. In this case, the power law model is restricted to positive p. Irrespective of p value, the damage probability curve measured for a sample with power law defect ensemble features smooth bending at the threshold fluence and a strictly defined LIDT. However, the total defect density approaches infinity as the fluence increases [44], thus, it can be calculated only in a specified peak fluence interval.

Gaussian model assumes that the defect ensemble follows Gaussian distribution. In this case, T_0 corresponds to the mean LIDT value, which means that the amount of defects with LIDT T_0 on a sample surface is the highest. ΔT corresponds to the standard threshold deviation (full width at $1/\mathrm{e}^2$) (Fig. 3.1: C) [47]. However this model has a drawback – using this model, an absolute, lowest LIDT value does not exist. Only conditional LIDT can be determined for

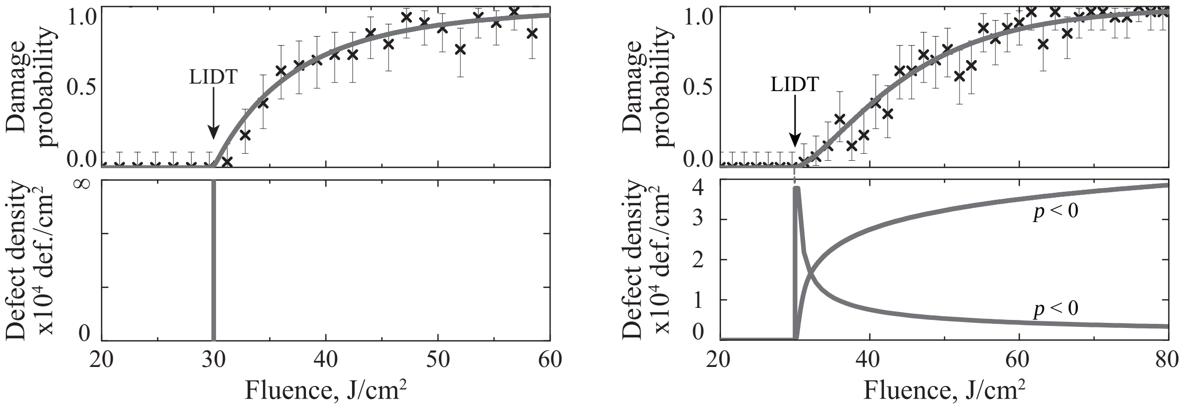

A Degenerate defect ensemble

B Power law defect ensemble

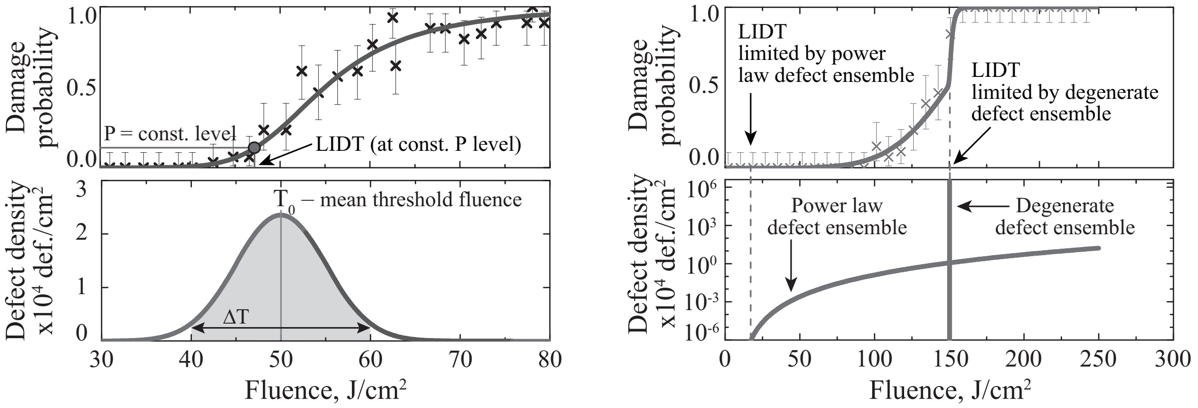

C Gaussian law defect ensemble

D Mixed defect ensemble

Figure 3.1 Top images show LID probability curve corresponding to the defect ensemble shown at the bottom. Four cases are visualized: **A** is degenerate defect ensemble, **B** is power law, **C** is Gaussian and **D** is mixed defect ensemble.

a non-zero damage probability. The damage probability curve is approaching 0, but never reaches it, thus the LIDT has to be determined on a specific damage probability. It is recommended to report LIDTs at 0.001 damage probability level [47].

Mixed defect ensemble is described with composite models, where different aforementioned defect ensembles are combined (Fig. 3.1: D) [45, 48, 49]. Usually, the damage probability curves are complex: different curve parts are related to different defect ensembles. In this case, LIDT can be determined by applying a complex model or by approximating only a part of the probability curve. In practice, interpreting such an ensemble depends on the operator's experience and insight.

A variety of functions used to predict the defect ensemble helps one to understand the nature of extrinsic contamination by defects. However the lack of *a priori* information about the true defect ensemble complicates the standardization of LIDT measurements. As mentioned above, some functions, namely, the Gaussian, do not feature a clearly defined parameter that could be directly linked to the highest fluence with zero damage probability [47, 230]. The lack of information regarding the true defect ensemble and appropriate criteria of damage threshold leads to compromises such as the wide use of the linear fit function. Furthermore, the reliability of statistical models requires sufficient sets of experimental data. This condition is hard to ensure when the sample sizes are very limited. Aforementioned factors raise the need of direct and unambiguous defect ensemble determination method. Raster scan procedure shows promising results as a reliable defect density characterization technique [227, 229]. However, it is not yet fully standardized. As there are no basic recommendations, that leaves a possibility for systematic errors to occur. Thus, in the Sections below, the main principles of raster scan procedure application for quantitative evaluation of damage precursors are described.

3.2 Experimental methodology

In order to assess the true distributions of defect ensembles, a direct comparison of two methods, i.e. raster scan and damage probability measurements, has been performed for the first time. Firstly, the defect ensemble is extracted from high-resolution damage probability measurements performed using 1-on-1 ISO 21254-1 test procedure [9]. Secondly, on the same set of samples, the defect ensemble is determined by the damage density measurements based on raster scan procedure. Postmortem defect inspection was carried out by bright field, Nomarski and atomic force microscopy (AFM). Defect ensembles extracted by the two approaches are directly compared and discussed.

3.2.1 Preparation and characterization of samples

Fused silica is known to feature a better UV transmission than other glasses. Thus, it is one of the main materials used to produce optical elements for the UV spectral range. Measurements have been carried out on two types of samples: uncoated fused silica substrate (FS) and fused silica substrate with a deposited SiO_2 monolayer film (FS + SiO_2). All substrates were identical – 5 mm thickness, conventionally pad polished, prepared within the same polishing batch. Monolayer films are fabricated by ion-beam sputtering (IBS) technology. The physical thickness of SiO_2 layer is 361 nm. Produced coating features a refractive index of 1.492 at 355 nm wavelength. Additionally, both samples are *ex situ* annealed for 1 hour under a maximum temperature of 300 °C.

3.2.2 Experimental set-up

The automated in-house build LIDT test bench presented in Chapter 1 was equipped with an optical arm used for the raster scan measurements and 1-on-1 LIDT testing (Fig. 3.2: arm B). In the case of damage probability measurement, the laser radiation is focused by a plano-convex lens down to 30 μm at $1/e^2$ level of maximal intensity in the focal plane. Small beam diameter is used to ensure a wide transition zone between 0 and 1 damage probability, since the information about defect ensemble is extracted exactly from this range [45]. In the case of raster scan measurement, the laser radiation is guided towards a galvo scanner featuring a telecentric lens and a fixed sample holder (Fig. 3.2: arm A). The focal length of the telecentric lens is 150 mm. The beam diameter at the focal plane is 18 μm at $1/\mathrm{e}^2$ level of maximal intensity. Beams are shot with 80% overlap.

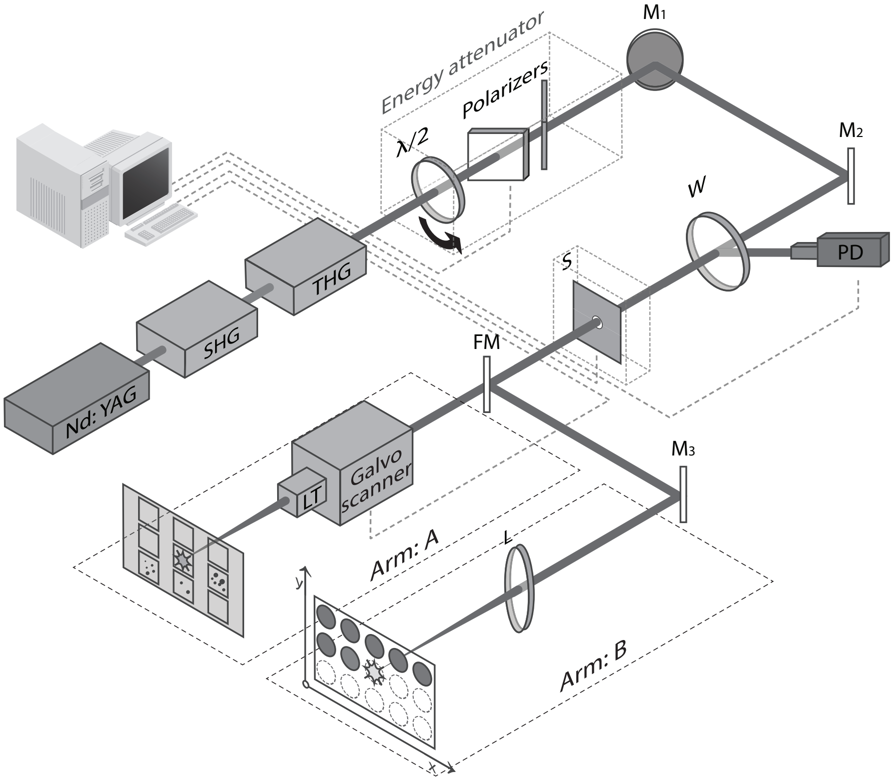

Figure 3.2 The schematics of experimental set-up. SHG is unit for second harmonic generation, THG is unit for third harmonic generation, $\lambda/2$ is a half-wave plate, M1, M2, M3 are steering mirrors, W is a wedge, PD is a photodiode, S is a mechanical shutter, FM is a flipping mirror, LT is a telecentric focusing lens, L is a focusing lens.

Postmortem inspection of all irradiated sites is performed. Irradiated site is declared as damaged if any visible modifications are seen with a Nomarski microscope. Nomarski microscopy is a common choice for the off-line damage detection in damage probability measurements, since it ensures a better contrast than bright field microscopy. However, in this particular case, no differences were found between Nomarski and bright field microscopies. The inspection was performed with Olympus BX51 microscope using 40× magnification with 0.6 numerical aperture (NA). The limit of the lowest defect density that can be observed without image stitching by an optical microscope is defined by the field of view (FOV) and at least one observed defect. In this case, it was found to result in a detectable density of 2713 defects/cm^2. Additionally, samples tested with raster scan procedure were inspected with a Dimension Edge atomic force microscope system from *Veeco*. Scanning was performed in tapping mode, over a 50×50 μm^2 scan area. The probe used for AFM was an aluminum and diamond-like-carbon coated silicon probe of <5 nm tip radius. In this case, the lowest detectable defect density was 40 000 defects/cm^2. Data obtained from AFM measurements were analyzed with the software package *"Nanoscope Analysis v1.40"*.

3.2.3 Raster scan procedure

Raster scan procedure is used to determine damage density dependence on peak laser fluence. Since in nanosecond pulse regime a laser damage event is mainly associated with the presence of nanometer sized defects, the damage density might be directly linked to the defect density. In the context of this study, defects are visually seen as craters that formed when the defects were exposed to the peak laser fluence higher than defect damage threshold (Fig. 3.3: A).

Damage density measurements are carried out in the following steps. Firstly, the surface of an optical sample is virtually divided into domains which are to be exposed to predetermined peak fluence (Fig. 3.3: B). Each domain consists of a hexagonal matrix of testing sites. In order to ensure a uniform intensity over the whole tested area, shot-to-shot laser beams are overlapped. The overlap is one of the key parameters of this procedure. On one hand, if the overlap is high, defects experience a long irradiation ramp and damage grows due to successive shots on the same site, but on the other hand, high overlap is neces-

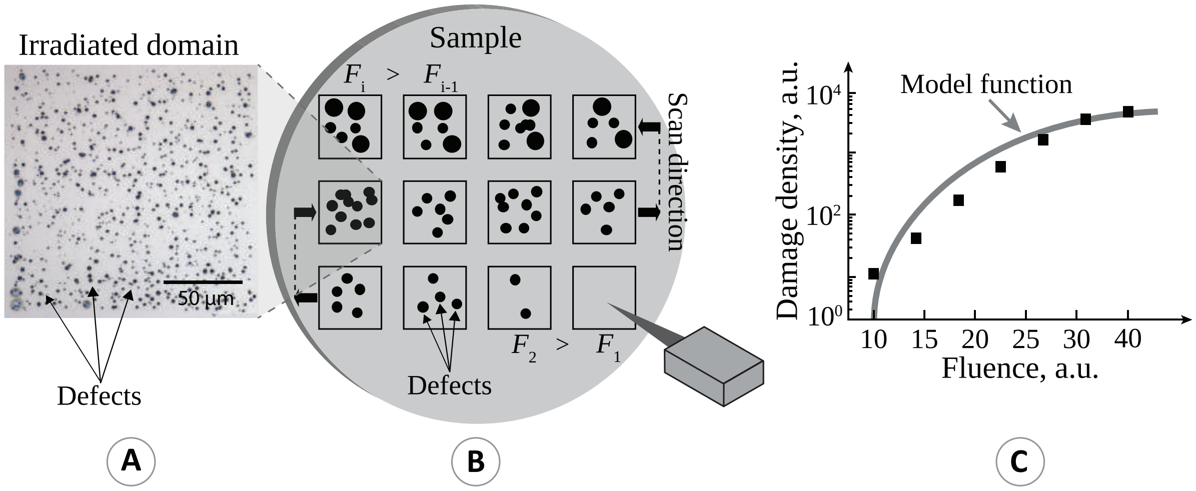

Figure 3.3 The basics of raster scan procedure. **A**: defects seen as craters that formed when the defects were exposed to the peak laser fluence higher than defect damage threshold. **B**: test sample divided into domains exposed to the constant peak laser fluence F_i with 80% overlapping laser beam. **C**: an example of experimental result of raster scan procedure. Damage densities estimated from microscopic images are plotted versus the applied laser peak fluence.

sary to ensure a good correspondence between damage and fluence maps. A parametric study on laser-induced surface damage density measurements concluded, that beam overlap above 95% results in a catastrophic damage growth. Also, observed damage morphologies can no longer be related with individual damage precursors [227]. Recorded damage densities with an overlap between 31% to 95% match within the interval of uncertainty. After dividing the sample, the first domain is exposed to laser pulses with a constant onset peak fluence F_p. Then, fluence is changed (either increased or decreased) by a small increment step (Fig. 3.3: B) and next domain is irradiated. Following this algorithm, the scanning procedure is carried out on all domains under various fluences of interest. After the measurement, an optical image of each domain is recorded by bright field or Nomarski microscopy (Fig. 3.3: A).

Images of each irradiated domain (Fig. 3.4: A) are used to evaluate the number of defects $N(F_\mathrm{p})$, which were converted to visible craters at particular peak fluence. Only the central area of a recorded image is used for defect density calculation. Firstly, each recorded optical image is duplicated. Then, the duplicated copy is used to generate a smoothed background image – a median filter is applied to remove all visible particles (Fig. 3.4: B). The original image is divided pixel by pixel by the smoothed background, resulting in an image with a uniformly levelled background (Fig. 3.4: C). The number of defects in the image is calculated by particle counting algorithm based on a grey level threshold for a particle to be separated from the surrounding noise (Fig. 3.4: D). The calculation is performed using open source software *ImageJ* [241]. The same threshold value is used for all images.

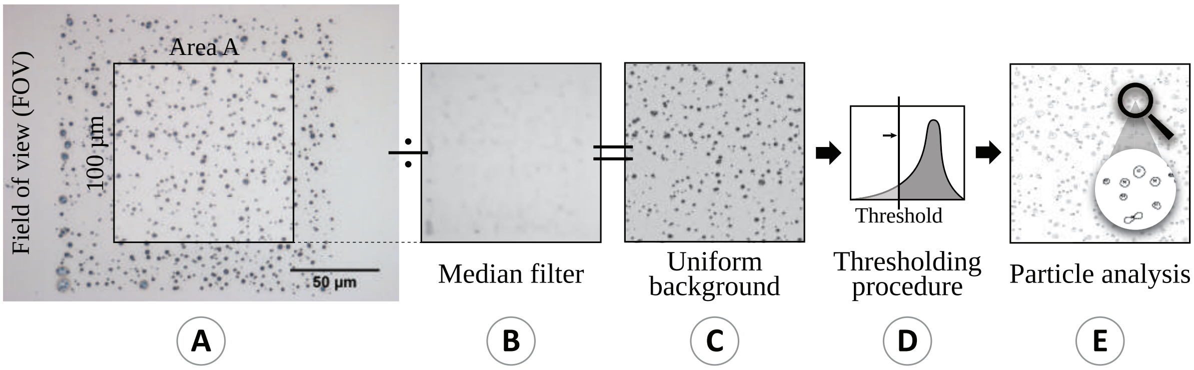

Figure 3.4 **A:** a typical image recorded after raster scan procedure. **B:** a median filter generated to discard visible particles. **C:** an image after the background subtraction. **D:** the thresholding procedure. **E:** particles calculated from an image by particle analysis algorithm.

Experimental defect density $m(F_\mathrm{p})$ is estimated and plotted as a ratio of $N(F_\mathrm{p})$ defects and area A (Fig. 3.4: A) exposed while testing one irradiated domain, both calculated from optical microscopy.

$$m(F_\mathrm{p}) = \frac{N(F_\mathrm{p})}{A}\,. \tag{3.1}$$

Defect density calculated from each optical image is plotted versus respective applied peak fluence (Fig. 3.3: C). Typical defect density dependence is shown in logarithmic scale. Defect density data are fitted arbitrarily. A power law dependence on laser peak fluence is most commonly reported [227, 242].

In some cases, damage density curve additionally features a "plateau" at low fluences [186, 227, 229].

As the beam overlap used in raster scan procedure is not perfect, a large fraction of exposed area is irradiated with a local fluence smaller than the peak fluence. This fact causes differences between the experimentally observed defect density $m(F_\mathrm{p})$ and the true defect density. Therefore, the experimental defect density dependence on the peak laser fluence should be corrected for real localized fluence. There are several techniques that approach this question [243–245]. A detailed description of commonly used data treatment method [148, 227, 229] is presented in the work of L. Lamaignere et al. [229]. Even though the approach proposed therein works well, it involves a complex fitting procedure, which requires the data recorded at high fluences to be treated differently than the data obtained for low fluences. Furthermore, the pulse-to-pulse spatial beam profile variation is not taken into account. And, most importantly, to our best knowledge, the defect density measurements have never been related nor compared with defect ensembles extracted from damage probability measurements. To address those issues, we propose a revised approach based on experimental data fitting by modelling the defect density curve with an assumed defect ensemble. Total laser instability is assessed via careful characterization of the laser fluence distribution prior to the measurement. Thus, unlike in the other cases [186, 229], simulated (not experimental) damage density is corrected for pulse-to-pulse fluence instability.

The actual spatial laser fluence distribution used to irradiate a sample is determined by individual spatial beam profiles, recorded for each irradiation site of a domain. Each laser pulse varies in beam shape and absolute energy value, causing the intensity variations recorded within every spatial profile image. After determining the distributions of all the images representing separate laser shots, they are combined into a single image, consisting of maximal intensity pixels of all images (Fig. 3.5: A). Only the central part of the combined image is

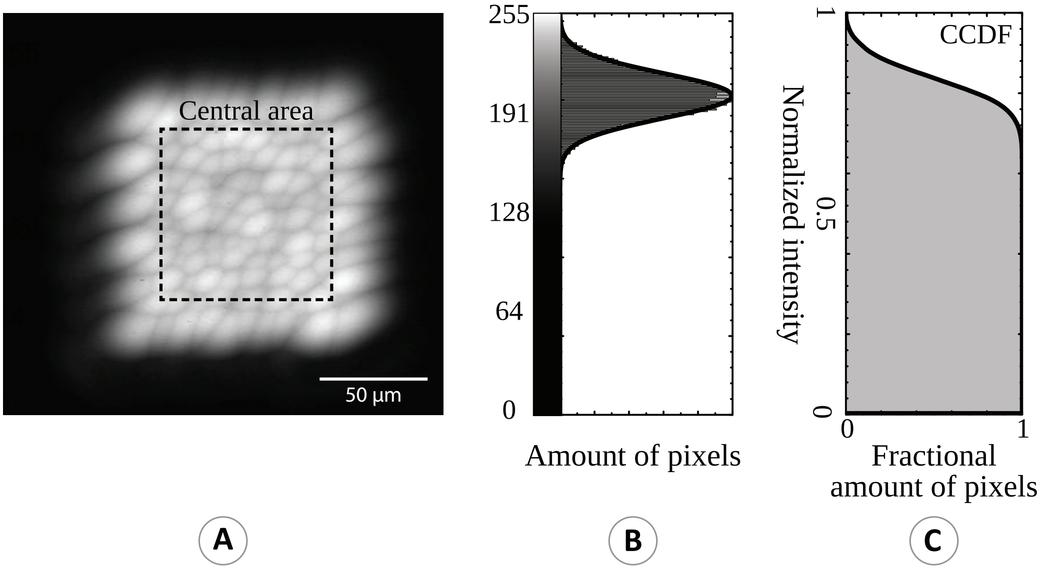

Figure 3.5 **A:** a combined image synthesized out of individual spatial beam profiles recorded for each site, for each site of a domain, equivalent to domains used in measurements, and for one typical spatial pulse profile used in raster scan measurements. **B:** a histogram of pixel grey level distribution. **C:** integrated and normalized histogram used as the PDF of intensity.

selected for further investigation in order to avoid edge effects. The combined image is used to extract a histogram distribution of the maximal pixel grey levels. Grey level axis (Fig. 3.5: B) is scaled to the highest pixel value, representing the peak laser fluence. The integrated area under this curve is normalized to unity. Then the extracted distribution can be used as an empirical PDF of the onset fluence (Fig. 3.5: B), which defines the range of localized fluence values that are used to irradiate the sample with a defined F_p. Integration of the PDF results in a cumulative distribution function (CDF), which describes the probability of irradiation of a randomly distributed particle with a localized fluence less than or equal to a selected fluence of interest F, that is below F_p. However, here we want to solve an opposite case and seek to know how often F is exceeding the localized fluence of interest, as F_p is defined. Namely, what fraction of raster scanned area damages the defects at specific onset laser fluence. Mathematically it can be evaluated by a complementary cumulative distribution function (CCDF), also known as a tail distribution or exceedance (Fig. 3.5: C):

$$\mathrm{CCDF}(F_\mathrm{p}) = 1 - \mathrm{CDF}(F_\mathrm{p})\,. \tag{3.2}$$

The CCDF is determined for each peak fluence used in measurements. For this purpose, F_p is used as a scaling factor of the grey level axis. Then the obtained function is numerically interpolated over the whole range of tested fluences. The shape of the CCDF depends on the overlap of individual pulses and thus on the histogram of the pixel grey level distribution (Fig. 3.5: B).

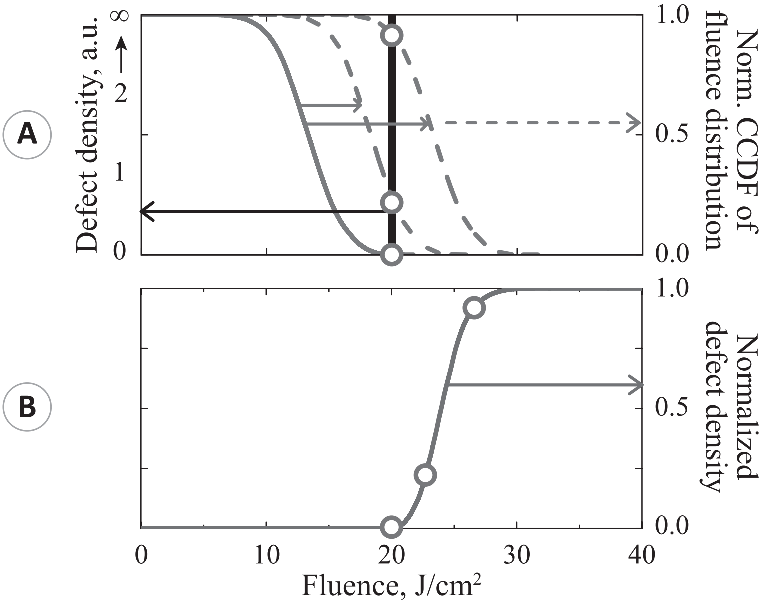

Figure 3.6 An example of numerical simulation. **A:** an illustration of the degenerate defect ensemble convolution with a normalized CCDF of local fluence F distribution. **B:** the simulated curve of raster scanned defect particle density as a function of peak fluence.

Experimentally measured damage density $m(F_\mathrm{p})$ is a convolution between the true defect ensemble $D(F)$, that we are trying to extract, and the local fluence distribution characterized by the CCDF. Thus, in presented model, the simulated experimental damage density $m^*(F_\mathrm{p})$ is defined as:

$$m^*(F_\mathrm{p}) = \int_0^{F_\mathrm{p}} \mathrm{CCDF}(F_\mathrm{p}, F) \cdot D(F)\,\mathrm{d}F\,. \tag{3.3}$$

The fitting of the experimental damage density $m(F_\mathrm{p})$ with the simulated damage density $m^*(F_\mathrm{p})$ is performed by varying the parameters of the defect ensemble until the best agreement with experimental data is achieved.

An example of the application of the model is given in Fig. 3.6. The degenerate defect ensemble model is assumed to exemplify the situation. It is shown, that due to the localized fluence distribution the measured defect density is a function of F_p as defined by equation 3.3.

3.3 Results and discussion

3.3.1 Comparison of defect ensembles

Results obtained from 1-on-1 LIDT testing and raster scan measurements are shown in Figs. 3.7 and 3.8 respectively. Both techniques show the same trend: FS + SiO_2 data are shifted towards lower fluence if compared to FS (Fig. 3.7: A and Fig. 3.8: A).

In the case of raster scan measurement, the uncertainty interval is determined by two limiting cases. The upper limit is defined when the threshold of the camera noise is reached and an undamaged region is (mistakenly) considered as particles. The lower limit is set when clearly visible particles are neglected. The lowest detectable defect density is limited by the FOV of bright field microscopy (3.8: L1). Since the true defect ensemble is unknown, three statistical defect ensembles (degenerate [44], power law [44], Gaussian [47]) have been assumed in order to fit the experimental results in both cases. It is worth mentioning that raster scan data range used for fitting is restricted with a contamination limit, which is discussed in detail further in this Chapter. The suitability of the fitting models is judged by their ability to reproduce the shape of experimental data. In the case of damage probability measurements,

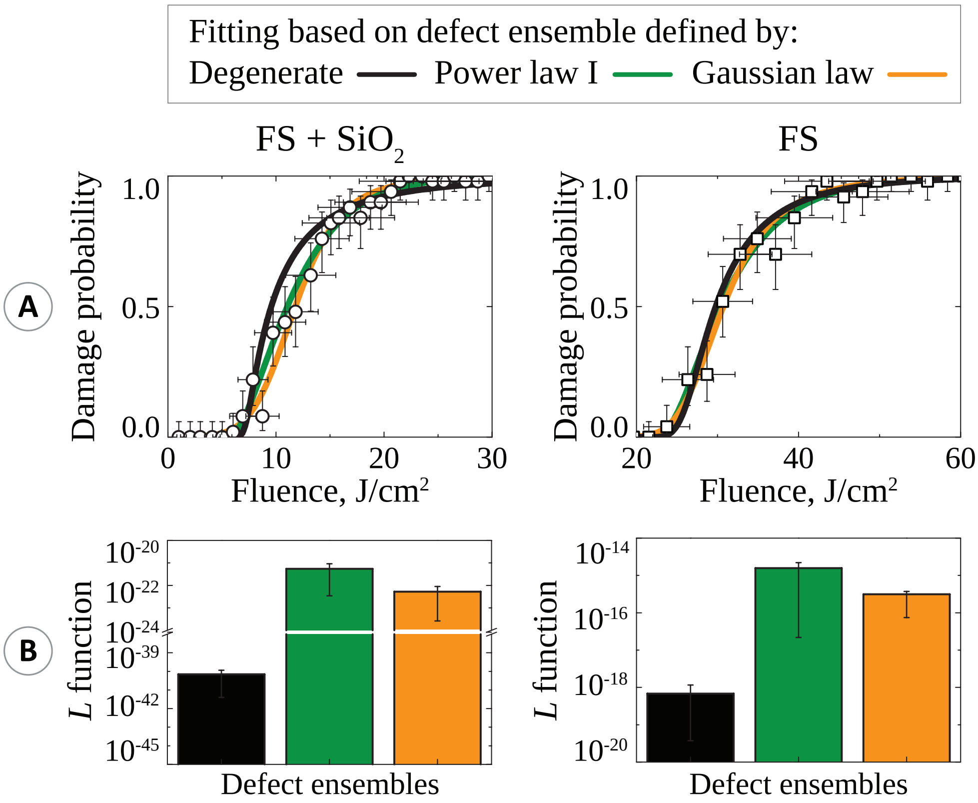

Figure 3.7 **A**: 1-on-1 damage probability curves measured for FS and FS + SiO_2 samples and fitted using different defect ensemble models. **B**: absolute likelihood values of each fit.

the experimental data were fitted with nonlinear damage probability model described in **Chapter 2**. The goodness of fit is evaluated by directly comparing the absolute values of the likelihood function L. The higher the likelihood value, the better the fit. The degenerate defect ensemble features the lowest value of the likelihood function for both samples (Fig. 3.7: B). In contrast to the degenerate ensemble, both the power law and Gaussian ensembles are able to reproduce the experimental data and are almost indistinguishable one from another. Thus, at given experimental conditions, the damage probability method can hardly be used to determine the true defect ensemble model. In the case of the raster scan measurements, the experimental data were fitted by applying a nonlinear regression. The goodness of fit is judged by the mean squared error (MSE). The fitting was performed in a logarithmic scale in order to weight the

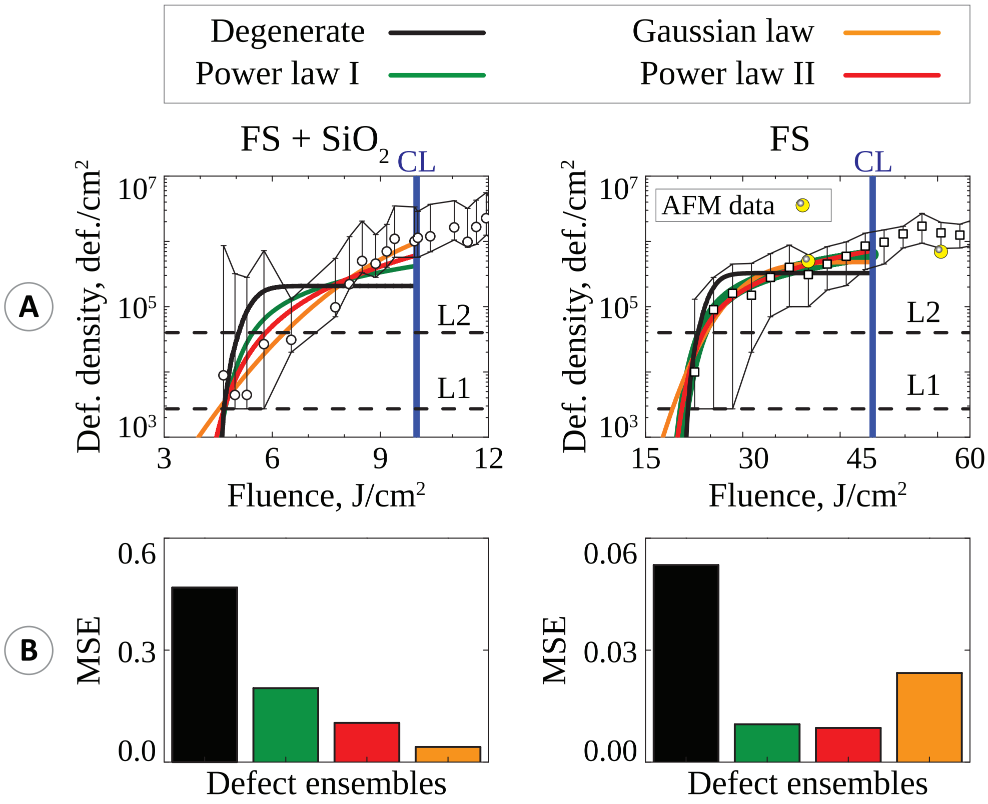

Figure 3.8 **A**: raster scan damage probability curves measured for FS and FS + SiO$_2$ samples and fitted using different defect ensemble models. L1 and L2 mark the lowest detectable damage densities from different microscopes. CL marks the contamination limit. AFM data points are indicated to validate the data obtained by optical microscopy. Both CL and AFM data are discussed in the Subsection 3.3.2. **B**: MSE values of each fit.

data points recorded at low and high absolute damage densities.

$$\mathrm{MSE} = \frac{1}{n}\sum_{i=0}^{n-1}\left[\log\left(m^*(F_\mathrm{p})\right) - \log\left(m(F_\mathrm{p})\right)\right]^2 . \tag{3.4}$$

If the MSE is approaching 0, it means that the applied model is able to reproduce the recorded experimental data. Thus, the closer MSE is to 0, the better. Comparison of fits reveals that data obtained by raster scan measurements can also be well fitted by several defect ensembles, namely, power law and Gaussian. Thus, based on these results, the true defect ensemble cannot be unambiguously defined as well.

Distributions of laser damage precursors extracted by the damage probability measurements and the raster scan procedure are shown in Fig. 3.9. They are indicated by black and red lines, respectively. There are several issues with used defect ensemble models that should be discussed before we start to interpret the presented results. Firstly, as it has been mentioned in Section 3.1, the determined LIDT value depends on external factors: beam diameter and selected damage probability level. Thus, the criteria for the LIDT definition differ among the defect ensembles. In order to compare the results, an alternative LIDT definition is suggested. The LIDT is related directly with the width of a Gaussian defect ensemble:

$$\mathrm{LIDT} = T_0 - 3 \cdot \Delta T\,, \tag{3.5}$$

where T_0 is the central position of Gauss function, ΔT corresponds to the standard deviation of Gauss function (Fig. 3.9: D). Within the range of 3 standard deviations lie 99.7% of the distribution data. The introduced factor of 3 is selected arbitrarily and therefore is subject for further discussions.

Furthermore, considering the power law ensemble, two cases were investigated. Firstly, parameter p was set between -1 and 1. This approach is identified as “power law I”. Secondly, parameter p was restricted to the range from -1 to 0 as introduced in Refs. [44, 46]. This approach is identified as “power law II”. Both approaches were used to fit the results obtained from the damage probability measurements and the raster scan procedure. The best fit of damage probability curves (Fig. 3.7: A) was with $p < 0$. The same result was achieved by applying both the “power law I” and “power law II” approaches (Fig. 3.9: B and C, black line). Such ensembles have a well-defined threshold fluence value and predict that the defect density decreases for higher fluences. In the case of the raster scan measurements, the best agreement with experimental

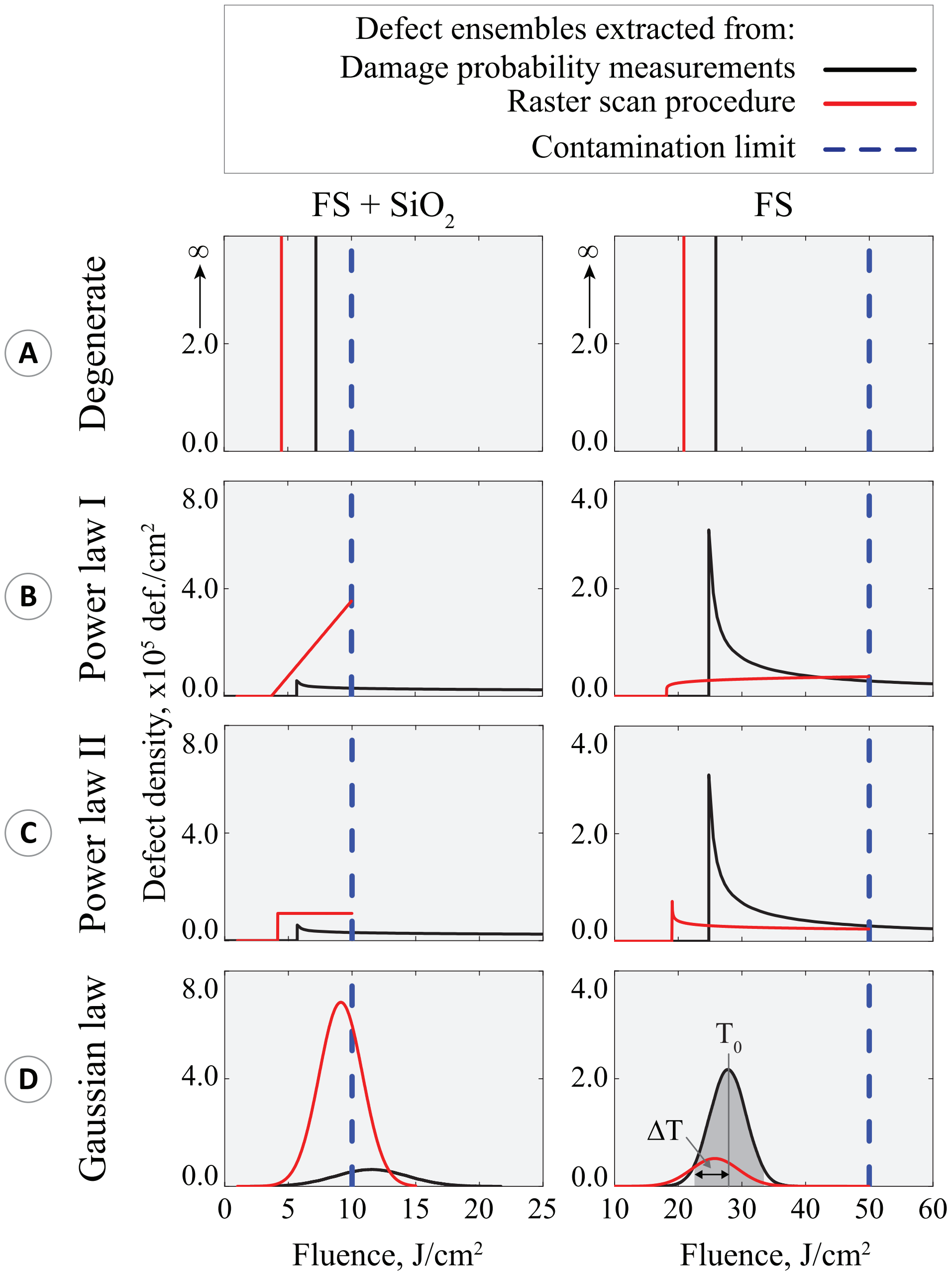

Figure 3.9 The defect ensembles extracted from damage probability measurements (black) and the raster scan procedure (red). Defect ensembles, **A** to **D**, are: degenerate, power law I, power law II and Gaussian. T_0 is the central position of Gauss function, ΔT is the standard deviation of Gauss function.

results was found using the "power law I" with $p > 0$. The determined defect ensemble has a well-defined LIDT value and predicts the growth of defects for higher fluences (Fig. 3.9: B, red line). When the damage density data were fitted using the "power law II" approach, the best agreement with experiment was achieved when p was equal to 0, which corresponds to the uniform distribution (Fig. 3.9: C, red line). The comparison of MSE values (Fig. 3.8: B) indicates that botj power law ensembles cannot be distinguished from Gaussian ensemble. Since the obtained data are conflicting, none of the extracted defect ensembles can be concluded as the true defect ensemble yet. This is a major issue, because the use of inappropriate defect ensemble, as well as non-eligible damage threshold criteria, causes over- or underestimation of both the absolute LIDT value (Fig. 3.10) and the areal defect densities (Fig. 3.11).

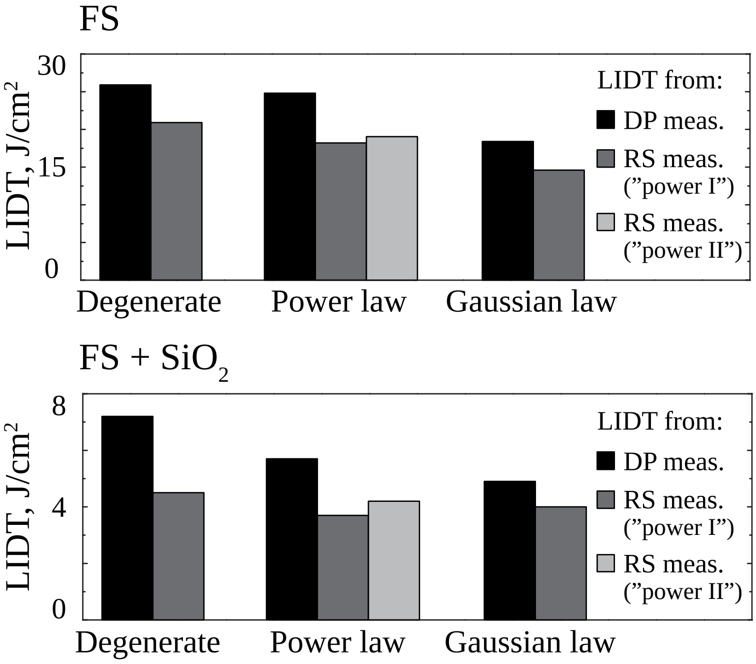

Figure 3.10 The comparison of LIDT extracted from damage probability and raster scan measurements by applying different defect ensemble models.

The defect ensembles also differ when comparing different ensemble determination methods on the same sample. For instance, the Gaussian based defect ensembles deviated in the central position and shape (Fig. 3.9: D). The decrease observed in the areal defect density extracted from the raster scan procedure

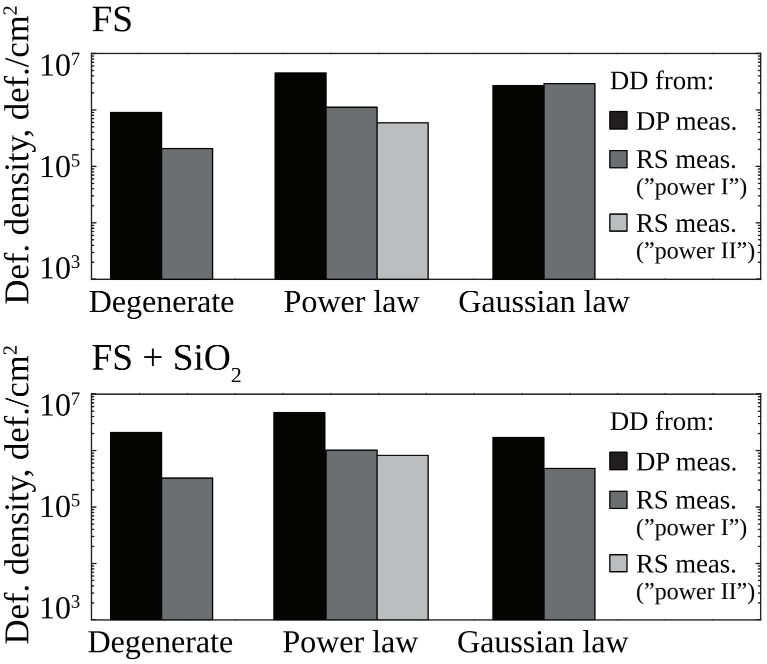

Figure 3.11 The comparison of the defect densities extracted from damage probability and raster scan measurements by applying different defect ensemble models.

can be attributed either to the conditioning effect [180] or to other effects (for example, limited resolution of optical microscopy). Conditioning of the material most likely is not a possible scenario, as it should also result in higher absolute LIDT values. However, the results show that the threshold determined by the raster scan procedure also decreases with respect to the damage probability measurements. While seeking to explain the observed differences, two hypotheses were proposed. Either none of the used defect ensemble models was correct, or some of the experimental data were biased. In the first case, there would be no significant difference between the defect ensembles determined by raster scan and damage probability measurements. So, it is clear that some of the data are biased by the applied experimental methodology.

In the case of the damage probability measurements, the determination of defect ensembles can be limited by a narrow transition range between 0 and 1 damage probability. In order to extend the transition region, usage of more sharply focused laser beams is possible. Then the number of irradiated sites should be significantly increased to keep the statistical error bar reasonably small. In the case of raster scan procedure, the experimental data can be influenced by an overexposure of the sample due to a partial overlap of the pulses as well as by contamination with ablation products. However, with the used overlap of 80% the effect of preconditioning or damage growth was assumed to be negligible [227]. But in our case the differences in extracted defect ensembles were recognizable. Thus, the contamination of a sample surface due to ablation products was also considered as a possible scenario. In order to test these hypotheses, the comparison of damage morphologies and the surface analysis by optical and atomic force microscopy is performed.

3.3.2 Analysis of damage morphologies

In the case of damage probability measurements, the aim of surface analysis is only to check whether the laser affected area is visually modified or not. In the case of raster scan measurements it is necessary to distinguish between two separate particles, thus the optical resolution becomes very important. So, two cases should be considered when analyzing raster scan measurements:

- factors causing an overestimation of defects. As discussed previously, ablation can cause the contamination of a sample. So, it should be checked whether such contamination exists and whether it influences the experimentally recorded defect density data.
- factors leading to underestimation of the defects due to inability to distinguish between two particles. Two issues should be considered here: the resolution of the microscope used and particle separation by the particle counting algorithm.

The typical laser damage induced on FS and FS + SiO_2 samples at similar peak fluences is compared in Fig. 3.12. The laser damage of FS consists of "pin-point" patterns. Such morphology is obtained for both 1-on-1 and raster scan tests. It clearly indicates the presence of localized defects, which cause the absorption of applied laser radiation by nano-size particles, digs, scratches or cracks as reported previously [29]. FS + SiO_2 sample features similar damage morphology.

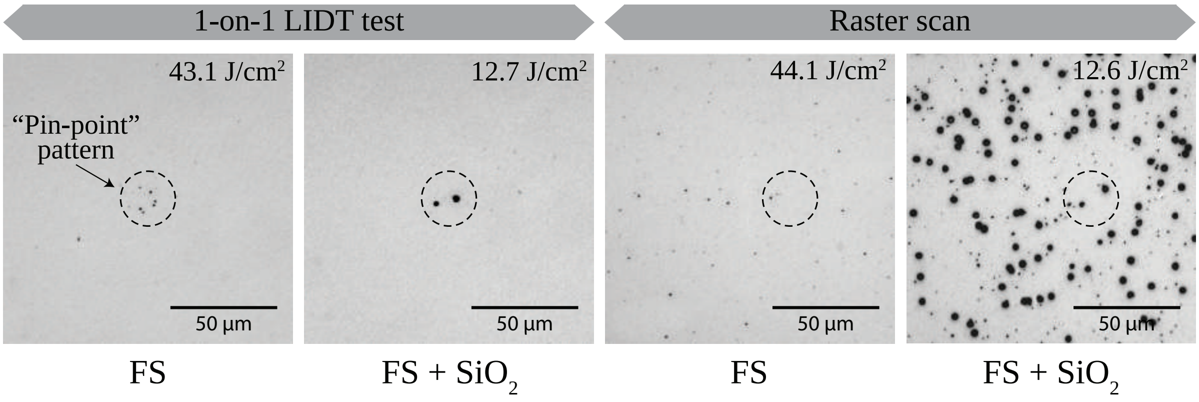

Figure 3.12 The damage morphologies recorded for FS and FS + SiO_2 by damage probability and raster scan approaches.

In order to test the presence of possible contamination, the FS sample has been cleaned after the raster scan measurement. Cleaning was performed in an ultrasonic bath for 40 minutes using a commercially available cleaning process for optical elements [246]. Comparison of the sample surface before and after the cleaning procedure revealed that a self-contamination during the measurement does exist (Fig. 3.13: A). Before cleaning, multiple particles can be observed in both marked areas. Area 1 shows particles within the irradiated zone, while area 2 shows particles visible on the non-irradiated area. Some of these particles have been removed during the cleaning. However, ablation debris and craters induced because of embedded defects cannot be distinguished by optical microscopy. Thus, ablation caused contaminants can be easily mistaken for polishing or deposition defects. The same effect was observed on FS + SiO_2 as well. In order to find out whether all contaminant particles were removed after the cleaning, the surface of the sample was inspected with AFM (Fig. 3.13:

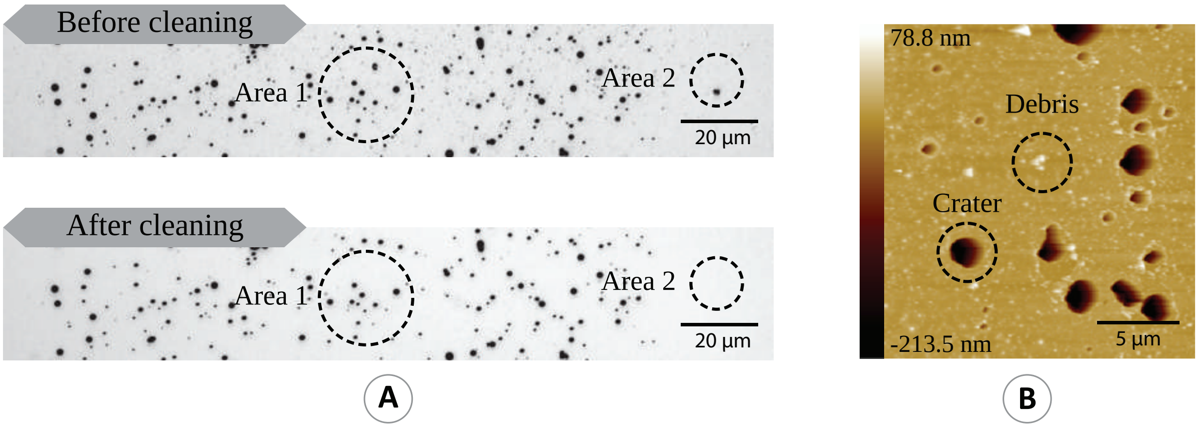

Figure 3.13 **A:** representation of self-contamination by ablation process induced on a FS sample at fluences above the contamination limit. The surface of raster scanned sample is recorded by bright field microscope before and after cleaning. **B:** surface analysis of raster scanned FS by AFM shows two types of particles: defects and debris.

B). Surface analysis reveals two types of particles existing on the sample surface: debris, most likely formed from the ablation, recognized as peaks, and defects identified as craters. Debris can't be removed by standard optics cleaning procedure and it can't be distinguished from craters by optical microscopy. The density of debris increases with laser peak fluence above damage threshold (Fig. 3.14). Contaminant particles start to occur at fluence above 50 J/cm^2 for FS sample and above 10 J/cm^2 for FS + SiO_2. Thus, the term "contamination limit" (CL) is introduced here. Contamination affected experimental data should not be included in the fitting because defect density estimated by optical microscopy in this fluence range will be overestimated (Fig. 3.8 and Fig. 3.9: CL).

Crater densities (excluding debris) have been calculated from the AFM results at two fluences, namely, below and above the contamination limit for the FS sample (Fig. 3.8: AFM data). Defect density below the contamination limit corresponds to the defect density determined by optical microscopy in the range of uncertainty. However, the defect density calculated at fluence above the contamination limit shows that in this range the data determined by optical microscopy are overestimated. Thus, the contamination affected data

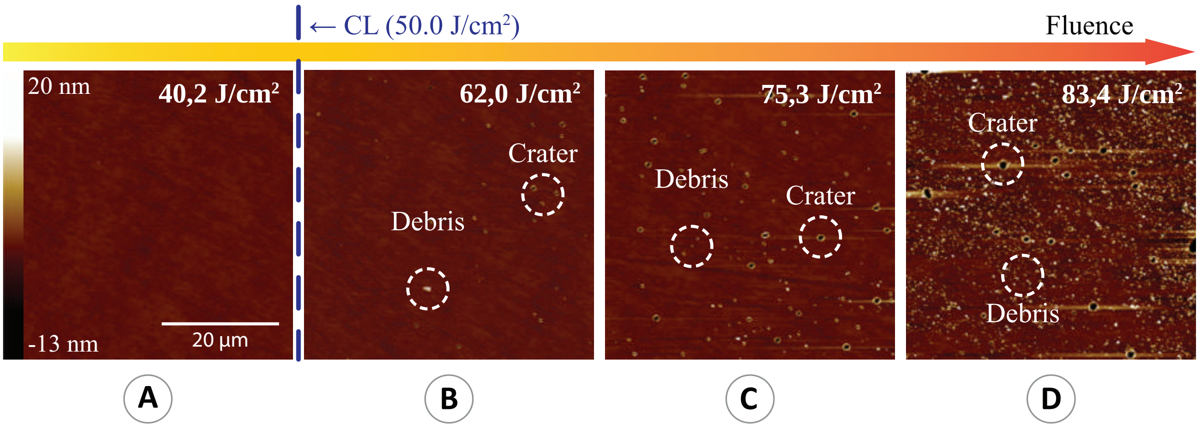

Figure 3.14 Ablation induced contamination by debris particles on FS surface. **A:** fluence is lower than the damage threshold, **B–D:** fluence above the damage threshold.

should not be included in defect density calculations. These results raise two concerns. Firstly, the debris cannot be eliminated by a standard optical element cleaning procedure. Since the contamination cannot be distinguished optically, there are two approaches that could be applied to solve this problem. On the one hand, the defect density can be determined by the AFM, which is capable of separating defects from debris, on the other hand, the contamination limit should be set and the data above it should not be used in the defect density calculation. Another concern questions the role of ablated particles in the generation of new craters. It is unknown whether the debris particles act as additional damage precursors or not. More work should be carried out in order to answer this question. A possible solution here could be the sample exposure to one laser pulse featuring a large flat-top spatial distribution. In this case, the generated defect would not be affected by repeating pulses due to the overlap procedure and previously generated ablation products would not influence the creation of new ones.

In order to avoid the underestimation of defect density, the limit of the lowest detectable damage density should be defined. It varies with the field of view of the applied microscopy. There are no detectable data below these limits. It could be easily overcome by stitching separate images. At this point, it

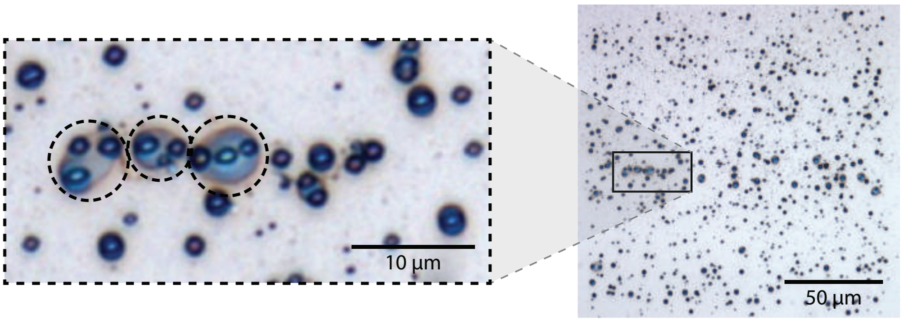

Figure 3.15 An example of clusterization of particles in FS sample, exposed to fluence much higher than the damage threshold.

is noticed that no observed damage within an image does not mean that the defects do not exist. Another factor that causes the underestimation in data recorded by the raster scan procedure is related to the possible clustering of particles (Fig. 3.15). Multiple particles cannot be distinguished by thresholding procedure and would be treated as one large particle. In this study, a clearly recognizable clustering process started at 57.6 J/cm^2 for FS and at 11.0 J/cm^2 for FS + SiO_2. The beginning of the clustering process was observed at similar fluences as the contamination limits discussed above. Inability to determine precise defect density for high fluences might explain a decrease in the defect density growth witnessed in the damage density measurements (Fig. 3.8). Thus, the application of raster scan procedure requires a consideration of aforementioned effects as well as a detailed description of the applied particle calculation techniques in order to compare the data from different laboratories and to avoid misconceptions in presented results.

3.4 Conclusions

For the first time, a direct comparison of laser fluence limiting defect ensembles extracted from damage probability and raster scan measurements is performed. We have shown that both approaches are incapable of telling which of defect ensembles – power law or Gaussian is the true one, while it is clear that degenerate ensemble does not suit as the true defect ensemble. Most likely, extracted defect ensembles do not match due to experimental limitations of the raster scan procedure. It has been shown that due to laser ablation process the samples become contaminated by small particles – debris, which cannot be distinguished by optical microscopy and some of them cannot be removed by standard optical element cleaning procedures in an ultrasonic bath. Threshold fluence of the permanent contamination process has been determined for each sample. It remains unknown whether the debris particles act as additional damage precursors. In addition, we have also shown that the experimentally collected data of the raster scan procedure can be influenced by particle clustering when several particles cannot be distinguished by particle calculation algorithm. The threshold fluences for particle clustering processes have been found to similar with the contamination limits.

4 Identifying the weak layers in optical component

A chain is only as strong as its weakest link.
An international adage.

Material related to this chapter is published in *A2, A9, C2*

None of the previously discussed defect identification and characterization techniques is able to identify weak sublayers within a multilayer coating, where damage was initiated, or answer the question which type of defects – coating or polishing – limit the optical resistance of the component. Thus, the goal of this study is to develop a new metrological approach capable of identifying the layers containing defects with the lowest LIDT in complex multilayer optical components. In other words, it is important to identify not only how strong the weakest layer is, but which type of layer it is as well. Both theoretical and experimental efforts are made in order to distinguish polishing and deposition defects by analyzing the damage probability curves. Since both types of defects are located at a distinct depth, it is possible to manipulate the relative electric field (e-field) distribution inside the component and measure the damage probability response as a function of incident fluence at the same time. Changing the angle of incidence (AOI) and polarization allows one to form such an e-field distribution, which destructively interacts only with a particular sublayer of the coating or substrate defects. In order to test this concept, a high resolution 1-on-1 LIDT testing [9] has been carried out under UV irradiation (355 nm, 4.8 ns) for 0° and 45° AOI and varying polarizations (s, p) on four types of samples. For interpretation of the obtained LIDT data, two different approaches were applied from previous studies [28–30, 52]. On the one hand, the LIDT is related to the standing wave (SW) pattern formed within the optical element. Namely, LIDT relationship with the maximum internal field squared $|E|^2$ is analyzed [247, 248]. On the other hand, LIDT might also be associated with the properties of the traveling wave (TW). If the optical surface or the bulk has a high density of absorbing defects, then the energy of forward TW might be absorbed. In this case, LIDT depends on the internal fluence "seen" by the localized defects. Up to now it is not fully understood, which physical characteristic is associated with the scaling of LIDT when changing the AOI and polarization. Thus, both assumptions are investigated within this study.

4.1 Relation between incident laser fluence and internal LIDT

Electromagnetic waves incident on dielectric surfaces are partially reflected, absorbed and transmitted. Multiple reflections arise from the interfaces of thin films, thus the interference effects should also be taken into account. As it is still not entirely understood which physical characteristic of laser beam is responsible for scaling of the LIDT when changing the AOI and polarization, we consider two bibliographic inputs [63, 248]. Both hypotheses have been tested when interpreting the experimental data. The first assumption states that the internal damage threshold [63] is achieved as soon as critical squared internal electric field $|E|^2$ is reached at a given pulse duration. We define it as "Approach A". Another hypothesis (or "Approach B") presumes that the damage threshold is reached for critical transmitted (absorbed) laser fluence (for example, seen by an individual defect). Both approaches are quite similar, however they result in different LIDT scaling laws for AOI and polarization. These assumptions are discussed in detail below.

Approach A. For practical reasons, the ISO norm [9] considers damage threshold in terms of peak incident laser fluence F_p:

$$F_\mathrm{p} = \frac{2E_\mathrm{p}}{\pi\omega^{c}{}_{0,\mathrm{eff}}}\,, \tag{4.1}$$

where E_p is laser pulse energy, $\omega_{0,\mathrm{eff}}$ is effective laser beam radius at $1/\mathrm{e}^2$ level of fluence. Thus, the peak incident laser fluence F_p can be related to the internal electric field via incident energy density ED_inc reached within laser pulse.

On the one hand, ED_inc is characterized by the incident laser pulse energy E_p stored within a volume V, defined by pulse duration t, speed of light c and effective laser beam radius at $1/\mathrm{e}^2$ level of fluence $\omega_{0,\mathrm{eff}}$ (Fig. 4.1):

$$\mathrm{ED}_\mathrm{inc} = \frac{\text{energy}}{\text{volume}} = \frac{E_\mathrm{p}}{\pi{\omega_{0,\mathrm{eff}}}^2 ct}\,. \tag{4.2}$$

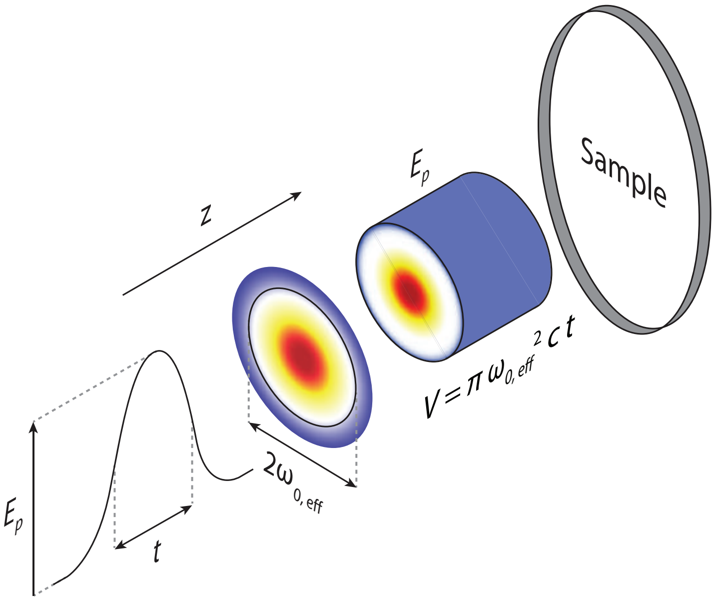

Figure 4.1 A visualization of ED_inc calculation. E_p is laser pulse energy, t is pulse duration at FWHM, $\omega_{0,\mathrm{eff}}$ is effective beam radius at $1/\mathrm{e}^2$ level of fluence, z is beam propagation direction.

On the other hand, the energy within a laser pulse is carried by electromagnetic waves as they travel through empty space. Both the electric and magnetic fields play a role in the transport of energy. Thus, the total energy density of electromagnetic wave per unit volume might be expressed as:

$$\mathrm{ED_{inc}} = \frac{1}{2}\varepsilon_0 E^2 + \frac{1}{2}\mu_0 B^2 = \varepsilon_0 E^2 \,, \tag{4.3}$$

where $\frac{1}{2}\varepsilon_0 E^2$ is the electric field energy per unit volume and $\frac{1}{2}\mu_0 B^2$ is magnetic field energy per unit volume. Further, Eq. 4.3 is simplified, since the electric field can be related to the magnetic field through $B = \frac{E}{c}$ and $c = 1/\sqrt{\mu_0\varepsilon_0}$.

Electric field contains electrical energy with the energy density proportional to the square of the field magnitude, defined as $|E|^2$. Based on Eqs. 4.1 and 4.2, the peak laser fluence, incident on the sample surface, might be readily associated with the squared magnitude of the incident electric field before it enters the sample. It can be done in four logical steps:

$$F_\mathrm{p} \propto E_\mathrm{p} \propto \mathrm{ED_{inc}} \propto |E|^2 \,. \tag{4.4}$$

When an incident laser pulse enters an optical element, it forms a SW pattern that is a function of the coordinate along the field propagation axis z and the refractive index of the material n. However, if normalized to incident energy density and internal energy density of SW pattern, the absolute $\mathrm{ED_{abs}}(z)$ inside the sample can be expressed as follows [248]:

$$\mathrm{ED_{abs}}(z) = n \left| \frac{E(z)}{E} \right|^2 \mathrm{ED_{inc}} \,, \tag{4.5}$$

where$\mathrm{ED_{inc}}$ is a peak energy density of an incident laser pulse, $\mathrm{ED_{abs}}(z)$ is a peak energy density within an optical element, $|E|^2$ is a magnitude of the incident e-field, $|E(z)|^2$ is a magnitude of the e-field inside the optical element, n is a refractive index of dielectric medium. If Eq. 4.5 is normalized to the incident laser radiation ($\mathrm{ED}_{\mathrm{inc}} = 1$), then it can be simplified and the relative $\mathrm{ED}(z)$ inside the optical element will be characterized as

$$\mathrm{ED}(z) = n \left| \frac{E(z)}{E} \right|^2 . \tag{4.6}$$

Respectively, $|E(z)|^2$ is proportional to $\mathrm{ED}_{\mathrm{inc}}$ and F_{p}. Further within this study, $|E(z)|^2$ is interpreted in terms of the relative maximal internal e-field magnitude, unless indicated otherwise. The energy within the standing electromagnetic waves fluctuates back and forth between the points and there is no net flow, even if the existing energy density is not equal to zero. Thus, the localized energy amount inside the optical elements can be reasonably assumed as a scaling factor for the LIDT.

Approach B. In this case, the total energy transmitted trough the "weakest" plane within the component is considered as a scaling factor. Thus, the LIDT scaling with AOI and polarization is expected to be proportional to the maximal transmitted fluence F_{internal} in the plane of interest (in this example, the glass interface is below the deposited coating). It should be proportional to the energy amount absorbed by localized point defects. When the sample is exposed at other than normal incidence angle, then the transmitted fluence should be scaled according to the increase of the effective area on the plane of the sample surface [9] and to the coefficient of transmission:

$$F_{\mathrm{internal}} = F_p \cdot T(\mathrm{AOI}, \mathrm{pol}) \cdot \cos(\mathrm{AOI}) , \tag{4.7}$$

where F_p is the laser peak fluence on the sample surface at normal incidence, $T(\mathrm{AOI}, \mathrm{pol})$ is a calculated Fresnel transmittance of the sample at particular AOI and polarization [249]. As fluence is associated with the net energy flow of the TWs, this approach cannot be directly applied to the analysis of SW patterns.

Approach B is limited to planar models of defect ensemble distribution, because the fluence is defined per effective area on the sample surface.

4.1.1 Modeling the damage probability

A theoretical model was built to predict the behaviour of damage probability curves, when changing AOI and polarization. The presence of point defects, which initiate damage at a particular fluence, is assumed to exist within optical elements. Defects are virtually distributed in different sites of the sample: within the bulk of the single layer coating, at the polished substrate interface or within distinct layers of a multilayer coating. Identification of the weakest layer requires the ability to model the damage probability of distributed defect ensembles both within an arbitrary plane inside the sample and in the bulk of the particular coating.

4.1.2 Planar damage probability model

For a Gaussian laser beam of TEM$_{00}$ mode, the fluence distribution at the plane of incidence is

$$F(r, z, \phi, \theta) = F_0(z, \theta) \exp\left(-\frac{2r^2}{\omega^2_{0,\text{eff}}(\phi, \theta)}\right), \tag{4.8}$$

where r is distance from the laser beam center, $\omega_{0,\text{eff}}(\phi, \theta)$ is an effective beam radius at $1/\text{e}^2$ fluence level. When the AOI is oblique, $\omega_{0,\text{eff}}(\phi, \theta)$ can be described in polar coordinates as

$$\omega_{0,\text{eff}}(\phi, \theta) = \frac{a(\theta)b}{\sqrt{(a\sin\phi)^2 + (b\cos\phi)^2}}, \tag{4.9}$$

where $a(\theta) = \frac{\omega_0}{\cos\theta}$ is a semi-major axis, $b = \omega_0$ is a semi-minor axis and $\omega_0 = \omega_{0,\mathrm{eff}}(\phi, \theta = 0)$ is a beam radius at normal incidence.

Given a Gaussian beam with fluence F_0, the area $S_{F>F_\mathrm{T}}$, where fluence F is higher than the defect determined threshold fluence F_T, can be calculated as

$$S_{F>F_\mathrm{T}}(F_0, F_\mathrm{T}) = \frac{\pi a(\theta) b}{2} \ln\left(\frac{F_0}{F_\mathrm{T}}\right) , \tag{4.10}$$

here $S_{F>F_\mathrm{T}}(F_0, F_\mathrm{T})$ is normalized to F_0 for each distance coordinate z.

In order to calculate the number of defects $N(F_0)$ that are damaged after irradiation with a particular fluence F, assumptions on the possible defect ensemble function $g(F)$ should be made. The most commonly used defect ensembles are: degenerate [44], power law [230] and Gaussian [47]. Any of these models or their combinations can be used in principle. Multiplying the function of a defect ensemble with the area above the critical fluence $S_{F>F_\mathrm{T}}$ and integrating along the F_T from 0 to F_0 will provide an average number of defects $N(F_0)$ that are damaged after the exposure to an applied fluence F_0:

$$N(F_0) = \int\limits_0^{F_0} g(F_\mathrm{T}) S_{F>F_\mathrm{T}}(F_0, F_\mathrm{T})\,\mathrm{d}F_\mathrm{T}\,. \tag{4.11}$$

The probability to damage the sample after its exposure to a Gaussian beam of fluence F_0 is then given by the Poisson statistics and can be expressed as

$$P(F_0) = 1 - \mathrm{e}^{-N(F_0)}\,. \tag{4.12}$$

Pulse-to-pulse variance of laser fluence, used for collecting particular damage probability statistics, might be assessed prior to the measurement and parameterized by a convolution procedure described in detail in **Section 2.7.3**.

$$P_{\mathrm{conv}}(F_0) = (P \otimes h)(F_0) = \int_0^\infty P(F_0) h(F - F_0)\, \mathrm{d}F\,, \tag{4.13}$$

where $h(F)$ is the PDF of the fluence distribution. Thus, $P_{\mathrm{conv}}(F_0)$ determines the measured damage probability corrected due to fluence uncertainty.

4.1.3 Volumetric damage probability model

As radiation is propagating along the optical component surface, the damage probability model should be extended to the bulk of the samples. In this case, the LIDT is interpreted in terms of a maximum e-field, not fluence. Thus, the threshold volume rather than the threshold area for damage to occur should be considered (Fig. 4.2). Integrating $S_{|E_0|^2>|E_T|^2}$ along z determines the volume where the electric field intensity is higher than the given threshold:

$$V(|E_0|^2, |E_{\mathrm{T}}|^2) = \int_{z_1}^{z_2} S(|E_0|^2, |E_{\mathrm{T}}|^2)\, \mathrm{d}z\,. \tag{4.14}$$

The threshold volume $V_{|E_0|^2>|E_T|^2}(|E_0|^2, |E_T|^2)$ depends on the spatial beam profile and the incident electric field distribution pattern along the z axis. z_1 and z_2 indicate the range of interest, where the threshold is calculated. For instance, in the case of FS - the coating or Beilby layer thickness.

Three dimensional (3D) electric field distribution inside the optical elements has been numerically simulated by employing the open source project *OpenTMM*, based on a scattering matrix (S-matrix) algorithm [249]. Synthetic samples were divided into the multilayer stacks made of plane-parallel layers with individual optical properties located between two semi-infinite media

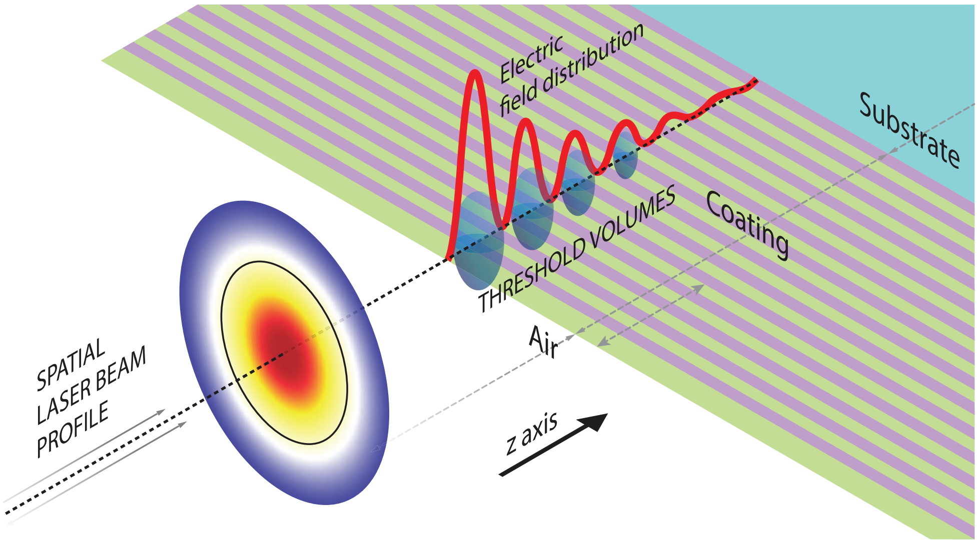

Figure 4.2 The determination of threshold volume $V_{|E_0|^2>|E_\mathrm{T}|^2}(|E_0|^2, |E_\mathrm{T}|^2)$ where the applied fluence $|E_0|^2$ is greater than the threshold fluence $|E_\mathrm{T}|^2$. Black line in spatial beam profile marks level of $1/\mathrm{e}^2$.

(air and substrate). Standing electromagnetic wave patterns within layers were calculated for monochromatic plane waves of a given wavelength. These patterns can be directly applied to long (nanosecond) laser pulses, because their spatial-temporal length is much larger than the thickness of coating or the polished layer containing defects.

Then the average number of defects $N(|E_0|^2)$ can be calculated numerically:

$$N(|E_0|^2) = \int_0^{|E_0|^2} g(|E_\mathrm{T}|^2) V(|E_0|^2, |E_T|^2)\,\mathrm{d}|E_\mathrm{T}|^2\,. \tag{4.15}$$

As in the previous case, the damage probability is calculated according to Eqs. 4.12 and 4.13.

4.2 Experimental methodology

4.2.1 Sample preparation

Four types of samples were produced for damage probability analysis: an uncoated substrate (FS), two types of monolayer films (FS + SiO_2 and FS + HfO_2) and one multilayer highly reflective (HR) mirror. All samples were produced out of identical substrates, which are fused silica samples conventionally manufactured with pad polishing and prepared within the same polishing batch. The thickness of each substrate is 5 mm. Monolayer films and HR coatings are deposited on substrates by ion-beam sputtering (IBS) technology at the Center for Physical Sciences and Technology in Vilnius, Lithuania [250]. FS + SiO_2 monolayer has been chosen to investigate the properties of low-refractive-index deposition materials and FS + HfO_2 monolayer for those of the high-refractive-index materials. Both types of single layer films are of the same 6 quarter-wave optical thickness (QWOT) at 355 nm wavelength. HR mirror consists of 40 layer coating stack, featuring alternating layers of HfO_2 and SiO_2 and a double SiO_2 overcoat layer on top. Refractive-index and physical-thickness analyses were carried out by using the transmittance spectrum data in a low-absorptance spectral region with *Optichar* [251], the optical characterization software. Sample properties are summarized in Table 4.1. All samples are *ex situ* annealed for 1 hour under maximum temperature of 300 °C.

4.2.2 1-on-1 LIDT testing

The LIDT measurements are performed by using the same experimental test bench as described in **Chapter 2** (Fig. 2.6), which is equipped to fit planned experimental research. An additional $\lambda/2$ plate is implemented in order to change the light polarization when necessary. Laser radiation is focused by

Table 4.1 The characteristics of the samples. Here L indicates a low-refractive-index material (SiO_2), H indicates a high-refractive-index material (HfO_2).

Substrate	Coating type	Coating structure	Physical thickness, nm	Refractive index at 355 nm
Fused silica, 5 mm.	Uncoated	—	—	1.477
	FS + SiO_2	Monolayer	361	1.497
	FS + HfO_2	Monolayer	299	1.965
	HfO_2/SiO_2	$L(LH)^{20}$	L - 59.48 H - 45.49	L - 1.492 H - 1.951

a plano–convex lens down to 30 μm at $1/e^2$ level of maximal intensity in the focal plane. The sample positioning system is equipped with two translational and one rotational axis. AOI can be varied in the range of 0–75°. As in previous testing, damage criteria is any visible modification that can be seen by using a Nomarski microscope with 100X magnification.

4.3 Results and discussion

4.3.1 Analysis of experimental damage probability

Identification of weak layers within multilayer coating was performed by analysing three factors: damage morphology, suitability of the fit model and maximum internal $|E|^2$ reached within each sample at damaging fluence. Firstly, the damage probability curves for each tested sample were fitted separately using the planar damage probability model and assuming the degenerate defect ensemble distribution. Damage threshold values obtained by this method are referred to as $LIDT_1$ (Table 4.2). The damage thresholds established using *Approach A* (referred to as $LIDT_2$) and *Approach B* (referred to as $LIDT_3$) are compared in Table 4.2. For A and B cases the analysis of the damage probability curves was performed simultaneously for all curves (0°, 45°) and polar-

Table 4.2 Calculated damage threshold values and other parameters for investigated samples. LIDT_1 is calculated by fitting damage probability curves separately. LIDT_2 is calculated by using *Approach A*. LIDT_3 is calculated by using *Approach B*. $|E(z)_{\max}|^2$ is the calculated internal field maxima at the incidence plane. T is calculated transmittance at air–glass or coating–glass interface plane.

Sample	**AOI, polarization**	**LIDT_1, J/cm^2**	**LIDT_2, J/cm^2**	**LIDT_3, J/cm^2**	$\|\mathrm{E}_{\max}\|^2$	**T**
FS	0°	25.9	25.6	24.2	0.65	0.96
	45°, s	24.78	19.8	25.3	0.50	0.92
	45°, p	21.5	21.3	23.0	0.54	0.99
FS + SiO_2	0°	7.3	7.9	6.3	0.65	0.96
	45°, s	7.1	6.3	6.1	0.50	0.90
	45°, p	6.4	6.5	6.0	0.54	0.99
FS + HfO_2	0°	5.4	4.7	4.1	0.57	0.84
	45°, s	4.3	3.9	3.7	0.48	0.88
	45°, p	4.2	4.3	3.4	0.53	0.98
HR	0°	10.2	—	—	L – 1.8, H – 1.1	1E-3
	45°, s	4.8	—	—	L – 1.9, H – 1.2	5E-3
	45°, p	2.9	—	—	L – 1.2, H – 0.8	0.56

ization (s, p) while varying only the defect ensemble parameters and keeping the irradiation parameters fixed.

The investigation starts with the characterization of FS sample, to screen the effects of deposition procedure. In this case, only defects inherent to the polishing process are important. Damage probability curves are interpreted via the planar damage probability model as the AOI and polarization are varied. Further, the analysis of HR mirror is discussed. A direct application of the *Approach B*, which associates the damage threshold with the maximum transmitted fluence, is not possible, whereas the fluence is undefined for SWs. Thus, the damage threshold behaviour is analyzed by the *Approach A* in terms of the maximum internal field $|E|^2$ reached within each sample. Then the influence of the coating process and the properties of coating materials are analyzed for

FS + HfO_2 and FS + SiO_2 samples. In this case, defects might be distributed both within the optical coating and in the coating–substrate interface. The location of defects can be identified by testing which model of damage probability, planar or volumetric, provides a better agreement with the experimental data. Suitability of models used for fitting was judged according to two criteria:

- ability of model fit to reproduce the shape of experimental data within uncertainty interval of ±2 standard deviations, indicated by experimental error bars;
- capability of reproducing the scaling (relative positions) of experimental curves representing different conditions of irradiation.

4.3.2 Characterization of uncoated fused silica

The typical FS damage morphologies consist of "pin-point" patterns (Fig. 4.3: A), that can be directly linked to localized defects of the surface layer. The measured damage probability curves have a deterministic damage threshold and steep curve transition that is related to high defect density and can be characterized by the degenerate defect ensemble [44], where dominant defects have a strictly defined damage threshold. Due to the laser fluence fluctuations during the measurement, the damage probability curves are bent close to 0 and 1 damage probabilities. Therefore, the damage probability model curves used for

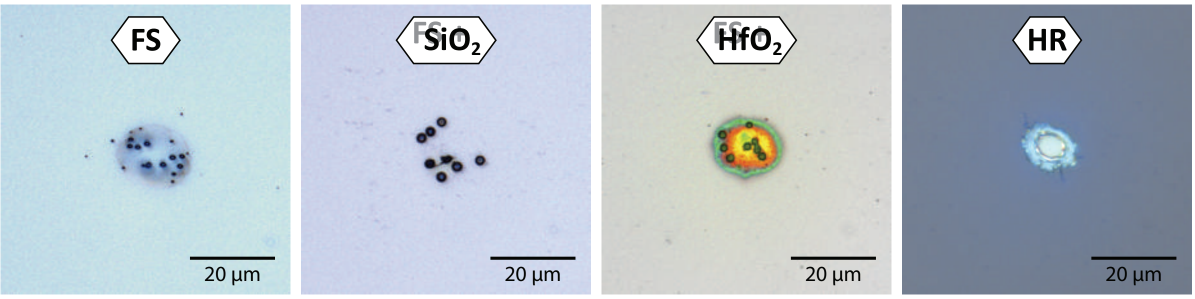

Figure 4.3 Typical damage morphologies of tested samples, when AOI is 0°.

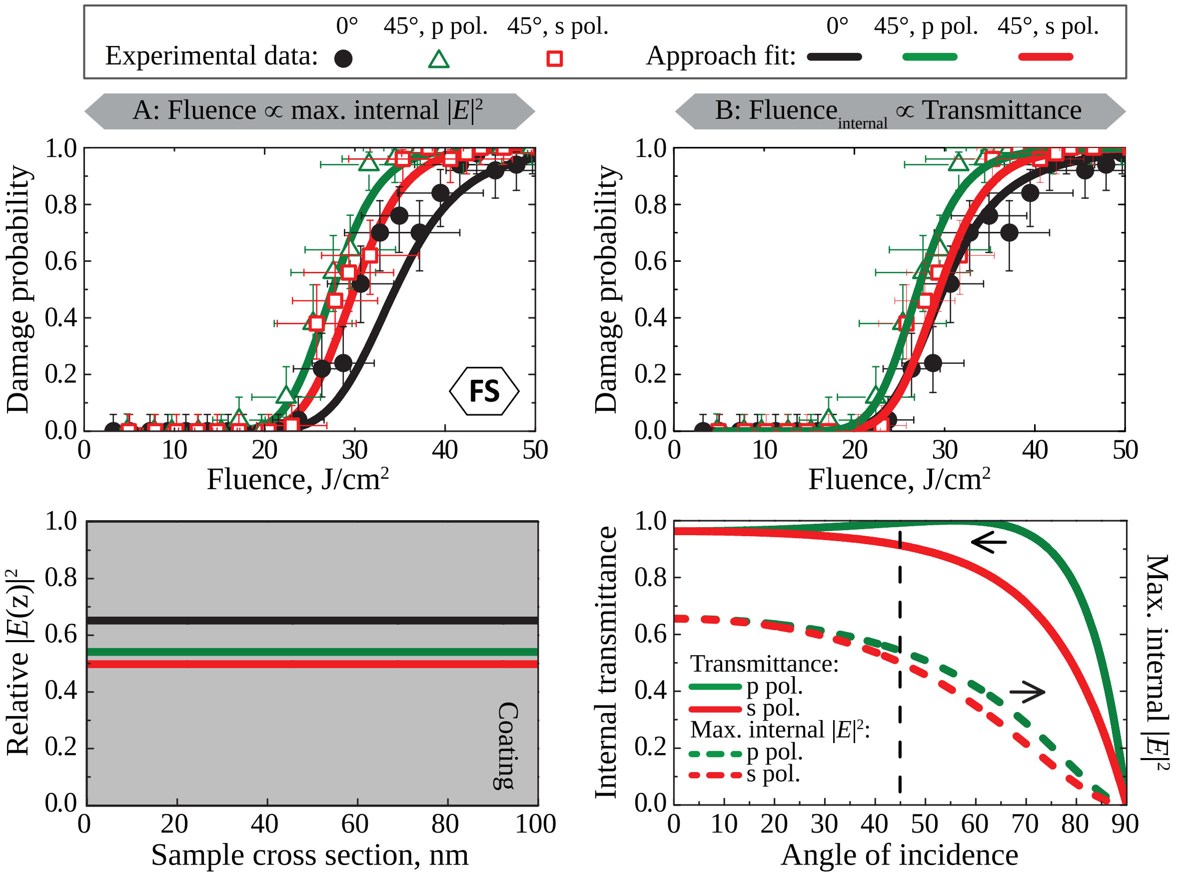

Figure 4.4 **Top**: damage probability curves measured for FS and fitted using $F \propto |E|^2$ (left) and $F \propto$ Transmittance (right) model. **Bottom**: e-field distribution inside the FS (left), transmittance and e-field maxima dependence on AOI (right).

fitting were corrected to compensate the fluence instability [232]. The standard deviation of fluence was characterized to be 6% for the particular measurement set-up. Based on the morphologies and the damage probability curve behaviour, FS sample can be reasonably assumed as a limiting case to investigate the effects caused only by the substrate defects.

Calculated $|E|^2$ and transmittance is shown in Fig. 4.4 (bottom). Both physical characteristics display dependence on the angle and polarization. The e-field distribution remains uniform within the whole FS sample volume (Fig. 4.4: bottom, left). Thus, the interference effects are negligible. The damage probability curves were fitted twice. Firstly, a group of damage probability curves has been fitted simultaneously to test the validity of *Approach A* (LIDT_2) and *Approach B* (LIDT_3). Both approaches have been found in a good agreement with the experimental data within uncertainty interval of ±2 standard deviations (see the fits in Fig. 4.4 for details). From these results it is hard to distinguish, which physical property is responsible for the scaling of the LIDT with the AOI and polarization. Then, each damage probability curve was fitted individually to determine the absolute damage threshold (LIDT_1). As predicted, it was shown to decrease with increasing the AOI changing polarization from s to p (Table 4.2). The absolute damage threshold was further used to evaluate the maximum internal $|E_{\mathrm{T}}|^2$ reached within FS sample (Fig. 4.5) [63]. As seen from the comparison, the values of the maximum internal $|E_{\mathrm{T}}|^2$ vary within the range of uncertainty.

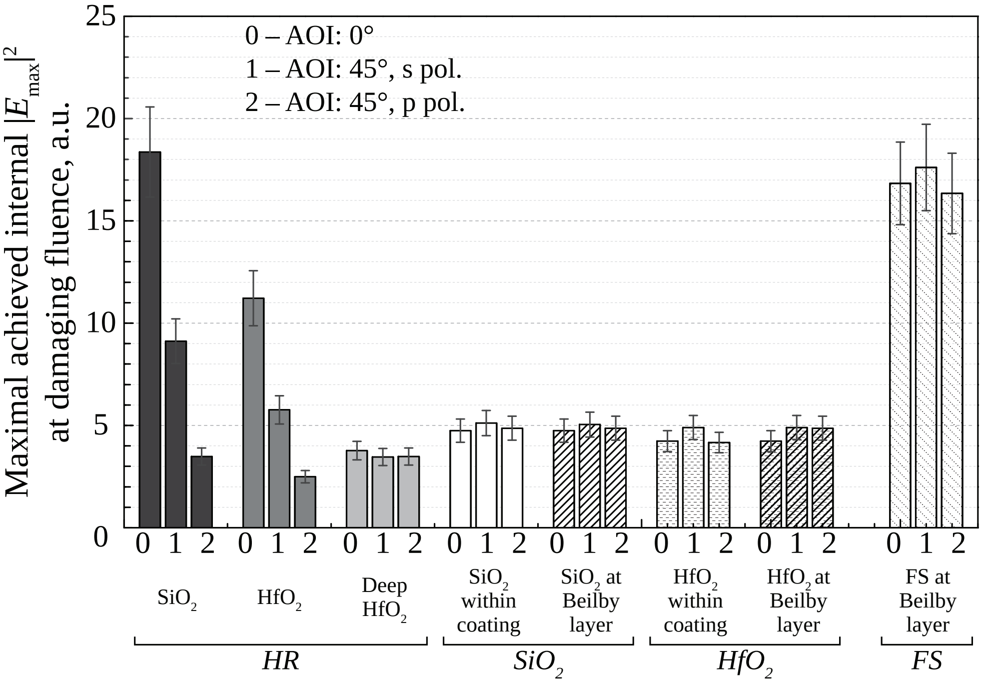

Figure 4.5 The comparison of maximum internal $|E_{\mathbf{T}}|^2$ reached within the samples at damaging fluence.

4.3.3 Characterization of the monolayer films

In the case of monolayer films, both polishing and coatings processes can be assumed to limit LIDT of the entire optical element. A decrease in absolute damage threshold value has been observed for both monolayer films, if compared with the LIDT of FS (Fig. 4.6 and 4.7). E-field distribution as well as transmittance of FS + SiO_2 is almost the same as that of bare FS sample (Fig. 4.6. In the case of FS + HfO_2, maximum internal$|E_\mathrm{T}|^2$ also remains stable within the interval of ± 2 standard deviations for different irradiation conditions(AOI and polarizations) (Table 4.2). The LIDT scaling both with $|E_\mathrm{T}|^2$ (*Approach A*)

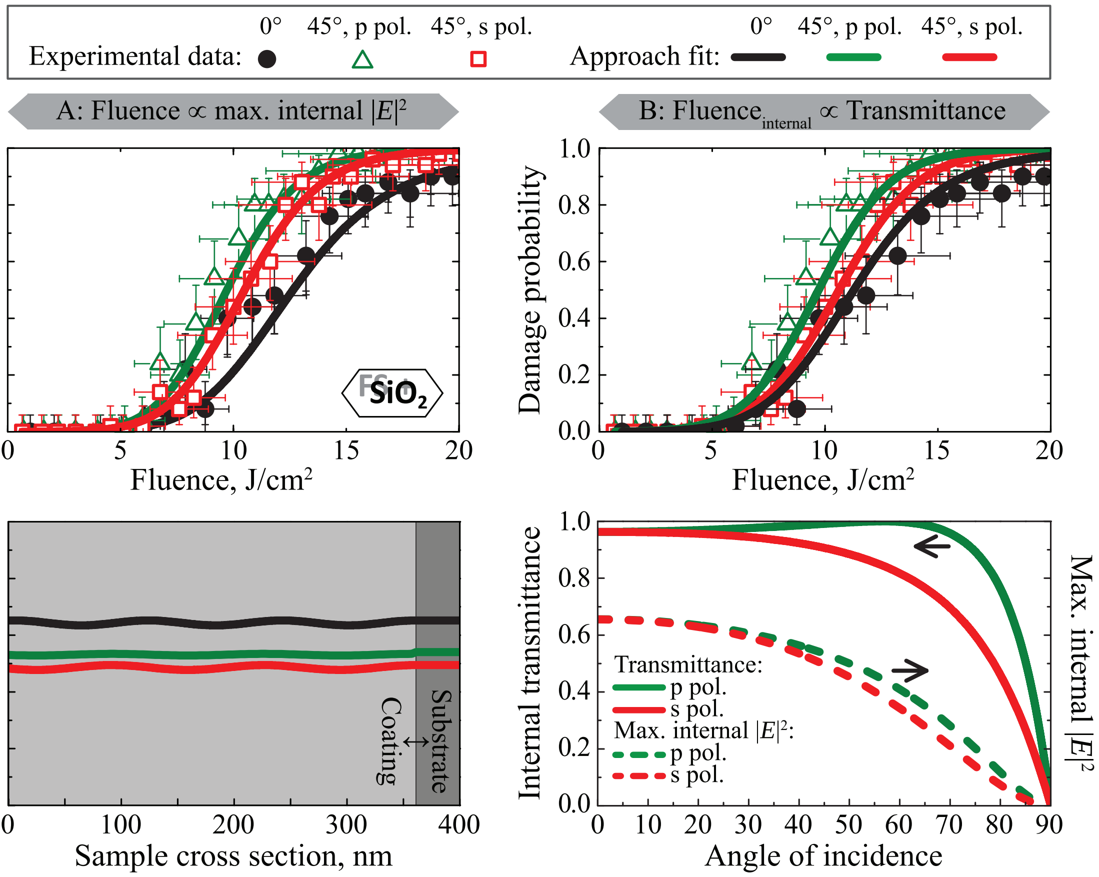

Figure 4.6 **Top**: damage probability curves measured for FS + SiO_2 and fitted using $F \propto |E|^2$ (left) and $F \propto$ Transmittance (right) model. **Bottom**: e-field distribution inside the FS + SiO_2 (left), e-field maxima dependence on AOI (right).

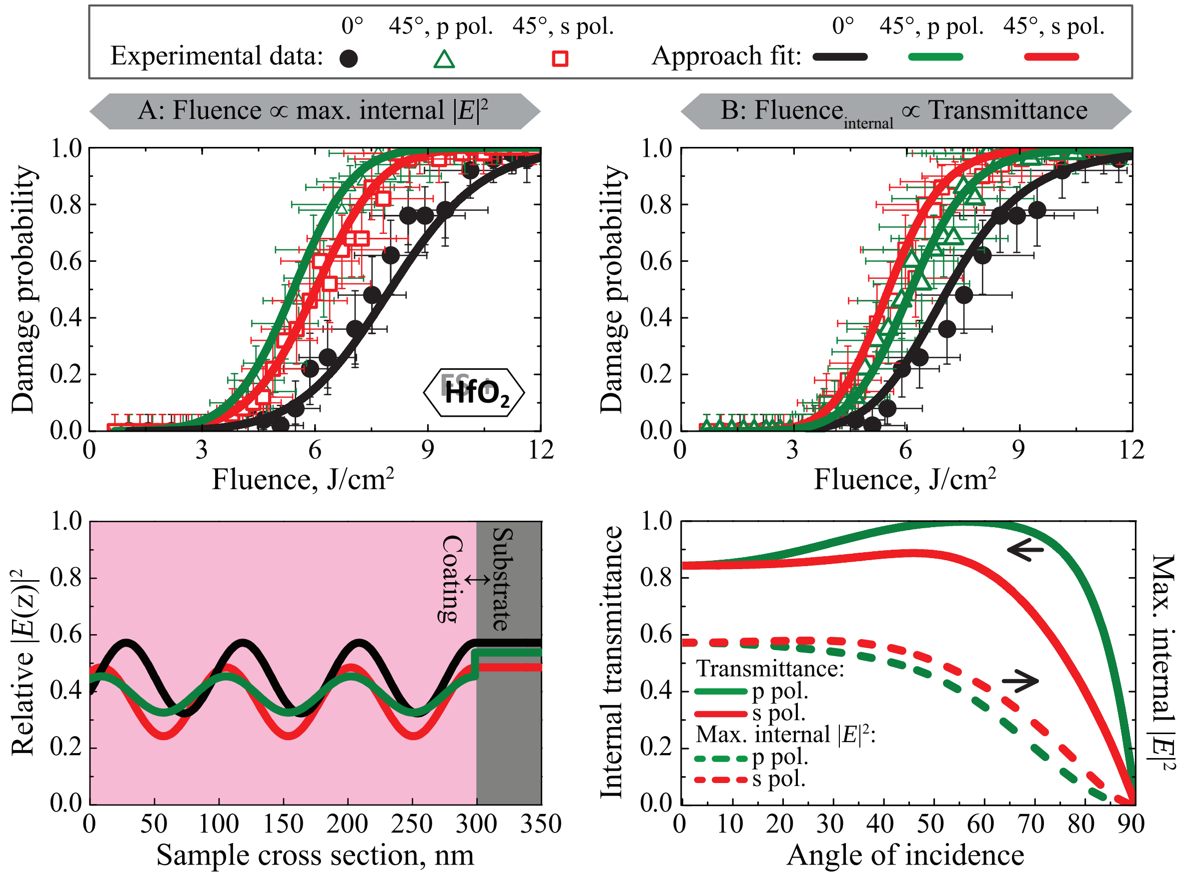

Figure 4.7 **Top**: damage probability curves measured for FS + HfO_2 and fitted using $F \propto |E|^2$ (left) and $F \propto$ Transmittance (right) model. **Bottom**: e-field distribution inside the FS + HfO_2 (left), e-field maxima dependence on AOI (right).

and transmitted fluence (*Approach B*) has been checked in order to explain the experimental results. The analysis has been performed twice by changing the location of limiting defects. Firstly, the defects were assumed within the bulk of the coating and the damage probability curves have been fitted using a volumetric damage probability model. Then, the defects were virtually located on the coating–substrate interface. In this case a planar damage probability model has been used. The best agreement with the experimental data was found in the case of planar defects at the coating–substrate interface. This indicates that the damage threshold of tested monolayer coating should be limited by the polishing defects. The recorded damage morphologies support this assumption (Fig.

4.3), revealing "pin-point" like defects similar to those observed on FS. Furthermore, maximum internal $|E_{\mathrm{T}}|^2$ reached at silica and hafnia monolayers and glass interface, as seen in the comparison (Fig. 4.5), is almost the same, thus indicating that LIDT limiting defects are indeed the same. Hafnia layer itself is not a limiting factor. However, then internal LIDT of FS and monolayer films should be the same. The results shown in the comparison contradict the previous assumption. In order to investigate this phenomenon another limiting case when LIDT is limited only by deposition process has been analyzed.

4.3.4 Highly reflective multilayer coating

The damage threshold of HR mirror is assumed to be limited only by the coating defects. When the sample is exposed to 0°/45° AOI and s polarization radiation, the e-field distribution decays within the coating and does not reach the substrate (Fig. 4.8). In the case of 45° AOI and p polarization, the laser beam penetrates both the coating and the substrate. However, $|E|^2$ inside the coating is 4 times larger than within a substrate. Therefore, it is reasonable to expect the

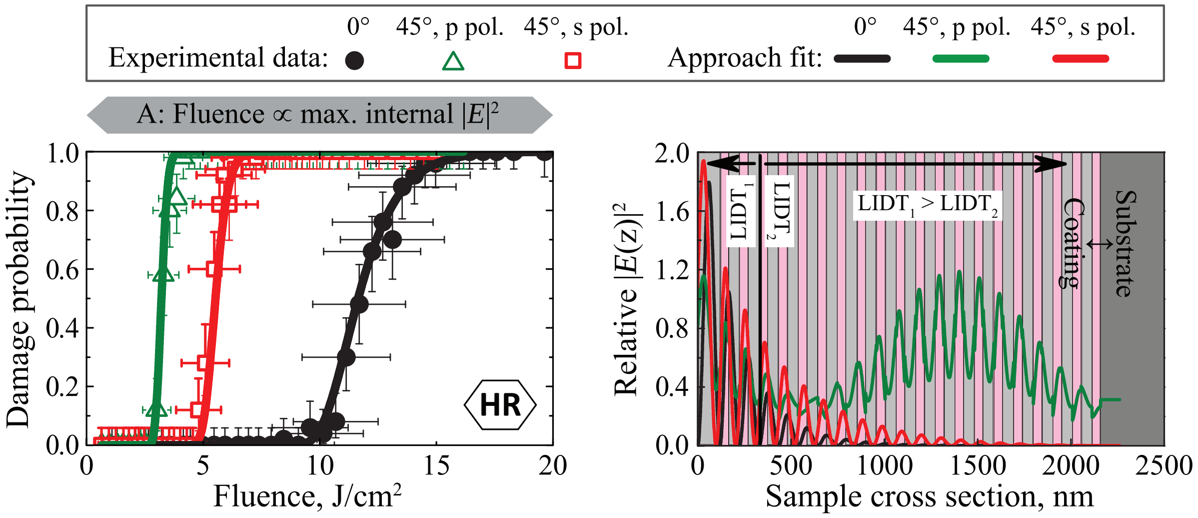

Figure 4.8 **Left**: damage probability curves measured for HR with central wavelength at 355 nm. **Right**: e-field distribution inside HR.

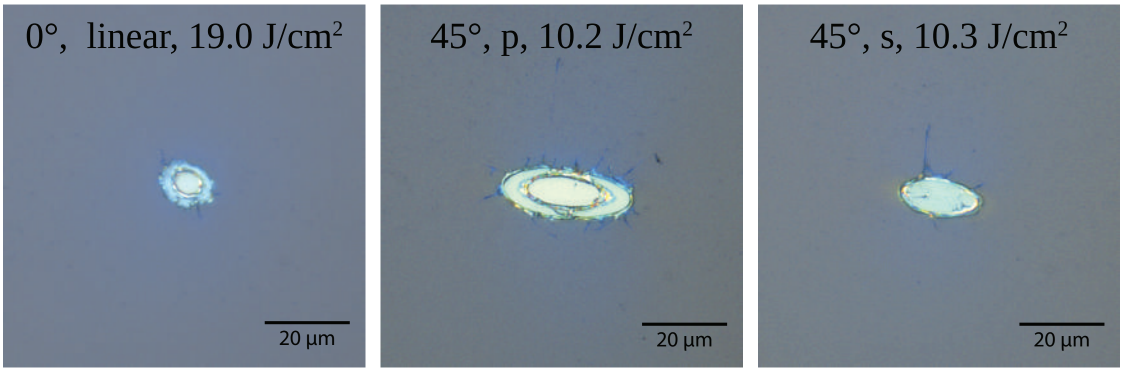

Figure 4.9 Typical damage morphologies recorded for HR mirror.

coating damage to occur before the substrate is damaged. Typical damage morphology recorded for the HR multilayer mirror (Fig. 4.3: D) reveals an absence of "pin-point" defects. The peeling of the coating is indicated as the primarily damage formation mechanism under both tested angles of incidence and both polarizations (Fig. 4.9). It confirms that the substrate defects are insignificant for multilayer coatings. The number of the peeled layers depends on the polarization. Parallel polarized radiation destroys deep layers of the coating, while perpendicularly polarized light is capable of peeling only the top layers. These features of observed morphologies are in agreement with the predicted e-field pattern within the HR mirror. The 1-on-1 LIDT results are presented in Fig. 4.8. The ratio of damage thresholds recorded for different AOIs and polarizations does not correlate with a ratio of maximum internal field $|E|^2$, reached at particular material, neither does it correlate with a maximum transmitted fluence F_{internal}, corresponding to the incident damaging fluence (Table 4.2). Maximum internal $|E_{\mathrm{T}}|^2$ reached at the damaging fluence of LIDT has been calculated separately for both silica and hafnia layers within the HR mirror (Fig. 4.5). It is seen from the comparison that a maximum internal $|E_{\mathrm{T}}|^2$ reached within uncoated FS is lower than that of silica layer within multilayer coating. It should be noted that the maximum internal $|E_{\mathrm{T}}|^2$, reached within SiO_2 layers at 0° AOI, is comparable with the maximum internal $|E_{\mathrm{T}}|^2$, reached within the uncoated FS sample. However, this behaviour cannot be linked to the substrate defects, because in this case the electric field is suppressed within the coating. In spite of the fact that the maximum internal $|E|^2$ reached on HfO_2 sublayers is lower than that for SiO_2 sublayers at the tested AOIs and both polarizations, the HfO_2 layer is expected to limit the LIDT of the whole multilayer. This assumption is made by considering *a priori* knowledge from bibliographic inputs stating that the internal LIDT of bulk dielectric materials is inversely proportional to their refractive index [252–254]. Nevertheless, neither *Approach A* nor *Approach B* are capable of fitting the measured damage probability behaviour for a particular sample in the case, when resistivity of sublayers is only a static function of the refractive index. Additional effects that take place only in multilayer stacks should be considered.

4.4 Discussion: identification of weak layers

During the analysis of LIDT of HR mirror, (Fig. 4.5) a very interesting tendency has been revealed that deserves special attention. The internal e-field reached in fused silica and hafnia layers is very different at the damaging fluence for different polarizations and AOIs. This should not be the case if one of materials is the only factor limiting the resistance of the whole coating. Thus, an assumption can be made that the resistance to laser irradiation at given conditions should be a function of the layer depth within the multilayer. This assumption was further tested numerically. Top layers of silica and hafnia were assumed to have higher damage threshold than the rest (Fig. 4.8). It has been noticed that the maximum internal $|E_{\mathrm{T}}|^2$ becomes almost constant at the damaging fluence for hafnia layers located 300 nm from the top surface (Fig. 4.5) for the investigated irradiation cases. After such consideration, *Approach A* was able to fit the experimental data (Fig. 4.8: left) and support the validity of the assumption. More work is required to clarify the physical reasons why the top layers have higher resistance. Only speculations could be made here

– association with annealing process, direct contact with atmosphere, distinct thermal-mechanical confinement and stress accumulation within a multilayer, as well as nonlinear optical processes during the laser–matter interaction.

It should be noticed as well that the top silica and hafnia layers in the HR mirror tolerate much higher e-field within the multilayer stack without being damaged compared to monolayer silica and hafnia coatings. This experimental fact implies that internal LIDT of the coating material itself cannot limit the LIDT in the case of a single layer. In other words, two "high damage threshold" materials combined together result in a low resistant material. Taking into consideration previous arguments and namely:

- similarity in "pin-point" damage morphology between FS and FS + SiO_2;
- absence of "pin-point" morphology patterns in HR mirror when e-field does not reach the Beilby layer;
- much higher internal e-fields tolerated within both deposited silica of multilayer and the Beilby layer of FS at damaging fluence

bring to the conclusion that interaction effect should exist. One explanation here could be that polishing defects change their ability to withstand the laser irradiation as additional materials are deposited on top. Such a phenomenon was first reported by S. Papernov et al. [187]. It suggests that the absorption of defects changes due to the surrounding lattice – the matrix effect. The maximum internal $|E_{\mathrm{T}}|^2$ reached within a FS + SiO_2 remains the same when changing the AOI and polarization (Fig. 4.5). The same tendency as in the case of a HR mirror can be recognized here: the deposition of defective layer causes the reduction of internal threshold. Differences of temperature and stress accumulation along the coating could explain such behavior [255].

4.5 Conclusions

The comparison of internal maximum $|E|^2$ reached within optical elements at damaging fluence shows that the decrease of nanosecond LIDT, observed in monolayer samples exposed to UV (355 nm) radiation, is associated with the polishing defects and is strongly influenced by the matrix effect due to layers deposited on top. This assumption is supported by the same “pin-point” damage morphologies, observed for the uncoated and single layer coated samples, and a much higher internal electric field reached in a HR mirror consisting of similar sublayers. The behaviour of LID probability curves, recorded for a HR mirror with central 355 nm wavelength at varying AOI and polarization, suggests that the internal LIDT of the multilayer varies with the layer depth. The LID scaling with the AOI and polarization is well defined by employing the maximum e-field, reached within an optical element, approach and the maximum transmitted fluence approach. In order to distinguish between theses two methods, a higher resolution of the LIDT measurements is needed.

Main results and conclusions

By employing Monte Carlo method, it has been shown that maximum likelihood based evaluation procedure, which takes into consideration the binomial nature of damage probability measurement, helps to improve the repeatability of determined LIDT values, as compared with standard approach based on the least squares method. The accuracy of determined results increases when fluence fluctuations are taken into account in the damage probability model.

In order to assess the true distributions of defect ensembles of damage precursors, a direct comparison of two methods, i.e. raster scan and damage probability measurements, has been performed for the first time. It has been revealed that these methods conclude different results. Both approaches are incapable of telling which of defect ensembles – power law or Gaussian is the true one, while it is clear that degenerate ensemble does not suit as the true one. A new approach, which allows to include the measurement uncertainty in raster scan measurements while determining defect ensembles is introduced. The research has found that the results obtained using the raster scan method are affected due to surface contamination by ablation products, and the quantity of defects might be misinterpreted owing to defect clusters.

In an attempt to understand the role of defects in multilayer coatings better, optical resistance metrology has been expanded to include interference phenomena and volumetric defect ensembles. A new statistical tool for interpreting data on damage probability measurements has been created, which allows for a better understanding of the properties of surface defects occurring in the process of polishing when they are additionally deposited with transparent layers. Also, it has been revealed that the LIDT of identical layers forming multilayer highly reflective HfO_2/SiO_2 mirror coating depends on specific depth of a layer in respect to the surface.

Bibliography

[1] T. H. Maiman, Stimulated optical radiation in ruby, Nature **187**, 493–494 (1960).

[2] R. M. Wood, *Laser damage in optical materials* (A. Hilger, Bristol, 1986).

[3] D. Ristau, *Laser-Induced Damage in Optical Materials* (CRC press, Taylor & Francis Group, Florida, 2014).

[4] R. R. Gattass and E. Mazur, Femtosecond laser micromachining in transparent materials, Nat. Photonics **2**(4), 219–225 (2008).

[5] P. D. Maker, R. W. Terhune, and C. M. Savage, Optical third harmonic generation, J. Exp. Theor. Phys.+ **1**, 1559 (1964).

[6] C. R. Giuliano, Laser-induced damage to transparent dielectric materials, Appl. Phys. Lett. **5**(7), 137–139 (1964).

[7] J. H. Cullom and R. W. Waynant, Determination of laser damage threshold for various glasses, Appl. Optics **3**(8), 989–990 (1964).

[8] M. Hercher, Laser-induced damage in transparent media, J. Opt. Soc. Am. **54**(4), 563 (1964).

[9] 21254-1: Determination of laser-induced damage threshold of optical surfaces – Part 1: 1-on-1 test, ISO (2011).

[10] N. Bloembergen, Laser-induced electric breakdown in solids, IEEE J. Quantum Elect. **10**(3), 375–386 (1974).

[11] S. C. Jones, P. Braunlich, R. T. Casper, X. A. Shen, and P. Kelly, Recent progress on laser-induced modifications and intrinsic bulk damage of wide-gap optical materials, Opt. Eng. **28**(10), 281039 (1989).

[12] K. Yoshida, N. Umemura, N. Kuzuu, H. Yoshida, T. Kamimura, and T. Sasaki, Wavelength dependence of laser-induced damage in fused silica and fused quartz, Proc. SPIE **3244**, 164–175 (1998).

[13] N. Kuzuu, K. Yoshida, H. Yoshida, T. Kamimura, and N. Kamisugi, Laser-induced bulk damage in various types of vitreous silica at 1064,

532, 355, and 266 nm: evidence of different damage mechanisms between 266 nm and longer wavelengths, Appl. Optics **38**(12), 2510–2515 (1999).

[14] C. W. Carr, H. B. Radousky, and S. G. Demos, Wavelength dependence of laser-induced damage: determining the damage initiation mechanisms, Phys. Rev. Lett. **91**(12), 127402 (2003).

[15] M. Jupé, L. Jensen, A. Melninkaitis, V. Sirutkaitis, and D. Ristau, Calculations and experimental demonstration of multi-photon absorption governing fs laser-induced damage in titania, Opt. Express **17**(15), 12269–12278 (2009).

[16] E. S. Bliss, Pulse duration dependence of laser damage mechanisms, Opto-Electron. Rev. **3**(2), 99–108 (1971).

[17] D. Du, X. Liu, G. Korn, J. Squier, and G. Mourou, Laser-induced breakdown by impact ionization in SiO_2 with pulse widths from 7 ns to 150 fs, Appl. Phys. Lett. **64**(23), 3071–3073 (1994).

[18] B. C. Stuart, M. D. Feit, S. Herman, A. M. Rubenchik, B. W. Shore, and M. D. Perry, Nanosecond-to-femtosecond laser-induced breakdown in dielectrics, Phys. Rev. B **53**(4), 1749 (1996).

[19] B. C. Stuart, M. D. Feit, A. M. Rubenchik, B. W. Shore, and M. D. Perry, Laser-induced damage in dielectrics with nanosecond to subpicosecond pulses, Phys. Rev. Lett. **74**(12), 2248 (1995).

[20] G. Batavičiūtė, E. Pupka, V. Pyragaitė, L. Smalakys, and A. Melninkaitis, Effect of longitudinal laser mode beating in damage probability measurements, Proc. SPIE **8885**, 88851M (2013).

[21] M. Mero, J. Liu, W. Rudolph, D. Ristau, and K. Starke, Scaling laws of femtosecond laser pulse induced breakdown in oxide films, Phys. Rev. B **71**(11), 115109 (2005).

[22] W. Riede, H. Schröder, G. Batavičiūtė, D. Wernham, A. Tighe, F. Pettazzi, and J. Alves, Laser-induced contamination on space optics, Proc. SPIE **8190**, 81901E (2011).

[23] W. Riede, P. Allenspacher, H. Schröder, D. Wernham, and Y. Lien, Laser-induced hydrocarbon contamination in vacuum, Proc. SPIE **5991**, 59910H (2005).

[24] L. Jensen, M. Jupé, H. Mädebach, H. Ehlers, K. Starke, D. Ristau, W. Riede, et al., Damage threshold investigations of high-power laser optics under atmospheric and vacuum conditions, Proc. SPIE **6403**, 64030U (2006).

[25] K. Mikami, S. Motokoshi, M. Fujita, T. Jitsuno, and K. A. Tanaka, Laser-induced damage thresholds of optical coatings at different temperature, Proc. SPIE **8190**, 81900A (2011).

[26] K. Mikami, S. Motokoshi, T. Somekawa, T. Jitsuno, M. Fujita, and K. A. Tanaka, Temperature dependence of laser-induced damage threshold of optical coatings at different pulse widths, Opt. Express **21**(23), 28719–28728 (2013).

[27] L. Yang, X. D. Yuan, H. X. Deng, X. Xiang, W. G. Zheng, S. B. He, Y. Jiang, et al., Influence of ambient temperature on nanosecond and picosecond laser-induced bulk damage of fused silica, Adv. Cond. Matter Phys. **5** (2014).

[28] N. Bloembergen, Role of cracks, pores, and absorbing inclusions on laser induced damage threshold at surfaces of transparent dielectrics, Appl. Optics **12**(4), 661–664 (1973).

[29] M. R. Kozlowski and R. Chow, Role of defects in laser damage of multilayer coatings, Proc. SPIE **2114**, 640–649 (1994).

[30] L. Skuja, Optically active oxygen-deficiency-related centers in amorphous silicon dioxide, J. Non-cryst. Solids **239**(1), 16–48 (1998).

[31] L. Gallais, D. Douti, M. Commandré, G. Batavičiūtė, E. Pupka, M. Ščiuka, L. Smalakys, et al., Wavelength dependence of femtosecond laser-induced damage threshold of optical materials, J. Appl. Phys. **117**(22), 223103 (2015).

[32] C. A. Haynam, P. J. Wegner, J. M. Auerbach, M. W. Bowers, S. N. Dixit, G. V. Erbert, G. M. Heestand, et al., National Ignition Facility laser performance status, Appl. Optics **46**(16), 3276–3303 (2007).

[33] N. Fleurot, C. Cavailler, and J. L. Bourgade, The Laser Megajoule Project dedicated to inertial confinement fusion: Development and construction status, Fusion Eng. Des. **74**(1), 147–154 (2005).

[34] J. P. Chambaret, O. Chekhlov, G. Cheriaux, J. Collier, R. Dabu, P. Dombi, A. M. Dunne, et al., Extreme light infrastructure: laser architecture and major challenges, Proc. SPIE **7721**, 77211D (2010).

[35] S. C. Seitel, A. Giesen, and J. Becker, International standard test method for laser-induced damage threshold of optical surfaces, Proc. SPIE **1848**, 2–3 (1993).

[36] J. Becker and A. Bernhardt, ISO 11254: an international standard for the determination of the laser-induced damage threshold, Proc. SPIE **2114**, 703 (1994).

[37] A. F. Stewart and A. H. Guenther, Laser-induced damage: an introduction, Appl. Optics **23**(21), 3741–3742 (1984).

[38] U. Willamowski, M. Dieckmann, D. Ristau, U. Broulik, B. Steiger, and W. Riede, Laser induced damage threshold measurements according to ISO/DIS 11254-1: Results of a national round robin experiment on Nd: YAG laser optics in *Fourth International Workshop on Laser Beam and Optics Characterization, pp314, VDI-Verlag*, (1997).

[39] W. Riede, U. Willamowski, M. Dieckmann, D. Ristau, U. Broulik, and B. Steiger, Laser-induced damage measurements according to ISO/DIS 11 254-1: results of a national round robin experiment on Nd: YAG laser optics, Proc. SPIE **8147**, 96–105 (1998).

[40] J. W. Arenberg, W. Riede, U. Broulik, B. Steiger, U. Willamowski, and D. Ristau, National round-robin test on laser induced damage at 1.064 μm: Revised data reduction and correlation analysis, Proc. SPIE **2258**,

645–656 (1999).

[41] A. M. Rubenchik and M. D. Feit, Initiation, growth, and mitigation of UV-laser-induced damage in fused silica, Proc. SPIE **4679**, 79–95 (2002).

[42] S. Papernov, A. W. Schmid, A. L. Rigatti, and J. Howe, Establishing links between single gold nanoparticles buried inside SiO_2 thin film and 351 nm pulsed-laser damage morphology, Proc. SPIE **4679**, 282–292 (2002).

[43] S. R. Foltyn, Spotsize effects in laser damage testing, NBS Spec. Publ. **669**, 368 (1984).

[44] J. O. Porteus and S. C. Seitel, Absolute onset of optical surface damage using distributed defect ensembles, Appl. Optics **23**(21), 3796–3805 (1984).

[45] J. Y. Natoli, L. Gallais, H. Akhouayri, and C. Amra, Laser-induced damage of materials in bulk, thin-film, and liquid forms, Appl. Optics **41**(16), 3156–3166 (2002).

[46] R. M. O'Connell, Onset threshold analysis of defect-driven surface and bulk laser damage, Appl. Optics **31**(21), 4143–4153 (1992).

[47] H. Krol, L. Gallais, C. Greezes-Besset, J. Y. Natoli, and M. Commandré, Investigation of nanoprecursors threshold distribution in laser-damage testing, Opt. Commun. **256**(1-3), 184–189 (2005).

[48] A. Melninkaitis, G. Batavičiūtė, and V. Sirutkaitis, Numerical analysis of laser-induced damage threshold search algorithms and their uncertainty, Proc. SPIE **7504**, 75041D (2009).

[49] S. Liukaitytė, G. Batavičiūtė, E. Pupka, M. Ščiuka, I. Kraujalienė, D. Tumosa, A. Skrebutėnas, et al., Effect of conventional fused silica preparation and deposition techniques on surface roughness, scattering, and laser damage resistance, Proc. SPIE **8530**, 853027 (2012).

[50] T. A. Laurence, J. D. Bude, S. Ly, N. Shen, and M. D. Feit, Extracting the distribution of laser damage precursors on fused silica surfaces for 351 nm, 3 ns laser pulses at high fluences (20-150 J/cm^2), Opt. Express **20**(10), 11561–11573 (2012).

[51] F. Jansen, The columnar microstructure and nodular growth of a-As_2S_3 films, Thin Solid Films **78**(1), 15–24 (1981).

[52] F. Seitz, On the theory of electron multiplication in crystals, Phys. Rev. **76**(9), 1376 (1949).

[53] A. S. Epifanov, Avalanche ionization induced in solid transparent dielectrics by strong laser pulses, J. Exp. Theor. Phys.+ **40**, 897 (1975).

[54] A. S. Epifanov, A. A. Manenkov, and A. M. Prokhorov, Theory of avalanche ionization induced in transparent dielectrics by an electromagnetic field, Sov. Phys.-JETP **70**, 728–737 (1976).

[55] A. S. Epifanov and S. V. Garnov, Statistical approach to theory of electron–avalanche ionization in solids, IEEE J. Quantum Elect. **17**, 2023–2026 (1981).

[56] M. D. Feit, A. M. Rubenchik, D. R. Faux, R. A. Riddle, A. Shapiro, D. C. Eder, B. M. Penetrante, et al., Modeling of laser damage initiated by surface contamination, Proc. SPIE **2966**, 417–424 (1996).

[57] B. C. Stuart, M. D. Feit, S. Herman, A. M. Rubenchik, B. W. Shore, and M. D. Perry, Nanosecond-to-femtosecond laser-induced breakdown in dielectrics, Phys. Rev. B **53**(4), 1749 (1996).

[58] F. Rainer, L. J. Atherton, and J. J. D. Yoreo, Laser damage to production–and research–grade KDP crystals, Proc. SPIE **2157**, 46–58 (1993).

[59] M. Mero, B. Clapp, J. C. Jasapara, W. Rudolph, D. Ristau, K. Starke, S. Martin, et al., On the damage behavior of dielectric films when illuminated with multiple femtosecond laser pulses, Opt. Eng. **44**(5), 051107 (2005).

[60] A. Vogel and V. Venugopalan, Mechanisms of pulsed laser ablation of biological tissues, Chem. Rev. **103**(2), 577–644 (2003).

[61] L. V. Keldysh, Ionization in the field of a strong electromagnetic wave, Sov. Phys.-JETP **20**(5), 1307–1314 (1965).

[62] B. Rethfeld, Unified model for the free-electron avalanche in laser-irradiated dielectrics, Phys. Rev. Lett. **92**(18), 187401 (2004).

[63] J. Jasapara, A. V. V. Nampoothiri, W. Rudolph, D. Ristau, and K. Starke, Femtosecond laser pulse induced breakdown in dielectric thin films, Phys. Rev. B **63**, 045117 (2001).

[64] L. H. Holway Jr and D. W. Fradin, Electron avalanche breakdown by laser radiation in insulating crystals, J. Appl. Phys. **46**(1), 279–291 (1975).

[65] E. S. Bliss, D. Milam, and R. A. Bradbury, Dielectric mirror damage by laser radiation over a range of pulse durations and beam radii, Appl. Optics **12**(4), 677–689 (1973).

[66] M. J. Soileau, W. Williams, and E. W. Van Stryland, Optical power limiter with picosecond response time, IEEE J. Quantum Elect. **19**(4), 731–735 (1983).

[67] W. Lowdermilk and D. Milam, Laser-induced surface and coating damage, IEEE J. Quantum Elect. **17**(9), 1888–1903 (1981).

[68] T. W. Walker, A. H. Guenther, and P. Nielsen, Pulsed laser-induced damage to thin-film optical coatings-part I: experimental, IEEE J. Quantum Elect. **17**(10), 2041–2052 (1981).

[69] J. H. Campbell, F. Rainer, M. R. Kozlowski, C. R. Wolfe, I. M. Thomas, and F. P. Milanovich, Damage resistant optics for a megajoule solid state laser, Proc. SPIE **1441**, 444–456 (1991).

[70] M. D. Perry, B. C. Stuart, P. S. Banks, M. D. Feit, V. Yanovsky, and A. M. Rubenchik, Ultrashort-pulse laser machining of dielectric materials, J. Appl. Phys. **85**(9), 6803–6810 (1999).

[71] M. Chambonneau, R. Diaz, G. Duchateau, P. Grua, J. Y. Natoli, J. L. Rullier, and L. Lamaignère, Laser-induced damage morphology in fused silica at 1064 nm in the nanosecond regime, Proc. SPIE **9237**, 923715 (2014).

[72] A. Smith, B. Do, R. Schuster, and D. Collier, Rate equation model of bulk

optical damage of silica, and the influence of polishing on surface optical damage of silica, Proc. SPIE **6873**, 68730U (2008).

[73] L. Englert, B. Rethfeld, L. Haag, M. Wollenhaupt, C. Sarpe-Tudoran, and T. Baumert, Control of ionization processes in high band gap materials via tailored femtosecond pulses, Opt. Express **15**(26), 17855–17862 (2007).

[74] L. G. DeShazer, B. E. Newnam, and K. M. Leung, Role of coating defects in laser-induced damage to dielectric thin films, Appl. Phys. Lett. **23**(11), 607–609 (1973).

[75] J. R. Bettis, R. A. House II, and A. H. Guenther, Spot size and pulse duration dependence of laser-induced damage, Proc. SPIE **622**, 338–345 (1976).

[76] E. W. Van Stryland, M. J. Soileau, A. L. Smirl, and W. E. Williams, Pulse-width and focal-volume dependence of laser-induced breakdown, Phys. Rev. B **23**(5), 2144 (1981).

[77] B. M. Kim, M. D. Feit, A. M. Rubenchik, E. J. Joslin, J. Eichler, P. C. Stoller, and L. B. Da Silva, Effects of high repetition rate and beam size on hard tissue damage due to subpicosecond laser pulses, Appl. Phys. Lett. **76**(26), 4001–4003 (2000).

[78] S. Martin, A. Hertwig, M. Lenzner, J. Krüger, and W. Kautek, Spot-size dependence of the ablation threshold in dielectrics for femtosecond laser pulses, Appl. Phys. A - Mater. **77**(7), 883–884 (2003).

[79] B. Wolff-Rottke, J. Ihlemann, H. Schmidt, and A. Scholl, Influence of the laser-spot diameter on photo-ablation rates, Appl. Phys. A - Mater. **60**(1), 13–17 (1995).

[80] L. Jensen, S. Schrameyer, M. Jupé, H. Blaschke, and D. Ristau, Spot-size dependence of the LIDT from the NIR to the UV, Proc. SPIE **7504**, 75041E (2009).

[81] F. Brandi, N. Burdet, R. Carzino, and A. Diaspro, Very large spot size effect in nanosecond laser drilling efficiency of silicon, Opt. Express **18**(22),

23488–23494 (2010).

[82] M. Bass and H. H. Barrett, The probability and dynamics of damaging optical materials with lasers, NBS Spec. Publ. **356**, 76–90 (1971).

[83] M. Bass and H. H. Barrett, Avalanche breakdown and the probabilistic nature of laser-induced damage, IEEE J. Quantum Elect. **8**(3), 338–343 (1972).

[84] M. Bass and D. W. Fradin, Surface and bulk laser-damage statistics and the identification of intrinsic breakdown processes, IEEE J. Quantum Elect. **9**(9), 890–896 (1973).

[85] N. L. Boling, P. Bräunlich, A. Schmid, and P. Kelly, Statistics in laser-induced dielectric breakdown, Appl. Phys. Lett. **27**(4), 191–194 (1975).

[86] L. D. Merkle, M. Bass, and R. T. Swimm, Multiple pulse laser-induced bulk damage in crystalline and fused quartz at 1.064 and 0.532 μm, Opt. Eng. **22**(4), 224405 (1983).

[87] R. M. O'Connell, T. F. Deaton, and T. T. Saito, Single-and multiple-shot laser-damage properties of commercial grade PMMA, Appl. Optics **23**(5), 682–688 (1984).

[88] A. Chmel, Fatigue laser-induced damage in transparent materials, Mater. Sci. Eng. B - Adv. **49**(3), 175–190 (1997).

[89] L. Gallais, J. Y. Natoli, and C. Amra, Statistical study of single and multiple pulse laser-induced damage in glasses, Opt. Express **10**(25), 1465–1474 (2002).

[90] J. Y. Natoli, B. Bertussi, and M. Commandré, Effect of multiple laser irradiations on silica at 1064 and 355 nm, Opt. Lett. **30**(11), 1315–1317 (2005).

[91] F. R. Wagner, A. Hildenbrand, H. Akhouayri, C. Gouldieff, L. Gallais, M. Commandré, and J. Y. Natoli, Multipulse laser damage in potassium titanyl phosphate: statistical interpretation of measurements and the damage initiation mechanism, Opt. Eng. **51**(12), 121806 (2012).

[92] F. R. Wagner, C. Gouldieff, and J. Y. Natoli, Contrasted material responses to nanosecond multiple-pulse laser damage: from statistical behavior to material modification, Opt. Lett. **38**(11), 1869–1871 (2013).

[93] C. Gouldieff, F. Wagner, and J. Y. Natoli, Nanosecond UV laser-induced fatigue effects in the bulk of synthetic fused silica: a multi-parameter study, Opt. Express **23**(3), 2962–2972 (2015).

[94] F. R. Wagner, C. Gouldieff, J. Y. Natoli, and M. Commandré, Nanosecond multi-pulse laser-induced damage mechanisms in pure and mixed oxide thin films, Thin Solid Films (2015).

[95] A. Melninkaitis, J. Mirauskas, M. Jupé, D. Ristau, J. W. Arenberg, and V. Sirutkaitis, The effect of pseudo-accumulation in the measurement of fatigue laser-induced damage threshold, Proc. SPIE **7132**, 713203 (2008).

[96] L. D. Khazov, I. A. Fersman, and V. I. U. Bortniker, Accumulative effect of fracture of transparent dielectrics subjected to repeated laser irradiation, Sov. Phys.-JETP **44**, 2020–2022 (1974).

[97] Y. K. Danileiko, A. A. Manenkov, and V. S. Nechitailo, Prethreshold phenomena in laser damage of optical materials, Quantum Electron.+ **6**(2), 236 (1976).

[98] A. Chmel and S. B. Eronko, Laser-induced generation of structural defects in vitreous silica and in activated silicate glass, J. Non-cryst. Solids **70**(1), 45–53 (1985).

[99] A. Chmel and S. B. Eronko, Optical strength of glasses implanted with argon ions, Glass Technol. - Part A **39**(1), 32–34 (1998).

[100] P. N. Saeta and B. I. Greene, Primary relaxation processes at the band edge of SiO_2, Phys. Rev. Lett. **70**(23), 3588 (1993).

[101] P. Audebert, Ph. Daguzan, A. Dos Santos, J. C. Gauthier, J. P. Geindre, S. Guizard, G. Hamoniaux, et al., Space-time observation of an electron gas in SiO_2, Phys. Rev. Lett. **73**(14), 1990 (1994).

[102] D. von der Linde and H. Schüler, Breakdown threshold and plasma form-

ation in femtosecond laser–solid interaction, J. Opt. Soc. Am. B **13**(1), 216–222 (1996).

[103] R. R. Gattass, L. R. Cerami, and E. Mazur, Micromachining of bulk glass with bursts of femtosecond laser pulses at variable repetition rates, Opt. Express **14**(12), 5279–5284 (2006).

[104] T. M. Stephan, B. Van Zyl, and R. C. Amme, Degradation of vacuum-exposed SiO_2 laser windows, Proc. SPIE **1848**, 106–110 (1993).

[105] J. H. Campbell, P. A. Hurst, D. D. Heggins, W. A. Steele, and S. E. Bumpas, Laser-induced damage and fracture in fused silica vacuum windows, Proc. SPIE **2966**, 106–125 (1997).

[106] A. K. Burnham, M. J. Runkel, S. G. Demos, M. R. Kozlowski, and P. J. Wegner, Effect of vacuum on the occurrence of UV-induced surface photoluminescence, transmission loss, and catastrophic surface damage, Proc. SPIE **4134**, 243–252 (2000).

[107] S. G. Demos, A. Burnham, P. J. Wegner, M. Norton, L. Zeller, M. Runkel, M. R. Kozlowski, et al., Surface defect generation in optical materials under high fluence laser irradiation in vacuum, Electron. Lett. **36**(6), 566–567 (2000).

[108] M. A. Norton, L. W. Hrubesh, Z. Wu, E. E. Donohue, M. D. Feit, M. R. Kozlowski, D. Milam, et al., Growth of laser initiated damage in fused silica at 351 nm, Proc. SPIE **4347**, 468 (2001).

[109] P. Allenspacher, W. Riede, D. Wernham, A. Capanni, and F. Era, Vacuum laser damage test bench, Proc. SPIE **5991**, 599128 (2005).

[110] S. Xu, X. Zu, X. Jiang, X. Yuan, J. Huang, H. Wang, H. Lv, and W. Zheng, The damage mechanisms of fused silica irradiated by 355 nm laser in vacuum, Nucl. Instrum. Meth. B **266**(12), 2936–2940 (2008).

[111] D. N. Nguyen, L. A. Emmert, W. Rudolph, D. Patel, E. Krous, C. S. Menoni, and M. Shinn, Studies of femtosecond laser induced damage of HfO_2 thin film in atmospheric and vacuum environments, Proc. SPIE **7504**,

750403 (2009).

[112] X. Ling, Y. Zhao, D. Li, J. Shao, and Z. Fan, Damage investigations of AR coating under atmospheric and vacuum conditions, Opt. Laser Tech. **41**(7), 857–861 (2009).

[113] D. N. Nguyen, L. A. Emmert, P. Schwoebel, D. Patel, C. S. Menoni, M. Shinn, and W. Rudolph, Femtosecond pulse damage thresholds of dielectric coatings in vacuum, Opt. Express **19**(6), 5690–5697 (2011).

[114] S. Schrameyer, H. Mädebach, L. Jensen, D. Ristau, C. Heese, J. Piris, A. Ciapponi, et al., Round-robin experiment on LIDT measurements at 1064 nm in vacuum for space qualification of optics, Proc. SPIE **8885**, 88850F (2013).

[115] X. Zhou, X. Zhou, J. Huang, Q. Cheng, F. Wang, X. Ye, X. Jiang, and W. Wu, Laser-induced point defects in fused silica irradiated by UV laser in vacuum, Adv. Cond. Matter Phys. **2014**, 1–7 (2014).

[116] F. Kong, Y. Jin, H. Huang, H. Zhang, S. Liu, and H. He, Laser-induced damage of multilayer dielectric gratings with picosecond laser pulses under vacuum and air, Opt. Laser Tech. **73**, 39–43 (2015).

[117] F. E. Hovis, B. A. Shepherd, C. T. Radcliffe, and H. A. Maliborski, Contamination damage in pulsed 1–μm lasers, Proc. SPIE **2714**, 707–716 (1996).

[118] H. A. Abdeldayem, E. Dowdye, J. Canham, and T. Jaeger, Contamination and radiation effects on spaceflight laser systems, Proc. SPIE **5897**, 589705 (2005).

[119] A. A. Manenkov, New results on avalanche ionization as a laser damage mechanism in transparent solids, NBS Spec. Publ. (541), 455 (1978).

[120] L. D. Merkle and D. Kitriotis, Temperature dependence of laser-induced bulk damage in SiO_2 and borosilicate glass, Phys. Rev. B **38**(2), 1473 (1988).

[121] K. Mikami, S. Motokoshi, M. Fujita, T. Jitsuno, J. Kawanaka, and R. Yas-

uhara, Laser-induced damage thresholds in silica glasses at different temperature, Proc. SPIE **7504**, 75041R (2009).

[122] K. Mikami, S. Motokoshi, M. Fujita, T. Jitsuno, and M. Murakami, Temperature dependence of nonlinear optical phenomena in silica glasses, Proc. SPIE **7842**, 78420X (2010).

[123] S. Becker, A. Pereira, P. Bouchut, F. Geffraye, and C. Anglade, Laser-induced contamination of silica coatings in vacuum, Proc. SPIE **6403**, 64030J (2006).

[124] H. Schröder, W. Riede, E. Reinhold, D. Wernham, Y. Lien, and H. Kheyrandish, In situ observation of UV-laser-induced deposit formation by fluorescence measurement, Proc. SPIE **6403**, 64031K (2006).

[125] H. Schröder, S. Becker, Y. Lien, W. Riede, and D. Wernham, Fluorescence monitoring of organic deposits, Proc. SPIE **6720**, 67200O (2008).

[126] A. Pereira, E. Quesnel, and M. Reymermier, Dynamic measurements of ultraviolet-enhanced silica contamination by photoluminescence-based diagnostic, J. Appl. Phys. **105**(1), 013109 (2009).

[127] R. Chow, L. V. Berzins, P. A. Arnold, and G. V. Erbert, Reversible laser damage of dichroic coatings in a high-average-power laser vacuum resonator, Proc. SPIE **3902**, 283–291 (2000).

[128] R. R. Kunz, V. Liberman, and D. K. Downs, Experimentation and modeling of organic photocontamination on lithographic optics, Journal of Vacuum Science & Technology B **18**(3), 1306–1313 (2000).

[129] D. Wernham, J. Alves, F. Pettazzi, and A. P. Tighe, Laser-induced contamination mitigation on the ALADIN laser for ADM-Aeolus, Proc. SPIE **7842**, 78421E (2010).

[130] D. C. Brown, The promise of cryogenic solid-state lasers, IEEE J. Sel. Top. Quant. **11**(3), 587–599 (2005).

[131] J. Kawanaka, S. Tokita, H. Nishioka, M. Fujita, K. Yamakawa, K. Ueda, and Y. Izawa, Dramatically improved laser characterist-

ics of diode-pumped yb-doped materials at low temperature, Laser Phys. **15**(9), 1306 (2005).

[132] D. J. Ripin, J. R. Ochoa, R. L. Aggarwal, and T. Y. Fan, 165-W cryogenically cooled Yb: YAG laser, Opt. Lett. **29**(18), 2154–2156 (2004).

[133] W. Heinicke and G. Winterling, The temperature dependence of stimulated Brillouin scattering in quartz, Appl. Phys. Lett. **11**(7), 231–233 (1967).

[134] K. Tanimura, T. Katoh, and N. Itoh, Lattice relaxation of highly excited self-trapped excitons in CaF_2, Phys. Rev. B **40**(2), 1282 (1989).

[135] O. M. Efimov, K. Gabel, S. V. Garnov, L. B. Glebov, S. Grantham, M. Richardson, and M. J. Soileau, Color-center generation in silicate glasses exposed to infrared femtosecond pulses, J. Opt. Soc. Am. B **15**(1), 193–199 (1998).

[136] L. Skuja, H. Hosono, and M. Hirano, Laser-induced color centers in silica, Proc. SPIE **4347**, 155–168 (2001).

[137] L. Courrol, R. Samad, L. Gomez, I. Ranieri, S. Baldochi, A. Zanardi de Freitas, and N. Vieira, Color center production by femtosecond pulse laser irradiation in LiF crystals, Opt. Express **12**(2), 288–293 (2004).

[138] W. Rudolph, L. Emmert, Z. Sun, D. Patel, and C. Menoni, Laser damage in dielectric films: what we know and what we don't, Proc. SPIE **8197**, 888516 (2013).

[139] X. Chen, L. Zhao, X. Fu, L. You, O. Stenzel, H. Kämmer, F. Dreisow, et al., Effect of oxygen vacancies on the laser-induced damage resistance of Y0.26Hf0.74Ox thin films, Opt. Lett. **39**(22), 6470–6473 (2014).

[140] Y. Zhao, W. Gao, J. Shao, and Z. Fan, Roles of absorbing defects and structural defects in multilayer under single-shot and multi-shot laser radiation, Appl. Surf. Sci. **227**(1), 275–281 (2004).

[141] X. Cheng, J. Zhang, T. Ding, Z. Wei, H. Li, and Z. Wang, The effect of an electric field on the thermomechanical damage of nodular defects

in dielectric multilayer coatings irradiated by nanosecond laser pulses, Light Sci. Appl. **2**(6), e80 (2013).

[142] Y. Lee, Evaluating subsurface damage in optical glasses, J. Eur. Opt. Soc.-Rapid **6** (2011).

[143] J. Shen, S. Liu, K. Yi, H. He, J. Shao, and Z. Fan, Subsurface damage in optical substrates, Optik **116**(6), 288–294 (2005).

[144] P. E. Miller, T. I. Suratwala, L. L. Wong, M. D. Feit, J. A. Menapace, P. J. Davis, and R. A. Steele, The distribution of subsurface damage in fused silica, Proc. SPIE **5991**, 599101 (2005).

[145] J. A. Menapace, P. J. Davis, W. A. Steele, L. L. Wong, T. I. Suratwala, and P. E. Miller, MRF applications: measurement of process-dependent subsurface damage in optical materials using the MRF wedge technique, Proc. SPIE **2125**, 599103 (2005).

[146] Z. Wang, Y. Wu, Y. Dai, and S. Li, Subsurface damage distribution in the lapping process, Appl. Optics **47**(10), 1417–1426 (2008).

[147] J. W. Carr, E. Fearon, L. J. Summers, and I. D. Hutcheon, Subsurface damage assessment with atomic force microscopy in *Proceedings of the 1st international conference and general meeting if the European society of precision engineering and nanotechnology*, (1999).

[148] J. Neauport, Ph. Cormont, L. Lamaignère, C. Ambard, F. Pilon, and H. Bercegol, Concerning the impact of polishing induced contamination of fused silica optics on the laser-induced damage density at 351 nm, Opt. Commun. **281**(14), 3802–3805 (2008).

[149] J. Neauport, C. Ambard, P. Cormont, N. Darbois, J. Destribats, C. Luitot, and O. Rondeau, Subsurface damage measurement of ground fused silica parts by HF etching techniques, Opt. Express **17**(22), 20448–20456 (2009).

[150] B. J. Inkson, T. Steer, G. Möbus, and T. Wagner, Subsurface nanoindentation deformation of Cu–Al multilayers mapped in 3D by focused ion beam microscopy, J. Microsc. **201**(2), 256–269 (2001).

[151] M. A. Groeber, B. K. Haley, M. D. Uchic, D. M. Dimiduk, and S. Ghosh, 3D reconstruction and characterization of polycrystalline microstructures using a FIB–SEM system, Mater. Charact. **57**(4), 259–273 (2006).

[152] F. Elfallagh and B. J. Inkson, 3D analysis of crack morphologies in silicate glass using FIB tomography, J. Eur. Ceram. Soc. **29**(1), 47–52 (2009).

[153] C. J. Stolz, M. D. Feit, and T. V. Pistor, Laser intensification by spherical inclusions embedded within multilayer coatings, Appl. Optics **45**(7), 1594–1601 (2006).

[154] W. Kanematsu, M. Sando, L. K. Ives, R. Marinenko, and G. D. Quinn, Dye impregnation method for revealing machining crack geometry, J. Am. Ceram. Soc. **84**(4), 795–800 (2001).

[155] W. Kanematsu, Visualization of subsurface damage in silicon nitride from grinding by a plasma etching and dye impregnation method, J. Am. Ceram. Soc. **89**(8), 2564–2570 (2006).

[156] T. Homma, C. E. D. Chidsey, and M. Watanabe, Method of detecting microscopic defects existing on a silicon wafer (Jan. 16 2001). US Patent 6,174,727.

[157] W. B. Williams, B. A. Mullany, W. C. Parker, P. J. Moyer, and M. H. Randles, Using quantum dots to tag subsurface damage in lapped and polished glass samples, Appl. Optics **48**(27), 5155–5163 (2009).

[158] W. Williams, B. Mullany, W. Parker, P. Moyer, and M. Randles, Using quantum dots to evaluate subsurface damage depths and formation mechanisms in glass, CIRP CIRP Ann.-Manuf. Techn. **59**(1), 569–572 (2010).

[159] P. P. Hed and D. F. Edwards, Relationship between subsurface damage depth and surface roughness during grinding of optical glass with diamond tools, Appl. Optics **26**(13), 2491 (1987).

[160] S. Li, Z. Wang, and Y. Wu, Relationship between subsurface damage and surface roughness of optical materials in grinding and lapping processes,

J. Mater. Process. Tech. **205**(1), 34–41 (2008).

[161] J. Neauport, J. Destribats, C. Maunier, C. Ambard, P. Cormont, B. Pintault, and O. Rondeau, Loose abrasive slurries for optical glass lapping, Appl. Optics **49**(30), 5736–5745 (2010).

[162] Z. Wu, M. D. Feit, M. R. Kozlowski, A. M. Rubenchik, and L. M. Sheehan, Laser modulated scattering as a nondestructive evaluation tool for optical surfaces and thin film coatings, Proc. SPIE **3578**, 721–729 (1999).

[163] W. K. Lu, Z. J. Pei, and J. G. Sun, Non-destructive evaluation methods for subsurface damage in silicon wafers: a literature review, Int. J. Mach. Machinab. Mater. **2**(1), 125–142 (2007).

[164] Z. M. Liao, S. J. Cohen, and J. R. Taylor, Total internal reflection microscopy (TIRM) as a nondestructive subsurface damage assessment tool, Proc. SPIE **2428**, 43–53 (1995).

[165] M. Yan, L. Wang, W. J. Siekhaus, M. R. Kozlowski, T. J. Yang, and U. Mohideen, Defect study in fused silica using near-field scanning optical microscopy, Proc. SPIE **3244**, 268–271 (1998).

[166] L. M. Sheehan, M. R. Kozlowski, and D. W. Camp, Application of total internal reflection microscopy for laser damage studies on fused silica, Proc. SPIE **3244**, 282–295 (1998).

[167] S. G. Demos, M. Staggs, K. Minoshima, and J. Fujimoto, Characterization of laser-induced damage sites in optical components, Opt. Express **10**(25), 1444–1450 (2002).

[168] G. M. Guss, I. L. Bass, R. P. Hackel, C. Mailhiot, and S. G. Demos, In situ monitoring of surface postprocessing in large-aperture fused silica optics with optical coherence tomography, Appl. Optics **47**(25), 4569–4573 (2008).

[169] D. Huang, E. A. Swanson, C. P. Lin, J. S. Schuman, W. G. Stinson, W. Chang, M. R. Hee, et al., Optical coherence tomography, Science **254**(5035), 1178–1181 (1991).

[170] M. Bashkansky, P. R. Battle, M. D. Duncan, M. Kahn, and J. Reintjes, Subsurface defect detection in ceramics using an optical gated scatter reflectometer, J. Am. Ceram. Soc. **79**(5), 1397–1400 (1996).

[171] P. R. Battle, M. Bashkansky, R. Mahon, and J. Reintjes, Subsurface defect detection in ceramic materials using optical gating techniques, Opt. Eng. **35**(4), 1119–1123 (1996).

[172] J. Steinert, S. Gliech, A. Wuttig, A. Duparre, and H. Truckenbrodt, Advanced methods for surface and subsurface defect characterization of optical components, Proc. SPIE **4099**, 290–298 (2000).

[173] A. Wuttig, J. Steinert, A. Duparre, and H. Truckenbrodt, Surface roughness and subsurface damage characterization of fused silica substrates, Proc. SPIE **3739**, 369–376 (1999).

[174] D. Rats, J. von Stebut, and F. Augereau, High frequency scanning acoustic microscopy: a novel non-destructive surface analytical tool for assessment of coating-specific elastic moduli and tomographic study of subsurface defects, Thin Solid Films **355**, 347–352 (1999).

[175] S. S. Mao, F. Quéré, S. Guizard, X. Mao, R. E. Russo, G. Petite, and P. Martin, Dynamics of femtosecond laser interactions with dielectrics, Appl. Phys. A-Mater. **79**(7), 1695–1709 (2004).

[176] H. Yokota, H. Sakata, M. Nishibori, and K. Kinosita, Ellipsometric study of polished glass surfaces, Surf. Sci. **16**, 265–274 (1969).

[177] J. DiJon, T. Poiroux, and C. Desrumaux, Nano absorbing centers: a key point in the laser damage of thin films, Proc. SPIE **2966**, 315–325 (1997).

[178] D. C. Harris, History of magnetorheological finishing, Proc. SPIE **8016**, 80160N (2011).

[179] S. Odenbach and S. Thurm, *Magnetoviscous effects in ferrofluids* (Springer, 2002).

[180] J. A. Menapace, B. Penetrante, D. Golini, A. F. Slomba, P. E. Miller, T. G. Parham, M. Nichols, and J. Peterson, Combined advanced finishing and

UV-laser conditioning for producing UV-damage-resistant fused-silica optics, Proc. SPIE **4679**, 56–68 (2002).

[181] J. A. Menapace, P. R. Ehrmann, and R. C. Bickel, Magnetorheological finishing (MRF) of potassium dihydrogen phosphate (KDP) crystals: nonaqueous fluids development, optical finish, and laser damage performance at 1064 nm and 532 nm, Proc. SPIE **3782**, 750414 (2009).

[182] O. W. Fähnle and H. H. van Brug, Novel approaches to generate aspherical optical surfaces, Proc. SPIE **3782**, 170–180 (1999).

[183] K. Yoshida, T. Hirao, T. Kamimura, K. Ochi, S. Kaku, H. Yoshida, H. Fujita, et al., In-situ optical coatings on subsurface damage-removed substratem, Proc. SPIE **2714**, 340–350 (1996).

[184] D. W. Camp, M. R. Kozlowski, L. M. Sheehan, M. A. Nichols, M. Dovik, R. G. Raether, and I. M. Thomas, Subsurface damage and polishing compound affect the 355 nm laser damage threshold of fused silica surfaces, Proc. SPIE **3244**, 356–364 (1998).

[185] R. M. Brusasco, B. M. Penetrante, J. A. Butler, S. M. Maricle, and J. Peterson, CO_2-laser polishing for reduction of 351 nm surface damage initiation in fused silica, Proc. SPIE **4679**, 34–39 (2002).

[186] J. Neauport, L. Lamaignere, H. Bercegol, F. Pilon, and J. Birolleau, Polishing-induced contamination of fused silica optics and laser induced damage density at 351 nm, Opt. Express **13**(25), 10163–10171 (2005).

[187] S. Papernov and A. W. Schmid, Correlations between embedded single gold nanoparticles in SiO_2 thin film and nanoscale crater formation induced by pulsed-laser radiation, J. Appl. Phys. **92**(10), 5720–5728 (2002).

[188] L. Gallais, J. Capoulade, J. Y. Natoli, and M. Commandré, Investigation of nanodefect properties in optical coatings by coupling measured and simulated laser damage statistics, J. Appl. Phys. **104**(5), 053120 (2008).

[189] J. DiJon, T. Poiroux, and C. Desrumaux, Nano absorbing centers: a key point in the laser damage of thin films, Proc. SPIE **2966**, 315–325 (1997).

[190] K. Bien-Aimé, C. Belin, L. Gallais, P. Grua, E. Fargin, J. Néauport, and I. Tovena-Pecault, Impact of storage induced outgassing organic contamination on laser induced damage of silica optics at 351 nm, Opt. Express **17**(21), 18703–18713 (2009).

[191] R. W. Hopper and D. R. Uhlmann, Mechanism of inclusion damage in laser glass, J. Appl. Phys. **41**(10), 4023–4037 (1970).

[192] M. D. Feit and A. M. Rubenchik, Implications of nanoabsorber initiators for damage probability curves, pulse length scaling, and laser conditioning, Proc. SPIE **5273**, 74–82 (2004).

[193] J. Yu, X. Xiang, S. He, X. Yuan, W. Zheng, H. Lü, and X. Zu, Laser-induced damage initiation and growth of optical materials, Adv. Conden. Matt. Phys. **2014** (2014).

[194] S. Papernov and A. W. Schmid, Using gold nanoparticles as artificial defects in thin films: What have we learned about laser-induced damage driven by localized absorbers?, Proc. SPIE **6403**, 64030D (2006).

[195] B. R. Lawn, *Fracture of brittle solids* (Cambridge University Press, 1993).

[196] T. Suratwala, L. Wong, P. Miller, M. D. Feit, J. Menapace, R. Steele, P. Davis, and D. Walmer, Sub-surface mechanical damage distributions during grinding of fused silica, J. Non-cryst. Solids **352**(52), 5601–5617 (2006).

[197] L. Li, X. Xia, Y. Xiao-Dong, H. Shao-Bo, J. Xiao-Dong, Z. Wan-Guo, and Z. Xiao-Tao, Effect of fused silica subsurface defect site density on light intensification, Chin. Phys. B **22**(5), 054207 (2013).

[198] F. Y. Genin, A. Salleo, T. V. Pistor, and L. L. Chase, Role of light intensification by cracks in optical breakdown on surfaces, JOSA A **18**(10), 2607–2616 (2001).

[199] A. A. Griffeth, The phenomenon of rupture and flow in solids, Philos. Trans. R. Soc. A **221**, 163–168 (1920).

[200] R. J. Tench, M. R. Kozlowski, and R. Chow, Investigation of the micro-

structure of coatings for high power lasers by non-optical techniques, Proc. SPIE **2253**, 596–602 (1994).

[201] K. H. Guenther, Nodular defects in dielectric multilayers and thick single layers, Appl. Optics **20**(6), 1034–1038 (1981).

[202] C. J. Stolz, J. M. Yoshiyarna, A. Salleo, Z. L. Wu, J. Green, and R. Krupka, Characterization of nodular and thermal defects in hafnia/silica multilayer coatings using optical, photothermal, and atomic force microscopy, Proc. SPIE **3244**, 475–483 (1998).

[203] X. Ling, J. Shao, and Z. Fan, Thermal-mechanical modeling of nodular defect embedded within multilayer coatings, J. Vac. Sci. Technol. A **27**(2), 183–186 (2009).

[204] M. J. Brett, R. N. Tait, S. K. Dew, S. Kamasz, A. H. Labun, and T. Smy, Nodular defect growth in thin films, J Mater. Sci.-Mater. El. **3**(1), 64–70 (1992).

[205] L. Dubost, A. Rhallabi, J. Perrin, and J. Schmitt, Growth of nodular defects during film deposition, J. Appl. Phys. **78**(6), 3784–3791 (1995).

[206] R.N. Tait, T. Smy, S.K. Dew, and M.J. Brett, Nodular defect growth and structure in vapor deposited films, J.f Electron. Mater. **24**(8), 935–940 (1995).

[207] Z. Lang and W. Xiuqin, Formation of nodular defects as revealed by simulation of a modified ballistic model of depositional growth, J. Mater. Sci. **33**(6), 1487–1490 (1998).

[208] D. Reicher, P. Black, and K. Jungling, Defect formation in hafnium dioxide thin films, Appl. Optics **39**(10), 1589–1599 (2000).

[209] J. F. DeFord and M. R. Kozlowski, Modeling of electric-field enhancement at nodular defects in dielectric mirror coatings, Proc. SPIE **1848**, 455–472 (1993).

[210] C. J. Stolz, F. Y. Génin, and T. V. Pistor, Electric field enhancement by nodular defects in multilayer coatings irradiated at normal and 45 incidence,

Proc. SPIE **5273**, 41–49 (2004).

[211] J. Bellum, D. Kletecka, P. Rambo, I. Smith, J. Schwarz, and B. Atherton, Comparisons between laser damage and optical electric field behaviors for hafnia/silica antireflection coatings., Appl. Optics **50**(9), C340 (2011).

[212] X. Cheng, Z. Shen, H. Jiao, J. Zhang, B. Ma, T. Ding, J. Lu, et al., Laser damage study of nodules in electron-beam-evaporated HfO_2/SiO_2 high reflectors, Appl. Optics **50**(9), C357–C363 (2011).

[213] L. Smalakys, G. Batavičiūtė, E. Pupka, and A. Melninkaitis, Comprehensive studies of IR to UV light intensification by nodular defects in HfO_2/SiO_2 multilayer mirrors, Proc. SPIE **9237**, 92371I (2014).

[214] Y. Shan, H. He, C. Wei, S. Li, M.Zhou, D. Li, and Y. Zhao, LIGO: The laser interferometer gravitational-wave observatory, Appl. Opt. **49**(22), 4290–4295 (2010).

[215] O. Stenzel, S. Wilbrandt, S. Yulin, N. Kaiser, M. Held, A. Tünnermann, J. Biskupek, and U. Kaiser, Plasma ion assisted deposition of hafnium dioxide using argon and xenon as process gases, Opt. Mater. Express **1**(2), 278–292 (2011).

[216] J. W. Arenberg, Revised damage frequency method for the determination of laser damage threshold, Proc. SPIE **2114**, 521 (1993).

[217] J. W. Arenberg, Direct comparison of the damage frequency method and binary search technique, Proc. SPIE **2254**, 599125 (2005).

[218] Evaluation of measurement data – guide to the expression of uncertainty in measurement, JCGM 100:2008 (2008).

[219] International vocabulary of basic and general terms in metrology, BIPM **2**, 59 (1993).

[220] J. M. Liu, Simple technique for measurements of pulsed Gaussian-beam spot sizes, Opt. Lett. **7**(5), 196–198 (1982).

[221] M. Mero, B. Clapp, J. C. Jasapara, W. Rudolph, D. Ristau, K. Starke, J. Krüger, et al., On the damage behavior of dielectric films when illu-

minated with multiple femtosecond laser pulses, Opt. Eng. **44**(5), 051107 (2005).

[222] M. Lenzner, F. Krausz, J. Kruger, and W. Kautek, Photoablation with sub-10 fs laser pulses, Appl. Surf. Sci. **154-155**(0), 11–16 (2000).

[223] 11254-2: Determination of laser-induced damage threshold of optical surfaces – Part 2: S-on-1 test, ISO (2011).

[224] Laser-induced damage threshold and certification procedures for optical materials, (NASA Reference Publication) **1395** (1997).

[225] J. W. Arenberg, Accuracy and precision of laser damage measurements made via binary search techniques, Proc. SPIE **2714**, 80 (1995).

[226] J. Hue, P. Garrec, J. DiJon, and P. Lyan, R-on-1 automatic mapping: a new tool for laser damage testing, Proc. SPIE **2714**, 90–101 (1996).

[227] L. Lamaignère, M. Balas, R. Courchinoux, T. Donval, J. C. Poncetta, S. Reyné, B. Bertussi, and H. Bercegol, Parametric study of laser-induced surface damage density measurements: toward reproducibility, J. Appl. Phys. **107**(2), 023105 (2010).

[228] M. D. Feit, A. M. Rubenchik, M. R. Kozlowski, F. Y. Genin, S. Schwartz, and L. M. Sheehan, Extrapolation of damage test data to predict performance of large-area NIF optics at 355 nm, Proc. SPIE **3578**, 226–234 (1999).

[229] L. Lamaignère, T. Donval, M. Loiseau, J. C. Poncetta, G. Razé, C. Meslin, B. Bertussi, and H. Bercegol, Accurate measurements of laser-induced bulk damage density, Meas. Sci. Technol. **20**(9), 095701 (2009).

[230] L. Gallais, J. Capoulade, J. Y. Natoli, and M. Commandré, Investigation of nanodefect properties in optical coatings by coupling measured and simulated laser damage statistics, J. Appl. Phys. **104**(5), 053120 (2008).

[231] S. K. Katti and A. V. Rao, Handbook of the poisson distribution, Technometrics **10**(2), 412 (1968).

[232] G. Batavičiūtė, P. Grigas, L. Smalakys, and A. Melninkaitis, Revision of laser-induced damage threshold evaluation from damage probability

data, Rev. Sci. Instru. **84**, 045108 (2013).

[233] C. L. Lawson and R. J. Hanson, *Solving least squares problems* (SIAM, 1974).

[234] K. Starke, H. Blaschke, M. Jupé, M. Lappschies, and D. Ristau, Modern topics in standardized laser-induced damage threshold measurements in *Optical Systems Design 2005*, 59650D, International Society for Optics and Photonics (2005).

[235] J. Y. Natoli, L. Gallais, H. Akhouayri, and C. Amra, Laser-induced damage of materials in bulk, thin-film, and liquid forms, Appl. Optics **41**(16), 3156–3166 (2002).

[236] J. W. Arenberg, Calculation of uncertainty in laser-damage thresholds determined by use of the damage-frequency method, Proc. SPIE **2428**, 489–502 (1995).

[237] A. Hildenbrand, F. R. Wagner, H. Akhouayri, J. Y. Natoli, and M. Commandré, Accurate metrology for laser damage measurements in nonlinear crystals, Opt. Eng. **47**(8), 083603 (2008).

[238] J. W. Arenberg, Comparison of the damage frequency method and the binary search technique, Proc. SPIE **5991**, 599125 (2005).

[239] I. J. Myung, Tutorial on maximum likelihood estimation, J. Math. Psychol. **47**, 90–100 (2003).

[240] T. I. Suratwala, P. Miller, J. D. Bude, W. A. Steele, N. Shen, M. V. Monticelli, M. D. Feit, et al., HF-based etching processes for improving laser damage resistance of fused silica optical surfaces, J. Am. Ceram. Soc. **94**(2), 416–428 (2011).

[241] C. A. Schneider, W. S. Rasband, and K. W. Eliceiri, NIH Image to ImageJ: 25 years of image analysis, Nature Methods **9**(7), 671–675 (2012).

[242] J. H. Campbell, R. A. Hawley-Fedder, C. J Stolz, J. A. Menapace, M. R. Borden, P. K. Whitman, J. Yu, et al., NIF optical materials and fabrication technologies: an overview, Proc. SPIE **5341**, 84–101 (2004).

[243] S. Schwartz, M. D. Feit, M. R. Kozlowski, and R. P. Mouser, Current 3-ω

large optic test procedures and data analysis for the quality assurance of National Ignition Facility optics, Proc. SPIE **3578**, 314–321 (1999).

[244] C. W. Carr, M. D. Feit, M. C. Nostrand, and J. J. Adams, Techniques for qualitative and quantitative measurement of aspects of laser-induced damage important for laser beam propagation, Meas. Sci. Technol. **17**(7), 1958 (2006).

[245] J. Bude, P. Miller, S. Baxamusa, N. Shen, T. Laurence, W. Steele, T. Suratwala, et al., High fluence laser damage precursors and their mitigation in fused silica, Opt. Express **22**(5), 5839–5851 (2014).

[246] `http://www.optimal-technologies.com`, Hard coating and cleaning system solutions from Optimal technologies (May 2015).

[247] D. Milam, R. A. Bradbury, and M. Bass, Laser damage threshold for dielectric coatings as determined by inclusions, Appl. Phys. Lett. **23**(12), 654–657 (1973).

[248] B. E. Newnam, D. H. Gill, and G. Faulkner, Influence of standing-wave fields on the laser damage resistance of dielectric films, Proc. SPIE **28**(604), 254–271 (1976).

[249] A. J. Yuffa and J. A. Scales, Object-oriented electrodynamic S-matrix code with modern applications, J. Comput. Phys. **231**(14), 4823–4835 (2012).

[250] S. Kičas, G. Batavičiūtė, K. Juškevicius, T. Tolenis, R. Drazdys, R. Buzelis, and A. Melninkaitis, Characterization and application of $HfO_2 - SiO_2$ mixtures produced by ion-beam sputtering technology, Proc. SPIE **8885**, 888521–1–7 (2013).

[251] T. Amotchkina, M. Trubetskov, A. Tikhonravov, I. B. Angelov, and V. Pervak, Reliable optical characterization of e-beam evaporated TiO_2 films deposited at different substrate temperatures, Appl. Optics **53**(4), A8–A15 (2014).

[252] J. R. Bettis, A. H. Guenther, and R. A. House II, Refractive-index dependence of pulsed-laser-induced damage, Opt. Lett. **4**(8), 256–258 (1979).

[253] J. R. Bettis, Correlation among the laser-induced breakdown thresholds in solids, liquids, and gases, Appl. Optics **31**(18), 3448–3452 (1992).

[254] B. Mangote, L. Gallais, M. Commandré, M. Mende, L. Jensen, H. Ehlers, M. Jupé, et al., Femtosecond laser damage resistance of oxide and mixture oxide optical coatings, Opt. Lett. **37**(9), 1478–1480 (2012).

[255] F. Y. Genin, C. J. Stolz, T. A. Reitter, M. R. Kozlowski, R. P. Bevis, and M. K. Von Gunten, Effect of electric field distribution on the morphologies of laser-induced damage in hafnia-silica multilayer polarizers, Proc. SPIE **2966**, 342–352 (1997).